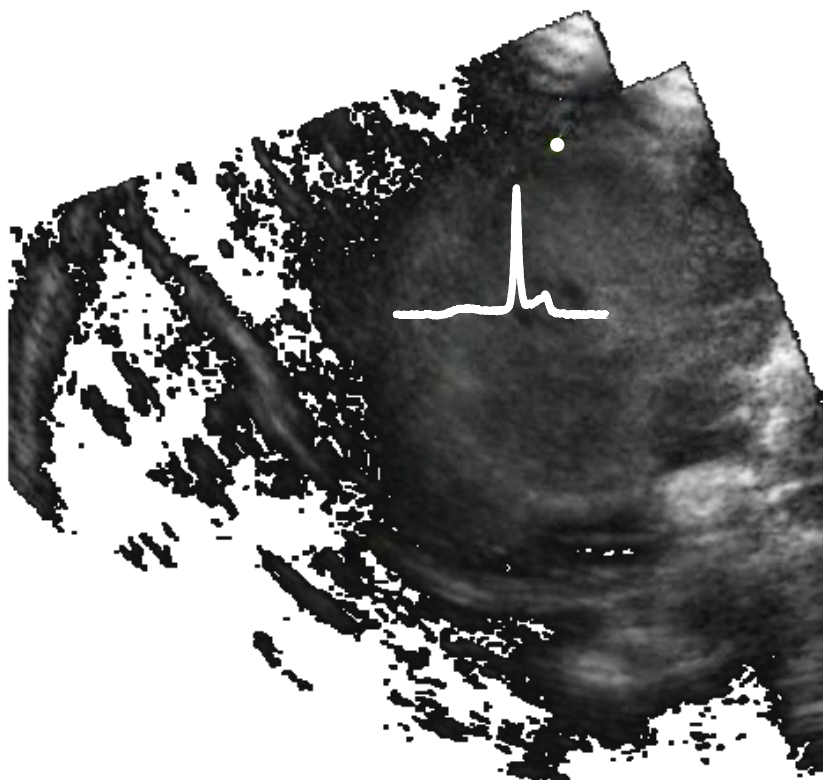


Fluorescence Spectroscopy for Quantitative Demarcation of Glioblastoma Using 5-Aminolevulinic Acid

Neda Haj-Hosseini



Linköping University

FLUORESCENCE SPECTROSCOPY FOR QUANTITATIVE DEMARCATION OF GLIOBLASTOMA
USING 5-AMINOLEVULINIC ACID

Neda Haj-Hosseini

Supervisor: Karin Wårdell, Prof.

Co-supervisor: Göran Salerud, Prof

Linköping Studies in Science and Technology. Dissertations, No. 1463

Copyright © Neda Haj-Hosseini 2012, unless otherwise noted
All rights reserved.

Department of Biomedical Engineering
Linköping University
SE-581 85 Linköping, Sweden

ISBN: 978-91-7519-845-3

ISSN: 0345-7524

Printed in Linköping, Sweden, by LiU-Tryck Linköping, 2012

Abstract

Total resection of glioblastoma, the highly malignant brain tumor, is difficult to accomplish due to its diffuse growth and similarity to the surrounding brain tissue. A total resection is proven to increase patient survival. The aim of this thesis was to evaluate fiber-optical based fluorescence spectroscopy for quantitative demarcation of malignant brain tumors during the surgery. Five-aminolevulinic acid (5-ALA) was used as a fluorescence contrast agent that accumulated as protoporphyrin IX (PpIX) in the tumor.

The method was evaluated at the Department of Neurosurgery, Linköping University Hospital. The patients ($n = 22$) received an oral dose of 5 mg/kg body weight 5-ALA two hours prior to craniotomy. Measurements with a developed fluorescence spectroscopy system were performed under the general procedure of surgery. The collected fluorescence spectra were quantified by defining a fluorescence ratio and the main challenges of measuring and quantifying spectra were investigated. The fluorescence ratio was compared to visual diagnosis of the surgeon, histopathological examination and ultrasound-based neuronavigation. The main challenges of using a fluorescence spectroscopy system in the operating room were the disturbing ambient light, photobleaching and blood interference which affect the signal quantification. The superimposition of ambient light was removed by modulating the system.

Using principal component analysis (PCA) the photobleaching sequences could be described by three spectral components of autofluorescence, PpIX fluorescence and blue-shift. To investigate the photobleaching induced prior to the measurements, a dynamic model was developed based on the PCA derived spectral components. Modulation and increased power of the excitation light resulted in a faster photobleaching; however, photobleaching was saturated at higher excitation powers. The system was adjusted to induce minimal photobleaching. In addition, effect of blood absorption on the fluorescence spectrum was investigated experimentally by placing blood drops on skin and theoretically by using Beer-Lambert law. The theoretical model was used to compensate for the distorted fluorescence ratio. According to the theoretical model of blood interference, a total 300 μm blood layer blocked the brain fluorescence signal totally and when the fluorescence signal was partially blocked, the fluorescence ratio was overestimated. The fluorescence ratio was corrected for blood layers thinner than 50 μm .

The tissue in and around the tumor was categorized into necrosis, low and high grade tumor and gliosis. The median fluorescence ratio confirmed with histopathological examination ($n = 45$) had a lower fluorescence ratio for low grade malignancies (0.3) than high grade malignancies (2.4) ($p < 0.05$). Gliosis (1.6) and necrosis (1.0) showed a moderate fluorescence ratio. Ultrasound-based navigation in combination with fluorescence spectroscopy showed improvement in the results; however, a more extensive study is needed to confirm benefits of the method combination. In conclusion, fluorescence spectroscopy of 5-ALA induced PpIX provided an objective method for differentiating tumor from the healthy tissue intra-operatively. Fluorescence ratios were indicative of tissue type and tumor malignancy degree.

Sammanfattning

Total resektion av glioblastoma, höggradig malign hjärntumör, är svår att utföra på grund av dess diffusa tillväxt och likhet med den omgivande hjärnvävnaden. En total resektion har visat sig öka patientens överlevnad. Syftet med denna avhandling är att utvärdera en fiberoptisk fluorescensspektroskopimetod för kvantitativ avgränsning av maligna hjärntumörer under operationen. Fem-aminolevulinsyra (5-ALA) användes som fluorescenskontrast, vilket ackumuleras som protoporfyrin IX (PpIX) i tumören.

Metoden utvärderades vid Neurokirurgiska kliniken, Universitetssjukhuset i Linköping. Patienterna (n = 22) erhöll en oral dos av 5 mg/kg kroppsvikt 5-ALA två timmar före kraniotomi. Mätningar med det egenutvecklade fluorescensspektroskopisystemet utfördes enligt det allmänna kirurgiska förfarandet. Insamlade fluorescensspektra kvantifierades genom att definiera en fluorescenskvot och de viktigaste utmaningarna för att mäta och kvantifiera spektra undersöktes. Fluorescenskvoten jämfördes med visuell diagnos av kirurgen, histopatologisk undersökning och ultraljudsbaserad neuronavigation. De största utmaningarna med att använda ett fluorescensspektroskopisystem i operationssalen var störning av omgivande ljus, fotoblekning och blod som påverkar signalens kvantifiering. Överlagringen av omgivande ljus avlägsnades genom modulering av systemet.

Genom användning av principal komponent analys (PCA) kunde fotoblekningssekvenser beskrivas genom tre spektrala komponenter; autofluorescens, PpIX fluorescens och blå-skift. För att undersöka fotoblekningen inducerad före mätningarna, gjordes en dynamisk modell baserad på de härledda spektrala komponenterna. Modulation och ökad effekt av excitationsljuset resulterade i en snabbare fotoblekning, men fotoblekningen var mättad vid högre excitationseffekt. Systemet justerades för att framkalla minimal fotoblekning. Dessutom har effekten av blodabsorption på fluorescerande spekrat undersökts experimentellt genom att placera bloddroppar på huden och teoretiskt genom att använda Beer-Lamberts lag. Den teoretiska modellen användes för att kompensera för den påverkade fluorescenskvoten. Enligt teoretiska modellen av blodstörningar blockeras fluorescenssignaler uppmätta på hjärnvävnad av ett 300 µm tjockt blodskikt och när fluorescenssignalen delvis blockerades var fluorescenskvoten överskattad. Fluorescenskvoten korrigerar för blodlagrer tunnare än 50 µm.

Vävnaden i och runt tumören kategoriserades som nekros, låg och hög gradig tumör och glios. Medianvärdet av fluorescenskvoten vilken bekräftades av histopatologisk undersökning (n = 45) hade en lägre fluorescenskvot vid låggradiga maligniteter (0,3) än höggradiga maligniteter (2,4) ($p < 0,05$). Glios (1,6) och nekrotiska zonen (1,0) visade en måttlig fluorescenskvot. Ultraljudsnavigering i kombination med fluorescensspektroskopi visade förbättring av resultaten, men en mer omfattande studie behövs för att bekräfta diagnostiska fördelarna med metodkombinationen. Sammanfattningsvis tillhandahåller fluorescensspektroskopi med 5-ALA-inducerad PpIX en objektiv metod för att differentiera tumör från den friska vävnaden intraoperativt. Fluorescenskvoterna indikerar vävnads typ och malignitetsgrad.

**“NOTHING IN LIFE IS TO BE
FEARED, IT IS ONLY TO BE
UNDERSTOOD.”**

- MARIE CURIE

(1867-1934)

List of Publications:

Main thesis publications:

- I. N. Haj-Hosseini, J. Richter, S. Andersson-Engels, and K. Wårdell, "Optical touch pointer for fluorescence guided glioblastoma resection using 5-aminolevulinic acid" *Lasers in Surgery and Medicine*, vol. 42, pp. 9-14, 2010.
- II. J. Richter, N. Haj-Hosseini, S. Andersson-Engels, and K. Wårdell, "Fluorescence spectroscopy measurements for resection of malignant brain tumors", *Lasers in Surgery and Medicine*, vol 43, pp 8-14, 2011.
- III. N. Haj-Hosseini, J. Richter, S. Andersson-Engels, and K. Wårdell, "Photobleaching behavior of protoporphyrin IX during 5-aminolevulinic acid marked glioblastoma detection", *Proceedings of SPIE*, vol. 7161, pp. 716131-8, 2009.
- IV. M. Brydegaard, N. Haj-Hosseini, K. Wårdell and S. Andersson-Engels, "Photo-bleaching Insensitive Fluorescence Diagnostics in Skin and Brain Tissue", *IEEE Journal of Photonics*, Vol 3, No. 3, pp 407-421, 2011.
- V. N. Haj-Hosseini, G. Salerud and K. Wårdell, "Compensation for blood interference in the tissue fluorescence - application in fluorescence guided brain tumor resection ", *Journal article*, submitted, 2012.

Related publications:

1. N. Haj-Hosseini, S. Lowndes, G. Salerud and K. Wårdell, "Blood Interference in fiber-optical based fluorescence guided resection of glioma using 5-aminolevulinic acid", *Proceedings of SPIE*, 78833R-1-10, 2011.
2. N. Haj-Hosseini, S. Andersson-Engels, and K. Wårdell, "Evaluation of a Fiber-Optic Based Pulsed Laser System for Fluorescence Spectroscopy", *Proceedings of 14th Nordic-Baltic Conference on Biomedical Engineering and Medical Physics*, 2008, pp. 363-366.
3. J. D. Johansson, P. Blomstedt, N. Haj-Hosseini, A. T. Bergenheim, O. Eriksson, and K. Wårdell, "Combined Diffuse Light Reflectance and Electrical Impedance Measurements as a Navigation Aid in Deep Brain Surgery", *Stereotactic and Functional Neurosurgery*, 87 (2), pp 105-113, 2009.

Acronyms

ALA	Aminolevulinic acid
ALAD	ALA dehydrase
ALAS	ALA synthase enzyme
BBB	Blood brain barrier
CNS	Central nervous system
CSF	Cerebrospinal fluid
CT	Computed tomography
CW	Continuous wave
DR	Double ratio
DRS	Diffuse reflection spectroscopy
FC	Ferrochelatase
FGR	Fluorescence-guided resection
FN	False negative
FP	False positive
GBM	Glioblastoma
GTR	Gross total resection
HG	High grade tumor
HIS	Hyperspectral imaging
HPD	Hematoporphyrin derivative
LED	Light emitting diode
LGT	Low grade tumor
MER	Micro electrode recording
mfp	Mean free path
MRI	Magnetic resonance imaging
MRSI	Magnetic resonance spectroscopic imaging
MSI	Multispectral imaging
mTHPC	Meta-tetra hydroxyphenyl chlorin
NADH	Nicotinamide adenine dinucleotide
NFR	Normalized fluorescence ratio
OCT	Optical coherence tomography
OR	Operating room
OTP	Optical touch pointer
PAI	Photoacoustic imaging
PAS	Photoacoustic spectroscopy
PBG	Porphobilinogen
PBGD	Porphobilinogen deaminase
PCA	Principal component analysis
PDT	Photodynamic therapy
PET	Positron emission tomography
PL	Pulsed
PpIX	Protoporphyrin IX
PPV	Positive predictive value
Sn	Sensitivity
Sp	Specificity
SVD	Singular value decomposition
TN	True negative
TP	True positive
US	Ultrasound
WHO	World Health Organization

Table of Contents

CHAPTER 1

INTRODUCTION	1
---------------------------	----------

CHAPTER 2

THE HUMAN BRAIN AND BRAIN TUMORS.....	3
2.1 THE BRAIN	3
2.1.1 <i>Cells of the Brain</i>	4
2.1.2 <i>Blood Brain Barrier</i>	5
2.2 BRAIN TUMORS	5
2.2.1 <i>Meningioma and Metastases</i>	6
2.2.2 <i>Glioma</i>	6
2.3 GLIOBLASTOMA.....	6
2.3.1 <i>Pathology</i>	7
2.3.2 <i>Diagnosis and Treatment</i>	8
2.3.3 <i>Prognosis</i>	8
2.3.4 <i>Guidance during Brain Tumor Resection</i>	9

CHAPTER 3

OPTICAL METHODS	11
3.1 LIGHT INTERACTION WITH TISSUE.....	11
3.1.1 <i>Absorption</i>	12
3.1.2 <i>Scattering</i>	12
3.1.3 <i>Phase Function and Anisotropy Factor</i>	13
3.1.4 <i>Reduced Scattering</i>	14
3.1.5 <i>Total Attenuation and Penetration Depth</i>	15
3.1.6 <i>Optical Properties of Brain Tissue and Blood</i>	15
3.2 FLUORESCENCE	16
3.3 EXCITATION AND DETECTION OF FLUORESCENCE	17
3.3.1 <i>Light Detectors</i>	18
3.3.2 <i>Optical Fibers</i>	18

CHAPTER 4

FLUORESCENCE-GUIDED RESECTION OF BRAIN TUMOR	19
4.1 TISSUE FLUORESCENCE	19
4.1.1 <i>Brain Tissue Fluorescence</i>	20
4.2 PHOTOSENSITIZERS.....	20
4.3 SPECIFICATIONS OF ALA	22
4.4 CLINICAL STUDIES BASED ON ALA GUIDED BRAIN TUMOR RESECTION	23
4.4.1 <i>Fluorescence Microscopy</i>	24
4.4.2 <i>Fiber-Optical Based Fluorescence Spectroscopy</i>	26
4.5 FLUORESCENCE INTENSITY AND QUANTIFICATION METHODS	26
4.5.1 <i>Fluorophore Concentration and Quantum Yield</i>	27
4.5.2 <i>Quantification Methods</i>	27

CHAPTER 5	
AIM OF THE THESIS	29
CHAPTER 6	
THE FLUORESCENCE SPECTROSCOPY SYSTEM	31
6.1 SYSTEM SPECIFICATIONS	31
6.1.1 <i>Suppression of Ambient Light</i>	32
6.1.2 <i>Optical Probes</i>	33
6.2 OPTICAL SPECIFICATIONS	34
6.2.1 <i>Laser Safety</i>	34
6.2.2 <i>Optical Parameters for Excitation</i>	35
6.2.3 <i>Excitation Depth</i>	38
6.3 COMBINATION WITH ULTRASOUND-BASED NEURONAVIGATION	39
CHAPTER 7	
SIGNAL QUANTIFICATION	41
7.1 MEASUREMENTS ON THE SKIN.....	41
7.2 FILTERING AND CALIBRATION	42
7.3 FLUORESCENCE RATIO	43
7.4 BLOOD INTERFERENCE	44
CHAPTER 8	
PHOTBLEACHING DYNAMICS	49
8.1 DYNAMIC MODEL OF PHOTBLEACHING	49
8.2 PARAMETERS INFLUENCING PHOTBLEACHING	50
8.2.1 <i>Effect of Photobleaching on Autofluorescence and Blue-Shift</i>	51
8.2.2 <i>Effect of Excitation Power and Modulation on Photobleaching</i>	51
CHAPTER 9	
CLINICAL EVALUATION	53
9.1 CLINICAL PROCEDURE AND DATA COLLECTION	53
9.2 STATISTICAL ANALYSIS AND CLINICAL PERFORMANCE MEASURES	54
9.2.1 <i>Quantified Approach</i>	55
9.2.2 <i>Binominal Approach</i>	57
CHAPTER 10	
REVIEW OF THE PAPERS	59
CHAPTER 11	
DISCUSSION AND CONCLUSIONS	63
ACKNOWLEDGEMENTS	67
REFERENCES	69

Chapter 1

Introduction

The highly malignant brain tumor, glioblastoma (GBM), is the most common aggressive brain tumor in adults and is often removed by surgery. The infiltrative growth and similarity of GBM to the surrounding brain tissue makes surgical resection a difficult task [1]. An incomplete resection leads to a faster recurrence of the tumor and thus a poor prognosis for the patient. Resection of a high percentage of tumor volume is reported to be associated with approximately five months higher survival advantage than the one year median survival length [2, 3]. Different intraoperative guidance methods including intraoperative MRI, CT and neuronavigation may be used to assist the tumor visualization [4].

At present, extensive studies are being conducted on the application of fluorescence-guided resection of brain tumors. Fluorescence is induced in the tumor by oral administration of 5-aminolevulinic acid (5-ALA) in doses of 20 mg/kg body weight prior to surgery. Fluorescence in the tumor is visualized through a modified surgical microscope and diagnosis is based on visual inspection of the fluorescence as vague or solid. In an extensive study Stummer et al. showed the usefulness of ALA guided resection in achieving higher degrees of resection and survival advantage for patients [3, 5]. The method has recently been approved for clinical use in Europe [6] and is under investigation for approval in several other countries including the USA, Australia and several Asian countries.

In this thesis a fiber-optical based fluorescence spectroscopy system for quantitative demarcation of highly malignant brain tumors was developed and evaluated. Fluorescence spectroscopy has advantages over fluorescence microscopy in the detection of weak signals and examination of the tumor extents in depth. The essence of fluorescence spectroscopy makes objective detection of fluorescence and quantification of the signals possible. In addition, a lower dose of ALA may be used together with a fluorescence spectroscopy system. The work presented in this thesis was carried out in collaboration with the Department of Neurosurgery at Linköping University Hospital and Department of Physics at Lund University.

The main challenges of using the fluorescence spectroscopy system in the operating room were the disturbing ambient light, photobleaching and blood interference that affect the signal quantification. The effect of ambient light was removed by modulating the system. Photobleaching induced by the system was measured and set to minimum. To estimate the photobleaching caused by the surgical microscope prior to the measurements, and to further investigate the parameters affecting the photobleaching, a model was developed based on principal component analysis. Blood strongly affected the signature of the fluorescence and thus the signal quantification. The effect of blood on the fluorescence signals was investigated experimentally and theoretically. Based on the theoretical model, the distortion induced by blood was corrected in the fluorescence signals.

The work presented in this thesis addresses intraoperative fluorescence spectroscopy and the challenges toward a quantified approach of fluorescence-guided resection of glioblastoma. The medical background concerning brain tumors, diagnosis and treatment is discussed in Chapter 2. The related optical principles and fluorescence mechanisms of tissue and photosensitizers are discussed in Chapters 3 and 4. Chapter 4 further reviews the current status of studies that consider ALA-guided resection using microscopy and spectroscopy methods. Chapters 6-9 describe the work performed on the system development, signal analysis and clinical evaluation of the technique. Chapter 6 gives a description of the technical aspects of the system including light source, signal collection routine and evaluation of parameters affecting measurements. Application of ultrasound-based neuronavigation as a complementary method for the fluorescence spectroscopy system is included in this chapter. Chapter 7 describes methods of signal quantification, filtering and calibration used for analysis of data included in Chapter 9. Experimental and theoretical modeling of blood interference and the proposed correction method is discussed as part of signal quantification in Chapter 7; however, the correction is applied to one patient data set separately and not to the data in Chapter 9. Photobleaching is discussed separately in Chapter 8 due to its importance and characteristic behavior; however, it is a parameter that affects signal quantification and is considered in the system setting. An overview of clinical measurements and clinical evaluation of quantified fluorescence-guided resection based on statistical methods is included in Chapter 9. The usefulness of combining the method with complementary methods is briefly investigated in this chapter.

Chapter 2

The Human Brain and Brain Tumors

2.1 The Brain

The nervous system conducts the electrical signals between different body parts and is divided into central and peripheral areas. The part of the nervous system localized in the brain and spinal cord functions as the control unit and is known as the central nervous system (CNS). Peripheral nervous system (PNS) is the nervous tissue outside of the CNS. The brain, sheltered by a skull (cranial bones), weighs approximately 1.5 kg in a human adult and is protected by three meninges of dura mater, arachnoid and pia mater in addition to the cerebrospinal fluid (CSF). Dura mater is a thick skin-like layer below the bone. Pia mater is very thin and attached to the brain cortex. Arachnoid has a web-like structure and lies in between these two membranes [7].

The brain is divided into four major parts of cerebrum, cerebellum, brainstem and diencephalon. *The cerebrum* composes the bigger part of the brain and is responsible for intelligent abilities. The upper 2-4 mm of the cerebrum is a layer of gray matter called the cerebral cortex. The deeper part of the cerebrum is composed of white matter. The *diencephalon* lies inferior to the cerebrum and includes thalamus, hypothalamus, epithalamus and subthalamus. The *cerebellum* is located in the inferior – posterior part of the brain. The *brain stem* lies between the diencephalon and spinal cord [8].

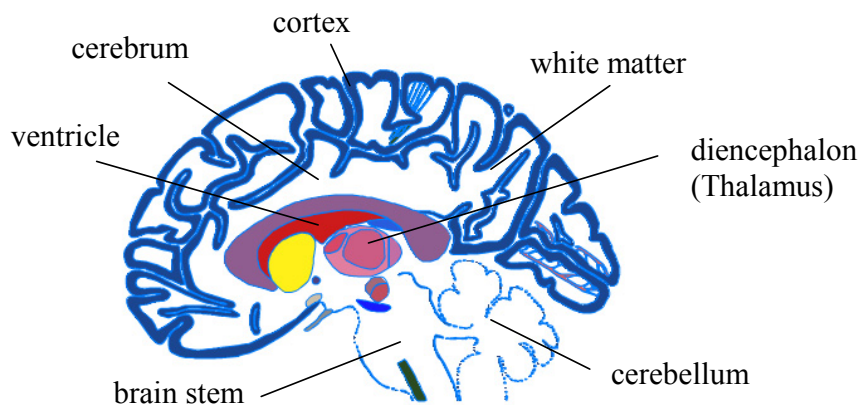


Figure 1 Principal parts of the brain (Image extracted from Cerefy Clinical Brain Atlas).

The gray matter of the brain composes the cerebral cortex and the deep brain structures (basal ganglia and mid brain). Neuron cell bodies, dendrites, unmyelinated axons and axon terminals form the gray matter. The blood supply to the gray matter is high due to its

high metabolism. Cerebral white matter consists of both myelinated and unmyelinated axons in form of tracts and is located below the cortex. The existence of myelinated axons gives the white matter its whitish color [8, 9].

2.1.1 Cells of the Brain

The nervous system is mainly composed of *neural* and *glial cells*. The whole brain of human adult is composed of approximately 170 billion cells in total 86 billion of which are neural and 84 are glial cells. The ratio of glial to neural cells varies in different parts of the brain but is close to one for the whole brain. The cerebral cortex contains 16 billion neurons and 61 billion glial cells (glial/neural = 3.8) and the cerebellum contains 69 billion neurons and 16 billion glial cells (glial/neural = 0.2). The glial/neural cell proportion is 1.5 in gray matter and 15.4 in the white matter [10].

The principal cell type responsible for the electrical function and signal transmission in the CNS and peripheral nervous system is the neural cell, also called neuron. Neurons' sizes and shapes vary depending on their function. Each neuron is composed of dendrites, a cell body, axon and axon terminals. The cell body of the neuron includes nucleus, cytoplasm and organelles. Neurons have the same organelles as the other cells; i.e., mitochondria, ribosome, golgi apparatus and cytoskeleton. However, the number of some organelles depends on the activity of the cell and is higher in neurons. Axons of some neurons are covered by a sheath of lipid and protein, called myelin. Myelin is formed by glial cells and speeds propagation of electrical signals in the axon [7, 11].

Neurons in general are classified into sensory, motor and interneural (association) types based on their function. Sensory neurons (available in PNS) transfer the information from the sensory receptors in different parts of the body to the CNS. The motor neurons (available in PNS) deliver the instructions from the CNS to the peripheral tissue. The interneurons are responsible for coordination of motor function with the sensory information and are mostly found in the CNS [7].

Additional to the neurons, glial cells, also called neuroglial cells, play an important role in the function of the nervous system. *Glia* originates from the Greek word for glue and was first thought to only mechanically support the neurons. Findings show the involvement of glial cells in transmitting information and pathogenesis [11]. Glial cells are of multiple kinds; in the central nervous system (CNS) they include oligodendrocytes, astrocytes, microglial and ependymal cells [8].

Astrocytes are star shaped and have many processes. They help with the maintenance of the chemical medium around the neurons, form and maintain the blood brain barrier (BBB), guide neuron development and repair neural tissue. *Oligodendrocytes* are smaller than astrocytes and have fewer processes. They help with the production of the myelin sheet around the axons and clustering of axons together. *Microglias* are small cells with few processes and protect the brain from the debris of dead cells, wastes and microbes. *Ependymal cells* have a cubic form and are arranged in a line. They participate in forming the cerebrospinal fluid in the ventricles [7, 8].

2.1.2 Blood Brain Barrier

The cerebral endothelium (thin layer of cells in the interior surface of vessels), differs from other tissue type vessels in having tight junctions between its cells which in turn forms a barrier for specific substances to enter the brain. The blood brain barrier keeps the homeostasis of the cerebral micro-environment and controls the exchange of substances between blood, brain and the cerebrospinal fluid. BBB is permeable to lipid solubles (e.g. oxygen and alcohol) and a few water soluble substances (e.g. glucose). Creatine, urea and ions pass very slowly and proteins and antibiotic drugs do not pass the BBB [8, 12]. The permeability of the BBB is altered by factors affecting the endothelial cell surface properties, cytoskeleton and BBB junctions. Inflammation (edema) is a case in which the BBB breaks down due to the secreted agents related to the immune system [12].

2.2 Brain Tumors

Cancer is defined as the growth of abnormal cells in the tissue or the uncontrolled growth and spread of cells [13, 14]. A cluster of these abnormal cells is called a tumor. The extent of tumor spreading (tumor staging) and degree of tumor malignancy (tumor grading) are two parameters for evaluating the progress of the cancer [15]. The grading is based on the cytology and histology of the tumors.

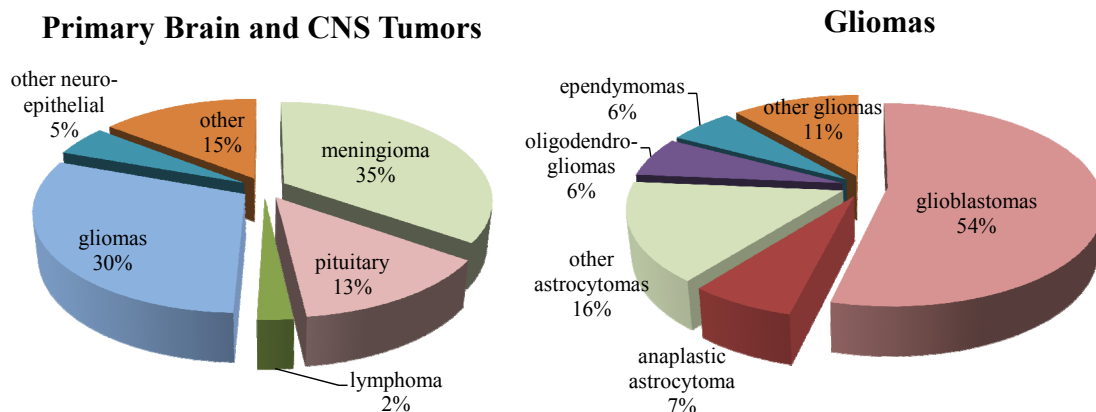


Figure 2 Primary brain and CNS tumor statistics based on the data from the Central Brain Tumor Registry of the United States for 2004-2008 [16].

Central nervous system tumors composed 1.8 % of all the diagnosed cancers in the European Union (27 States) in 2008 and 2 % of the cancers in the United States in 2010 [17, 18]. The incidence of CNS tumors for 2008 in the European Union and Sweden is estimated to be 40,000 and 587 persons, respectively [18].¹ The tumors in the CNS are

¹ The latest available report on cancer statistics in the European Cancer Observatory is an estimate from the partly reported data in 2008. The actual statistics are not yet (2012) available due to the delay between the incidence and the annual report.

divided into several categories depending on their region of growing or their origin (Figure 2). The most common intracranial tumors are meningioma, metastases and glioma. Statistics on the tumor incidence rate varies depending on the classification of tumors by the reporting organization [16].

2.2.1 Meningioma and Metastases

Two common intracranial tumor types are meningiomas and metastases. Meningiomas originate from the arachnoid cap cells and include about 35 % of primary intracranial tumors, most of which tend to be slow growing, benign and non-infiltrative [16, 19, 20]. Approximately 8% of meningiomas show aggressive features [21]. Tumor cells can reach the brain through the vessels from other sites of the body, usually breast, skin, lung, kidney and gastrointestinal tract. These tumors called metastases include 10-30 % of the diagnosed brain tumor cases [22].

2.2.2 Glioma

One other common intracranial tumor is glioma which originates from the glial cells and includes about 30 % of all primary intracranial tumors [16]. Common types of glioma are *astrocytic tumors*, *oligodendrogliomas*, *ependymomas* or a mixture of these. Astrocytic tumors (astrocytomas and glioblastomas) are tumors that originate from astrocytes and include tumors of four malignancy grades according to WHO classification. Oligodendrogliomas mostly occur in younger adults and include about 2% of the intracranial tumors [23, 24]. Ependymomas include 2-3% of intracranial tumors and are among the common pediatric tumors [24].

Brain tumors are graded according to the WHO classification. Grade I is benign and grade II is considered as low malignant. Low grade gliomas include 15% of all brain tumors and are common in children and younger adults (~4th decade) [25]. They include astrocytoma, oligodendroglioma and ependymomas [1]. The grade III and IV tumors are considered to be highly malignant. The grade III includes anaplastic astrocytomas, anaplastic oligodendrogliomas or a mixture type. The grade IV tumors include glioblastomas and gliosarcomas [1, 26].

2.3 Glioblastoma

Glioblastoma is the most common aggressive brain tumor with an incidence rate of 3-4 per 100,000 population [1]. The median age of diagnosis is 64 years [21]. The growth of this tumor is relatively fast and infiltrative. Most glioblastomas have an epicenter in the white matter and are accompanied by central necrosis and surrounding edema called gliosis. Border of this tumor appears as similar to the surrounding healthy brain tissue without any clear cut [1]. MR images of a glioblastoma are shown in Figure 3. In the contrast enhanced T1-weighted images (Figure 3-a, c) viable tumor and necrosis are visible. Edema is best visible in a T2-weighted image (Figure 3-b).

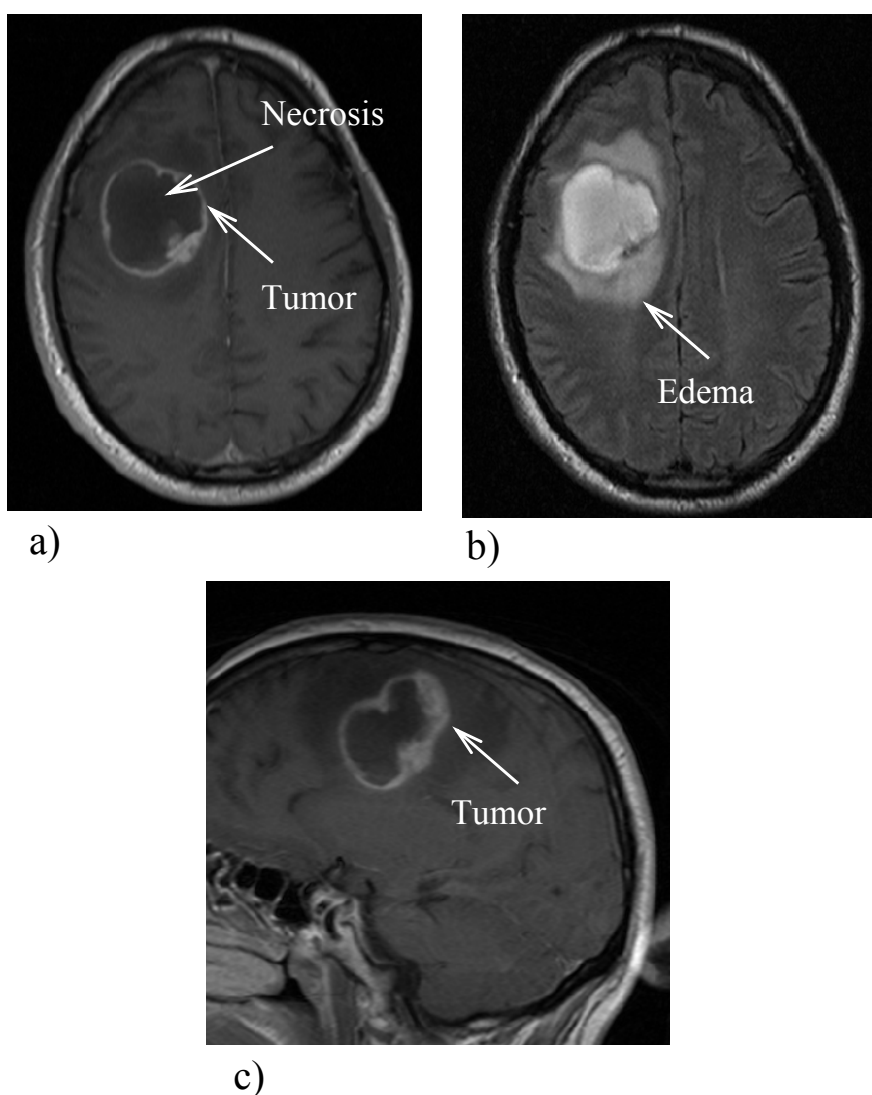


Figure 3 MR image of a glioblastoma: a) T1-weighted with contrast in axial plane, b) T2-weighted in axial plane and c) T1-weighted with contrast in sagittal plane. In a and c, the central dark area is necrosis and in b the surrounding dark area is edema.

2.3.1 Pathology

The histopathology of glioblastoma is variable within one tumor due to its multiform nature. Glioblastoma is generally characterized by aggressive infiltration, abnormal increase of micro-vascularization, necrosis and edema. Pathological diagnosis is based on cellularity, cellular morphology (atypia and mitosis), necrosis and proliferation of vessels; however, tissue pattern plays a greater role in diagnosis [1]. A primary glioblastoma cell's rapid growth induces hypoxia which is considered to be the cause of vascular proliferation [27, 28].

The blood brain barrier is disrupted in the malignant glioblastoma [12, 29] while a lower or no breakdown for BBB in the low grade gliomas is reported [29]. In another

study, vascularity was correlated with glioma malignancy in 131 patients using catheter angiography imaging [30]. Vascular abnormality was seen in angiographic images of 30% of grade II, 40% of grade III and 70% of grade IV gliomas. Capillary abnormalities similar to the primary brain tumors were reported for brain metastases but the capillaries reserved the morphological properties of the capillaries in the tissue of origin [31].

2.3.2 Diagnosis and Treatment

The diagnosis of brain tumors is based on the neurological symptoms and Computed Tomography (CT) or Magnetic Resonance (MR) imaging with the Gadolinium-enhanced MR being the gold standard method for imaging the brain tumors [32]. When MR and CT imaging do not give the right diagnosis, alternative methods are used based on the suspected outcome. Stereotactic biopsy samples are prescribed for small and inaccessible tumors [32]. Positron Emission Tomography (PET) and Magnetic Resonance Spectroscopic Imaging (MRSI) are other methods for diagnosis of glioblastoma. PET provides an image based on the glucose metabolism of the active tumor and is specifically useful when tumor size is below the detectable level by MR due to the undisrupted vessels or when discrimination from edema is desired; e.g. postoperative residual tumor evaluation [32]. MRSI monitors changes in several metabolites which discriminate pathological from healthy tissue and is used to discriminate the malignant from the non-malignant tissue [32]. The brain tumors are commonly removed by radical resection. The surgery can be followed by radiation therapy and chemotherapy or a combination of the radiation therapy and chemotherapy (adjuvant therapy).

2.3.3 Prognosis

The low survival rate and poor prognosis of the GBM is due to the recurrence of the tumor as a result of incomplete resection. The infiltration of glioblastomas and their morphological similarity to the functioning brain tissue hinders the total resection of the tumor. The location of the tumor is another factor which can affect the total removal of the tumor in favor of preserving the neurological function of the brain [33]. The recurrent tumor is in the majority of cases (75% to 90%) found within several centimeters from the original tumor border and in some other cases (5%) in the form of multiple lesions in a distant location. The median length of survival from the time of diagnosis is in the range of 12-18 months with surgery and additional therapy [2, 32, 34]. The 5-year survival rate is stated to be less than 10% [32].

Lacroix et al. have studied the prognosis and survival length of 416 patients in relation to the extent of tumor resection [2]. The extent of resection or gross total resection (GTR) is obtained by comparing the tumor volumes between preoperative and postoperative MR images. Post op MR images were taken shortly after the surgery (usually 24-48 hours) [32]. Resection of 98% or more of the tumor volume is reported to have a significant survival advantage (median of 13 months) compared to the resections less than 98% (median of 8.8 months). Others have also reported the significant influence of a higher resection amount on the survival length of the patients [35]. In a study on 243 patients, Stummer et al. report on improvement in the overall survival from the time of surgery from 11.8 to 16.7 months by achieving total resection [3].

2.3.4 Guidance during Brain Tumor Resection

Traditional open brain surgery is performed using a white light surgical microscope, electrosurgical units and a suction tool leaving the decision of tumor tissue identification to the surgeon alone. Preoperative images are commonly used for localizing the tumor; however, they are not perfectly valid as the tumor has a rapid growth. In addition, the position of brain and brain tumor changes due to a phenomenon referred to as brain shift. Brain shift is caused by a change in intracranial pressure and cerebrospinal fluid loss when the skull is opened. The change of brain volume due to open brain tumor resection is reported to be shrinkage to 60-95% of its original volume (1-9 mm displacement) [36]. The intraoperative tumor visualization modalities used today in clinics are: CT (mobile or stationary), open MRI, neuronavigation (MRI or Ultrasound-based) and fluorescence-guided resection (FGR) [37]. Intraoperative CT and MRI usually require additional resources and adjustments and thus put burden on the cost and time of the surgery [31]. Intraoperative mapping [38, 39] is used in some centers for identification of eloquent areas in the brain where resection should be avoided; however, the method is not in common practice. A short review of commonly used methods is given below:

Intraoperative MRI and CT: MRI is considered suitable in acquiring desired images from brain without exposure to the radiation. However, the cost is a burden and the strength of the magnetic field and thus the image quality of some older intraoperative units might be less than the standard units [31]. Today mobile MR units are available with magnetic field strengths of 0.12 to 1.5 and 3 Tesla [4]. CT has advantages over MRI in that it is less bulky, costs less and can be acquired as a mobile station. CT has the drawbacks of radiation exposure and limited soft tissue discrimination [31, 37].

Neuronavigation: Navigation may be used together with pre-op MR or PET images or ultrasound images. Ultrasound-based navigation is a more convenient and interactive device for the operating room as the ultrasound images are taken intraoperatively. However, the resolution of the images is less than MR images. Preoperative MR images may be optionally registered with the ultrasound images to compensate for the image quality [37, 40, 41].

Fluorescence guided resection (FGR): Fluorescence guidance is a recent method for visualizing glioblastoma [42, 43]. The tissue is marked with a fluorescent contrast and imaged during the operation. Different fluorescence contrast agents have been used; however, recently 5-aminolevulinic acid (5-ALA) has attracted a great attention from all over the world. The observation tool in clinics has so far been the modified white light microscopes for intraoperative visualization of fluorescence. The method is described extensively in Chapter 3.

Chapter 3

Optical Methods

Light is electromagnetic radiation which can act as wave and particle (photons) when interacting with matter. Interaction with tissue affects characteristic parameters of the incident light including intensity, phase, frequency, polarization and coherence. Shift in these parameters can be used in different optical modalities to study the tissue of interest. In this chapter optical topics relevant to fluorescence spectroscopy are reviewed.

3.1 Light Interaction with Tissue

Transmission of light in a medium is referred to as propagation. At the boundary between two media light is usually reflected or refracted (Figure 4). Reflection (specular) is the re-direction of light away from the boundary with the same angle relative to the surface normal. Refraction is the transmitted light through the boundary that propagates in the second medium. Reflection and refraction are functions of the two media's refractive indices. Refractive index, n , of a medium is the ratio of speed of light in the vacuum to the speed of light in that medium as described by Snell's law.

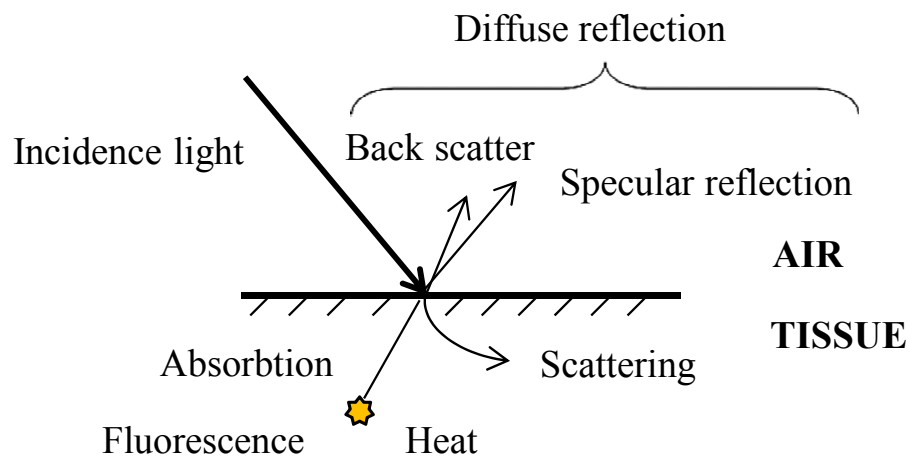


Figure 4 Transmission and reflection of incident light.

At the tissue interface, the part of light that propagates into the tissue goes through either of the absorption or scattering processes. The absorbed photons turn into another form of energy (e.g. heat or fluorescence) and the non-absorbed ones are scattered. The scattered photons propagate into the tissue until they are absorbed or exit the tissue by being backscattered; therefore, the optical properties of tissue can be explained by three main parameters: absorption coefficient, μ_a , scattering coefficient, μ_s , and the anisotropy factor, g .

3.1.1 Absorption

When photons propagate through matter their energy is transferred to the electrons of atoms and molecules in the medium. This process is called *absorption*. The energy of absorbed light is then transformed to heat or is re-emitted as fluorescence. The main absorbers in tissue, so called chromophores, are globins (hemo, myo, neuro and cyto) [44], lipid, water, melanin, and cytochromes [45, 46]. Figure 5 shows the main chromophores of the brain. The region between wavelengths of 600-1000 nm where the main chromophores of tissue have reduced absorption is referred to as the optical *therapeutic window*. Light penetrates the tissue deeper at wavelengths in this window [47].

Absorbance, A , describes the ratio of incident light intensity, I_0 , to the transmitted light intensity through the tissue, I , (Eq. 1) and is a function of extinction coefficient, ϵ [$\text{L mol}^{-1} \text{cm}^{-1}$], optical path length, l [cm], and concentration, c [g L^{-1}]. Absorption in a medium with homogenous absorbers is defined by absorption coefficient, μ_a [cm^{-1}]. $1/\mu_a$ is the average distance a photon travels before an absorption event occurs. The absorption coefficient may be calculated from the extinction coefficient and concentration of the chromophore (Eq. 2) [47, 48].

$$A = \epsilon(\lambda)lc = \log_{10} \frac{I_0}{I} \quad (\text{Eq. 1})$$

$$\mu_a(\lambda) = \epsilon(\lambda)c \quad (\text{Eq. 2})$$

Light intensity attenuation due to absorption in a medium is described by Beer-Lambert law (Eq. 3). Light attenuates exponentially with μ_a and l [47]:

$$I = I_0 e^{-\mu_a(\lambda)l} \quad (\text{Eq. 3})$$

3.1.2 Scattering

Scattering is the re-direction of light by small particles and depends on the size of the scattering particles. *Mie* scattering occurs when the particle dimension is in the same order of the light's wavelength and *Rayleigh* scattering occurs when the particle is much smaller than the wavelength of light. Cell organelles such as nuclei, mitochondria and collagen fibers have dimensions comparable to light wavelengths (Mie) whereas membrane and ultrastructure are much smaller than the light wavelength (Rayleigh). Both Rayleigh and Mie scatterings are elastic; i.e., the scattered photons have the same frequency and wavelength as the original light. Scattering of a medium is characterized by the scattering coefficient, μ_s [cm^{-1}] and $1/\mu_s$ is the average distance a photon travels before a scattering event occurs. Unlike Rayleigh and Mie, *Raman scattering* is inelastic where the scattered light has a frequency shift which is proportional to the vibrational frequency of the scattering particles. The vibrational frequency is specific for each molecule or substance [47, 49, 50].

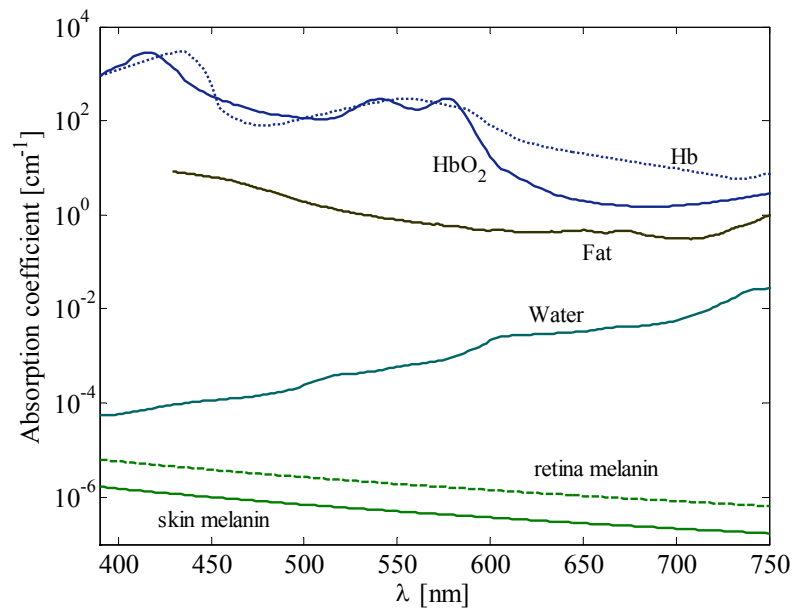


Figure 5 Absorption spectra of the main tissue chromophores: water [51], fat [52] and melanin[53]; data were provided by Prahl.

3.1.3 Phase Function and Anisotropy Factor

When striking a particle light scatters in different directions. The scattering profile of each particle is called phase function, $p(\hat{s}, \hat{s}')$. The scattering phase function is the probability of light propagating in direction \hat{s} to scatter in direction \hat{s}' with a scattering angle of θ (Figure 6) also written as $p(\theta)$. Notations and explanations are different in various literature on bio-optics; therefore, the equations are uniformly explained according to one reference only [47]. Considering that scattering is symmetric relative to direction \hat{s} , Eq. 4 can be written:

$$\int_0^{\pi} p(\theta) 2\pi \sin\theta d\theta = 1 \quad (\text{Eq. 4})$$

In isotropic conditions $p(\theta) = 1/4\pi$ where 4π is the number of Steradians in a sphere. In tissue, light is scattered both in the forward and random directions, so called anisotropically scattered. To simplify the formulation of anisotropic scattering, the average of the cosine of all scattering angles, $\langle \cos\theta \rangle$, is used to describe the degree of anisotropy in form of the anisotropy factor, g (Eq. 5). When $g = 1$, all the light is forward scattered. The anisotropy factor is wavelength dependent and varies for different tissues ($g = 0.6-0.98$) [50, 54, 55].

$$g = \int_0^{\pi} p(\theta) 2\pi \cos\theta \sin\theta d\theta = \langle \cos\theta \rangle \quad (\text{Eq. 5})$$

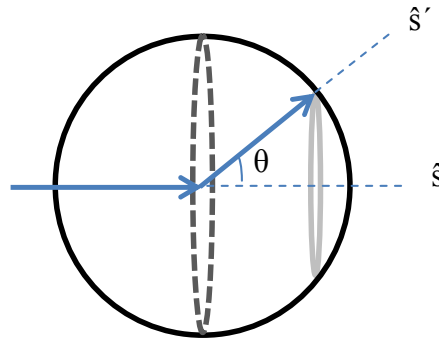


Figure 6 A single scattering event and the corresponding geometry.

3.1.4 Reduced Scattering

Photons in the tissue are mostly anisotropically and forward scattered. If sufficient amount of scattering occurs before the photon is absorbed, scattering in tissue may be defined in terms of the reduced scattering coefficient, μ'_s according to Eq. 6 [47]. Reduced scattering describes scattering of the photons in step sizes of $1/\mu'_s$ also called reduced mean free path (mfp'). Each mfp' considers isotropic scattering [56].

$$\mu'_s = \mu_s (1 - g) \quad (\text{Eq. 6})$$

Reduced scattering is useful in describing the scattering of photons in a scattering dominant medium where μ'_s/μ_a of the medium is greater than ten [57].

Figure 7 illustrates the concept of reduced scattering. In this case $1/\mu'_s$ is the mfp' of ten steps of mfp for $g = 0.9$ [56].

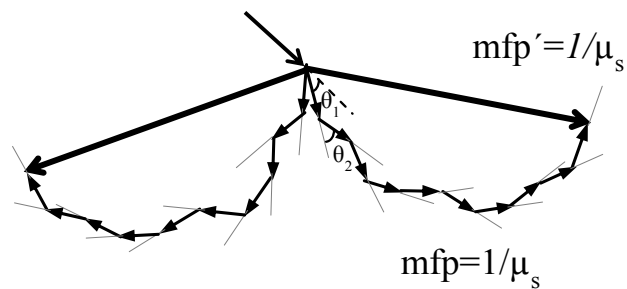


Figure 7 Mean free path and reduced mean free path.

3.1.5 Total Attenuation and Penetration Depth

For a turbid media, where both absorption and scattering are present, the total attenuation coefficient, μ_t , is calculated according to Eq. 7. Albedo is a commonly used concept that defines the amount of scattering to the total attenuation (Eq 8).

$$\mu_t = \mu_s + \mu_a \quad (\text{Eq. 7})$$

$$\text{albedo} = \frac{\mu_s}{\mu_t} \quad (\text{Eq. 8})$$

Penetration depth of light, D , may be calculated from Eq. 9 when the media is forward scattering (tissue) [48, 50]:

$$D = \frac{1}{\mu_t} \quad (\text{Eq. 9})$$

3.1.6 Optical Properties of Brain Tissue and Blood

Different optical properties (n , μ_a , μ_s and g) are reported for the different brain tissue types, namely gray and white matter and different malignancy types and grades (Table 1). The optical properties reported by Yaroslavsky [58] were investigated on the non-diseased human brain 48 hours post mortem and on the tumor samples extracted during surgery. Optical properties of blood (n , μ_s , μ_a and g) illustrated in Figure 8 are provided in the literature derived experimentally and theoretically [59, 60].

Table 1. Optical parameters of human brain and human brain malignancies [cm^{-1}].

Tissue type	$\lambda= 405 \text{ nm}$				$\lambda= 510 \text{ nm}$				$\lambda= 635 \text{ nm}$			
	n	μ_a	μ_s	g	n	μ_a	μ_s	g	n	μ_a	μ_s	g
White matter [58]	-	3	400	0.75	1.36 ^a	1	426	0.81	1.36 ^a	0.65	400	0.84
Gray matter [58]	-	2.5	150	0.86	1.36 ^a	0.4	106	0.88	1.36 ^a	0.18	100	0.9
Glioma grade II [58, 61]	-	20	20	0.86	-	2	180	0.94	-	0.9	110	0.96
Glioma grade III [61]	-	14	75	0.86	-	6.5	60	0.89	-	4	45	0.89
Meningioma [58]	-	4	100	0.91	-	0.8	200	0.94	-	0.3	180	0.95

^a Roggan [62]

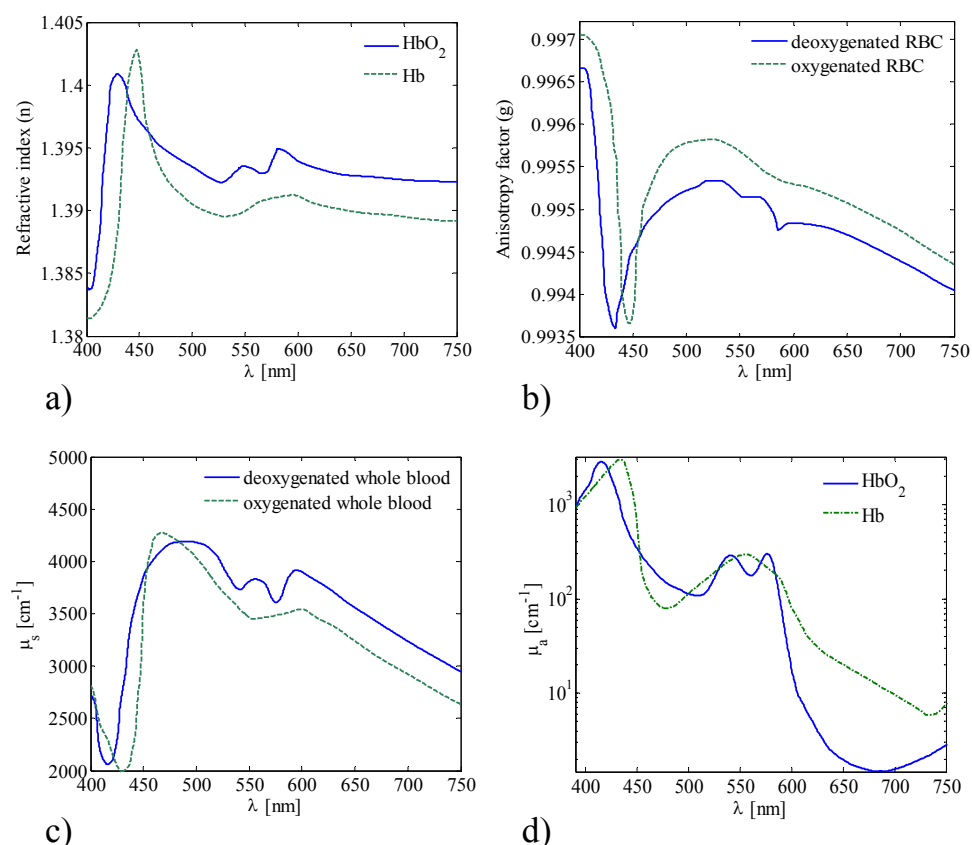


Figure 8 Optical properties of oxygenated and deoxygenated blood. a) Real part of the refractive index of deoxy and oxyhemoglobin, b) anisotropy factor (g) of the red blood cells, c) scattering coefficient (μ_s) of whole blood and d) absorption coefficient (μ_a) of hemoglobin. a-c is derived from [59] and d is from [60]. (Figs a-c): Copyright (2004) by the American Physical Society. Reprinted with permission for minor adaptations from [59]

3.2 Fluorescence

Electrons of specific molecules reach a higher energy level (S_1 or S_2) as a result of exposure to excitation light. Excited electrons usually relax to the lowest vibrational level of S_1 (internal conversion) first, and then return to their ground state (S_0) and release energy as fluorescence. A typical Jabłoński diagram in Figure 9 shows the principle of fluorescence emission. A fluorophore is a molecule which in exposure to an excitation light re-emits light of a longer wavelength since part of the excitation light energy is absorbed by the molecule. The time that the fluorophore stays in the excited state before it returns to the ground state is referred to as the fluorescence *lifetime*. Each fluorophore has a specific absorption and emission band. The excitation can occur at several different wavelengths where a fluorophore absorbs light; the emission response to any excitation is constant. The number of photons emitted in proportion to the number of photons absorbed, referred to as *quantum yield*, is a measure for fluorescence emission. Quantum yield is in addition to the fluorophore itself affected by the environment of the fluorophore [63].

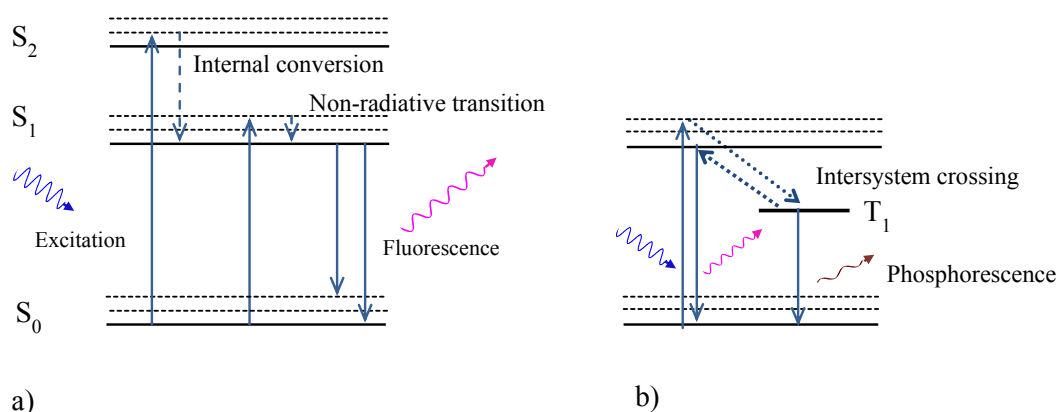


Figure 9 Typical Jablonski diagram [63]. S_0 is the singlet ground and S_1 and S_2 are the first and second electronic states. The dashed lines at each electronic state are the vibrational energy levels. a) Shows the typical fluorescence and b) shows the delayed fluorescence where electrons have a transit to the triplet state.

By theory, excitation of electrons to a higher energy level and return to the ground state may be repeated plenty of times without loss of fluorescence. In practice, this is not possible as some excited electrons decay to their triplet state, T_1 , (intersystem crossing) where they return to the ground state and release their energy as phosphorescence or react with other molecules including oxygen. As a result of interaction with oxygen a bi-product of the fluorophore is formed. Destruction of fluorophores and loss of fluorescence caused by light exposure is called *photobleaching* [47, 63].

Photobleaching may be undesired or desired depending on the application. When performing fluorescence diagnostics, minimal photobleaching is desired. On the other hand, photodynamic therapy (PDT) is a type of treatment that uses photobleaching of an applied photosensitizer for production of toxic singlet oxygen to destruct the target cells. PDT is used in treatments of various dermatological conditions ranging from bacterial and fungal infections to different types of tumors [64, 65]. Photochemical reactions differ based on the environment and availability of oxygen. In anoxic and hypoxic environments the reaction is dependent on target-substrate concentration (Type I). In oxygenated environments the excited photosensitizer reacts with easily excited triplet state oxygen where the reactions are oxygen dependent (Type II). Type II reactions are dominant in PDT, however, Type I reactions might increase at high photosensitizer concentrations [66].

3.3 Excitation and Detection of Fluorescence

To detect fluorescence of the desired fluorophore, light sources and light detectors should be matched with absorption and fluorescence emission bands of the fluorophore. The light source is usually a laser with a wavelength where the corresponding fluorophore has considerable absorption. Optical phenomena are commonly measured and visualized as one dimensional point measurement and two-dimensional imaging. The optical information may be collected from one single point or a two dimensional surface area.

3.3.1 Light Detectors

The principle of light detection is based on converting the interaction of light and matter into an electrical signal. The most common and basic photodetectors are photomultipliers (PMTs) and photodiodes (PDs) which measure a single point only. To obtain a spatial scan, an array of photodetectors is required. Charged coupled Devices (CCDs) are among the commonly used detectors for spatial detection [47].

In photo-diodes incidence photons result in increased conductivity of the semiconductor material and generate an electrical signal proportional to the photons. Avalanche photodiodes are a suitable type for the detection of weak optical signals. Photomultiplier tubes multiply the effect of incidence photons by ionization in multiple electrodes [47].

CCDs are widely used in spectroscopy and offer fast and sensitive spatial measurements. They can be built in one or two dimension arrays of photodiodes; the latter for two dimensional image construction. A typical CCD-based spectrometer consists of a slit which restricts the entering light, thereafter light is collimated. Using a grating, light at different wavelengths is reflected at different angles onto the detector array. Spectrometers may be chosen for each application based on the desired wavelength ranges and resolution [48].

3.3.2 Optical Fibers

Optical fibers generally consist of a core, cladding and jacket (Figure 10). Light is transmitted through the core of the fiber by being internally reflected due to the higher refraction index of the core. The acceptance angle of the fiber, referred to as the numerical aperture (NA), is a specification of optical fibers that describes the range of angles within which the fiber accepts or emits light. Supposing that n_{co} is the refraction index of the core, and n_{cl} is the refractive index of the cladding, NA and θ , the angle of light with the axis going through the fiber center, can be calculated from Eq. 10 [48, 67]:

$$NA = \sin\theta = \sqrt{n_{co}^2 - n_{cl}^2} \quad (\text{Eq. 10})$$

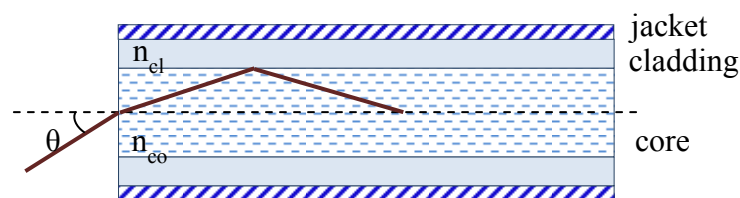


Figure 10 Structure of an optical fiber [48, 67].

Chapter 4

Fluorescence-Guided Resection of Brain Tumor

Using fluorescence for demarcating the tumor to guide the resection is widely known as fluorescence-guided resection. This chapter reviews the native tissue fluorescence components, photosensitizers, specifications of 5-aminolevulinic acid (ALA) and its current status in fluorescence-guided resection.

4.1 Tissue Fluorescence

Nicotinamide adenine dinucleotide (NADH), flavin, collagen, elastin, porphyrins, tryptophan, and lipopigments are the most common tissue fluorophores so called endogenous fluorophores. Collagen and elastin are structure related fluorophores. Flavin, NADH and porphyrin are related to the cellular metabolism [68]. Autofluorescence is the total fluorescence emission of the intrinsic fluorophores in the tissue when the tissue is exposed to the appropriate excitation light (usually in the UV region). The main fluorophores that contribute to the tissue autofluorescence are listed in Table 2 with their absorption and emission spectra shown in Figure 11. The amount of these fluorophores varies in different tissues making the pattern and intensity of the autofluorescence different from tissue to tissue. NADH, tryptophan, elastin and collagen are considered as an indicator for tumor tissue when altered [68]. The autofluorescence is reported to be less [69-72] and red shifted [70-72] in the tumor tissue relative to autofluorescence in the normal tissue. The reason to this lower autofluorescence intensity is not well known and can be related to the metabolic change of the tumor and/or other cancer related parameters which alter the optical properties of the tissue. For instance, in colon cancer it is shown that the collected submucosa fluorescence is reduced due to a thicker mucosa and higher blood content of the in vivo tumor tissue resulting in lower autofluorescence collected in the tumor tissue [70].

Table 2: Main fluorophores contributing to tissue autofluorescence [73, 74]

Fluorophore	max excitation λ [nm]	max emission λ [nm]
NADH	260, 350	460
Collagen	340	390
Flavin	210, 260, 390, 460	520
Lipopigments	350	560
Porphyrin IX	400	635, 704
Elastin	350	410
Tryptophan	215, 275	340
Pyrooxidane	311	394

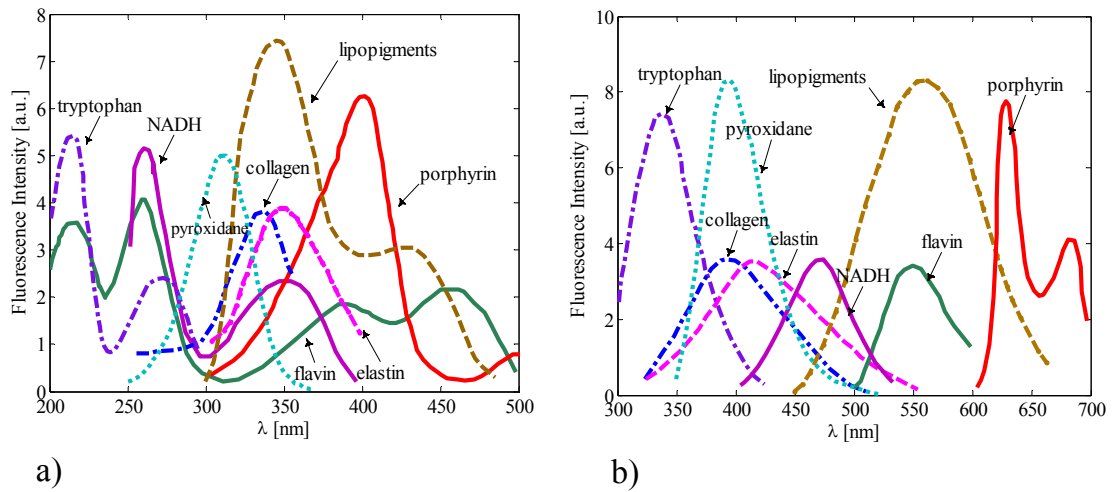


Figure 11 a) Absorption and b) emission spectra of tissue fluorophores. Copyright (1998) by John Wiley and Sons. Reprinted with permission for minor adaptations from [74]."

4.1.1 Brain Tissue Fluorescence

Tissue fluorescence, also called autofluorescence, has previously been investigated as a potential signature for differentiating between the normal and malignant brain tissue [69, 75, 76]. However, due to the difficulty of interpreting the signals [77] no reliable algorithms using autofluorescence for distinguishing brain tumor from healthy tissue has entered the clinical routine.

The main endogenous fluorophores in the brain are NADH, flavin, lipopigments, and porphyrin. The proportion of these fluorophores in the tumor compared to normal tissue depends on the tumor type and the type of normal brain tissue (gray or white) the comparison is made with [71, 75, 76]. Andersson et al. reported on increased porphyrin in the viable tumor [69]. Croce et al. reported the autofluorescence level to be lower in the tumor than in the normal brain tissue however they did not specify the type of normal brain tissue to be white or gray matter [71]. No red shift on the position of the maximum of the autofluorescence was observed by Lin et al. in GBM compared to the normal tissue [78].

4.2 Photosensitizers

Photosensitizers, also known as exogenous fluorophores, either directly or indirectly induce fluorescence in the target tissue. They are used when the intrinsic fluorophores are not adequate for the desired application and may be applied intravenously, orally or topically. Porphyrin, chlorin and bacteriochlorin based drugs are the common photosensitizers in use [66]. Specifications of the most common photosensitizers used in clinical brain tumor studies are summarized in Table 3.

One early porphyrin-based photosensitizer was hematoporphyrin derivative (HPD) which then developed into photofrin, a purified version of hematoporphyrin. Both of these photosensitizers have disadvantages including long skin photosensitivity and variation among batches, as they are a mixture of different porphyrins [79]. Photofrin is however a clinically approved drug and among the commonly used photosensitizers for brain tumors. The fluorescence emission is dark red and difficult to see [80]. Pure compounds arrived later into the practice. These include meta-tetra hydroxyphenyl chlorin (mTHPC) and aminolevulinic acid (ALA). mTHPC also known as Foscan[®], is a chlorin based photosensitizer with high photodynamical activity which makes it achieve comparable results with other photosensitizers at lower drug and light dose. Skin photosensitization is up to 20 days for Foscan[®] [66]. ALA, also known as 5-ALA, is an indirect photosensitizer which pronounces the production of PpIX in the cells. Esterified ALA derivatives result in a higher fluorescence in the tumor cells due to their higher lipophilicity which facilitates their passage through the cell membrane. The ALA esters (methyl, hexyl and benzyl ALA) have a more homogenous distribution relative to ALA when applied to skin [81]. The ALA esters are only tested on glioma cell lines [81] and not on human glioma in vivo yet.

Table 3- Specification of photosensitizers used in the clinical studies within neurosurgery

photosensitizer	Excitation λ [nm]	Emission λ [nm]	Skin protection relative to surgery time	Application
HpD [82]	400	600-700	2-3 months	24 h before intravenously
Photofrin (porfimer sodium) [83, 84]	370-400	630	2-3 months	48h before intravenously
mTHPC (Foscan[®]) [85]	405	652	4 days before	4 days prior to craniotomy/intravenously
ALA [42]	400	600-700	24 hrs after; at high doses	Oral administration 2-3 hours before the craniotomy

Selection of an appropriate photosensitizer is based on its high tumor selectivity, low skin photosensitization and the optimum excitation and emission bands. As photosensitizers were primarily used for photodynamic therapy they were designed on the basis of having a high singlet oxygen quantum yield to achieve phototoxicity. One other challenge has been to choose photosensitizers with high absorption at longer wavelengths (near infra-red) to increase the penetration depth of excitation light and thus the treatment depth [66]. The photosensitizer (5-ALA) in this thesis was chosen based on the optimum uptake by the target brain tumor cells, photo-physical properties, compatibility with the available microscopes and the maximal comfort for the patient which is oral administration and low skin photosensitization. Excitation and emission characteristics of PpIX are shown in Figure 12. ALA has so far been successfully applied in dermatology, urology, neurosurgery, otorhinolaryngology, gynecology and gastroenterology [6]. ALA is approved for clinical use in Europe since 2007 and for clinical trials prior to approval in the USA, Australia and some Asian countries.

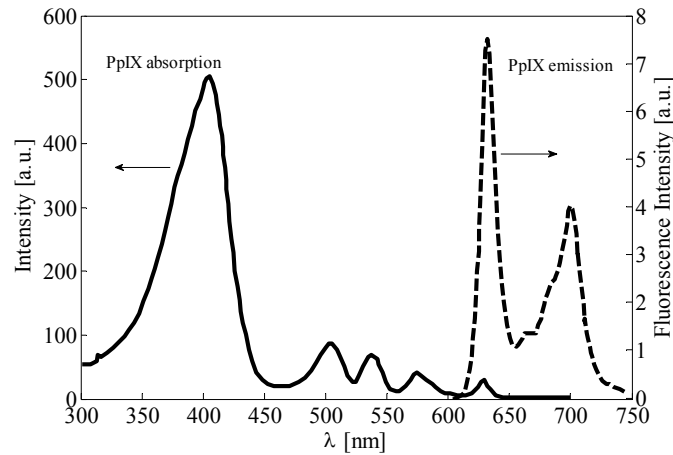


Figure 12 Absorption and emission spectra of PpIX. Copyright (2003) by Springer. Reprinted with permission for minor adaptations from [86].

4.3 Specifications of ALA

The first clinical application of ALA for tumor demarcation occurred in the 1980s by several investigators in parallel [87]. ALA can be applied topically or systematically (orally or intravenously), however, oral administration of ALA was preferred in all the human studies conducted at different centers so far. Skin photosensitization due to ALA is seen up to 24 hours after application of 20 mg/kg body weight [42].

Naturally, ALA exists in the heme synthesis cycle where heme is produced by the binding of PpIX to iron. Several enzymatic steps are involved in this process half of which are mitochondrial and the other half cytoplasmic (Figure 13). The final steps of PpIX and heme production occur in the mitochondria of cells giving a cellular distribution pattern to PpIX [88-90]. Selective accumulation of PpIX in brain tumors is affected by several parameters including:

Disrupted BBB: The BBB in general has a poor permeability to the 5-ALA, disregarding the 5-ALA concentration changes in the plasma [91]. The BBB in high-grade primary and metastases brain tumors is more permeable than the normal brain BBB [31, 89].

Altered pattern of enzyme activity: Ferrochelatase enzyme helps the iron to be added to the PpIX thus a deficiency of ferrochelatase (FC) in tumors hinders the change of PpIX to heme. Other enzymes/substances whose amounts are different in tumor tissue might affect the production of PpIX to heme: ALA synthase enzyme (ALAS), ALA dehydrase (ALAD) and porphobilinogen (PBG) [88, 90, 92].

Iron level: Iron is effective in accumulation of PpIX as its interaction with PpIX produces heme. Tumors take up iron more rapidly and have a lower iron level [86, 90, 93]. A study by Valdés [94] reports on the application of iron chelation to increase the fluorescence level of PpIX in brain tumor FGR. Iron chelation reduces the availability of free iron and thus reduces the breakdown of the PpIX to heme.

Temperature: A slightly elevated tumor temperature increases the activity of porphobilinogen deaminase (PBGD) enzyme and thus impedes production of PpIX [93].

pH: PpIX production is maximal at the physiological conditions of pH = 7 and is reduced under the acidic condition. A low extracellular pH value in the tumor might reduce the PpIX accumulation. Intracellular pH is not considered to affect the PpIX accumulation [90].

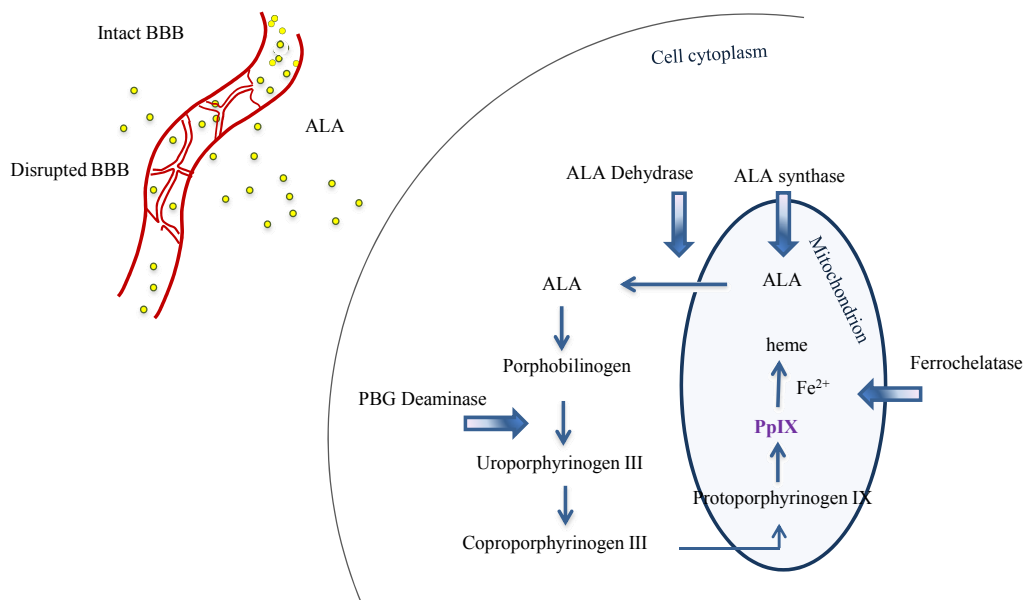


Figure 13 Transformation of 5-ALA into PpIX in the mitochondrion of a cell [90].

4.4 Clinical Studies based on ALA Guided Brain Tumor Resection

In the last decade several groups have investigated the potential of ALA based FGR in neurosurgery. Stummer et al. were the first to conduct an extensive clinical study on the extent of tumor resection using ALA [3]. The main studies were primarily performed using modified white light microscopes. The focus in most of these studies was to evaluate the sensitivity and specificity of the method, gross total resection achieved and the potential of combination with other intraoperative imaging modalities. Two groups have used endoscopy for qualitative imaging of deep-seated malignant glioma [95, 96]. A few groups in recent years have commenced the fiber-optical probe measurements for quantified analysis of fluorescence [97]. All of these studies orally administered a dose of 20 mg/kg body weight ALA dissolved in water as instructed by Stummer and colleagues [42].

Among all the brain tumors, glioblastoma is the main target for ALA; however, recurrent GBM, meningiomas, anaplastic astrocytomas, recurrent astrocytomas and the majority of metastases are reported to have taken up ALA [98-101]. Additionally, lymphoma and pituitary adenoma have exhibited fluorescence [101]. Low grade gliomas have been controversial in exhibiting fluorescence. In a prospective study Widhalm et al., correlate the availability of PpIX fluorescence in the low grade tumors to their malignant

progression within the one year follow-up period [102]. In rare cases GBM is reported not to have given any fluorescence [98, 101]. Table 4 summarizes the fluorescence response observed in various studies in tumor types other than GBM.

Table 4- Fluorescence in the tumor types other than GBM

Tumor type	Fluorescence response Pos	Fluorescence response neg
Low grade glioma	Widhalm [102]	Hefti [98], Widhalm [103]
Oligodendroglioma (WHO III)	Feigl [104], Widhalm [103]	Widhalm [103]
Astrocytoma (WHO III)	Ishihara [97], Widhalm [103], Eljamel [101]	-
Recurrent GBM	Nabavi [105]	-
Gliosarcoma	Johansson [106], Stummer [3]	-
Meningioma	Hefti [98], Bekelis [107], Kajimoto [108], Coluccia [109]	-
Metastases	Hefti [98], Utsuki [100], Kamp [99], Eljamel [101]	Kamp [99], Eljamel [101]

4.4.1 Fluorescence Microscopy

White light surgical microscopes were modified to detect PpIX fluorescence, first reported by Stummer et al., [110]. In a commercial fluorescence microscope, blue light (390-410 nm) is provided through filters using a high power Xe-lamp (~ 400 W). During the white light mode, the blue part of the illumination is omitted to reduce photobleaching of PpIX. A long-pass filter (450-720 nm) then omits the blue reflection from the observation spectra [111]. The general configuration of the microscope is presented in Figure 14. After fluorescence microscopes became commercially available, several other groups performed similar clinical studies using the microscope. The healthy tissue is viewed as blue as a result of the excitation light reflection and the tumor is viewed as pink or red due to the PpIX fluorescence (Figure 15). The fluorescence in the microscope is usually evaluated as weak and strong or present and absent. Table 5 summarizes several major studies conducted using fluorescence guidance and the results achieved. The same dose of ALA was applied by all groups but different approaches were taken regarding tumor types, complementary modalities and the evaluation method. It should be considered that in studies conducted by means of microscopy, in some cases the fluorescence might have been weaker than the detection threshold of the microscope and the eye; therefore, classified as negative by the authors. In several of these studies fluorescence guidance was combined with additional monitoring modalities including MR, CT, PET, MR based neuronavigation and microelectrode recording (MER).

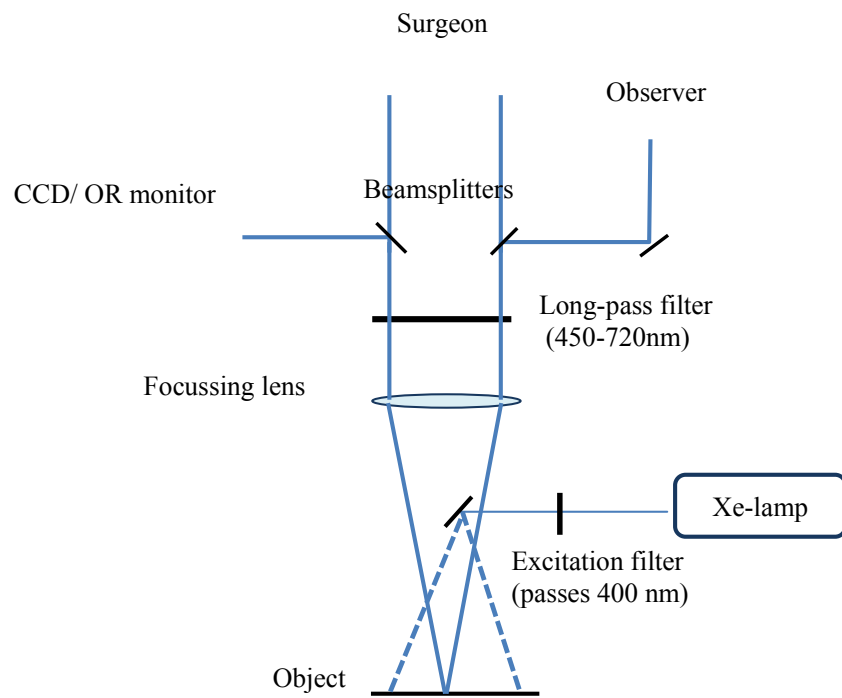


Figure 14 General configuration of a fluorescence microscope [110, 111]

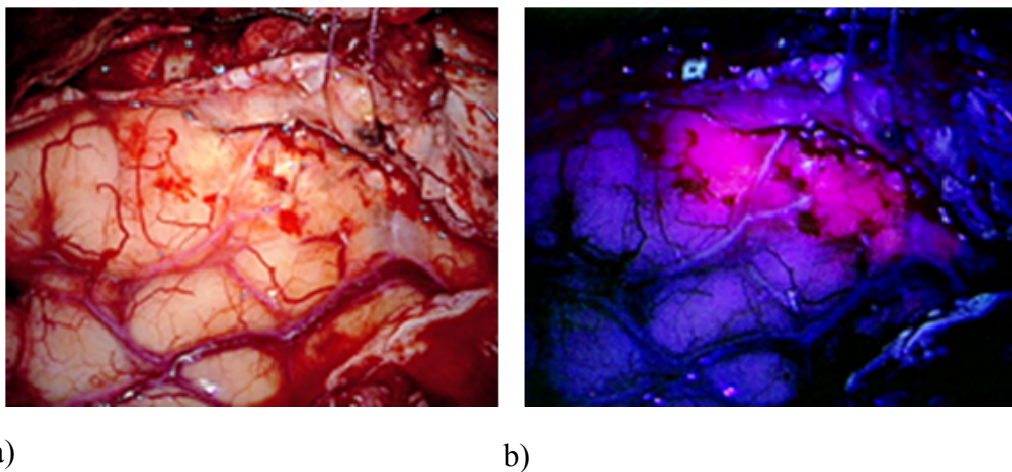


Figure 15 Image of Glioblastoma IV taken by a Carl Zeiss BLUE 400 microscope: a) under white light illumination and b) under blue light illumination (Courtesy of Walter Stummer, M.D., University of Düsseldorf, Düsseldorf, Germany).

Table 5- ALA based FGR conducted at various centers

Group	Patients	Additional modalities	Results
Stummer 2000[112]	52 pat	-	GTR achieved in 63% of patients
Utsuki 2007[100]	42 pat	-	Sn=100%
Ishihara 2007[97]*	6 pat	-	High sp
Stummer 2008[3]	243 pat	-	GTR=78% with FI, GTR=44% with WL
Hefti 2008 [98]	74 pat	FI microscopy on biopsies	Solid fl: Sp=100%, sn=98% Vague fl: sp=76%, sn=85%
Nabavi 2009 [105]	36 pat	-	PPV=96.6 TP is higher in strong fl
Feigl 2010[104]	18	MR neuronavigation, MER	GTR achieved in 64% of patients
Widhalm 2010 [103]	17 pat	Co-registered PET+MR in neuronavigation	Pathology correlates with fl
Panciani 2011 [113]	23pat	Co-registered CT+MR in neuronavigation	Sn=91.1%, sp=89.4% Combination: improved sp, lowered sn
Valdes 2011[114]*	14 pat	DRS	Higher efficiency for spectroscopy vs. microscopy

*Fluorescence spectroscopy

Definitions: Ppv: positive predictive value, TP: true positives, sp: specificity, sn: sensitivity, FI: fluorescence.

4.4.2 Fiber-Optical Based Fluorescence Spectroscopy

Monitoring fluorescence of PpIX in gliomas using a fiber optical probe was thoroughly investigated by several groups. Ishihara et al. reported on high specificity of fluorescence spectroscopy on 65 tumor samples (6 patients) in vitro. The signals were quantified then compared to the macroscopic observation through a long-pass filter. Spectroscopy could detect weak fluorescence invisible to the eye [97]. Utsuki et al. reported on a spectroscopy device capable of detecting weak fluorescence invisible to the eye. No quantification was considered in this work [115]. At Dartmouth, ALA spectroscopy was compared to microscopy methods. The fluorescence signals were quantified by estimating the PpIX concentration using combined fluorescence spectroscopy and diffuse reflection spectroscopy (DRS). The group obtained 66 % efficiency using fluorescence microscopy and 87 % efficiency using fluorescence spectroscopy [114].

4.5 Fluorescence Intensity and Quantification Methods

Various attempts were made to quantify the tissue fluorescence intensity. The main concern has been to calculate intrinsic fluorescence for obtaining concentration of the target fluorophore. Intrinsic fluorescence is the original fluorescence which is not affected by the absorption and scattering of the medium and reflects the original amount of the target fluorophore. One other concern has been to cancel out the variation of the excitation fluence rate due to geometrical properties of the optical probe and the position of the probe relative to the tissue.

4.5.1 Fluorophore Concentration and Quantum Yield

Fluorescence intensity is to a great extent affected by its concentration and quantum yield in the tissue. The quantum yield for PpIX is mentioned as being 0.5% [116, 117]; however, it may vary depending on the environment [64, 118]. The concentration and the fluorescence intensity of PpIX have shown linear proportionality ($R^2 = 0.99$) when known amounts of PpIX were mixed with dissolved human GBM tissue in the lab [106]. Kim et al., also report the PpIX fluorescence intensity and the known PpIX concentration as being linearly proportional ($R^2 = 0.64$) in the optical phantoms made of intralipid and food color [116].

4.5.2 Quantification Methods

The intrinsic fluorescence has been calculated by various methods of combining the fluorescence measurements with reflection spectroscopy, Monte Carlo simulation, application of optical theories, controlled measurements using specific probe design or fluorescence-based methods [68]. However, in clinical practice imposing additional procedures is not desirable and should be implemented only if there is a significant improvement to the diagnosis. A review on these methods is included in this section.

Theoretical and Monte Carlo Approach

The main goal of the theoretical based methods have been to obtain a transfer function that calculated the intrinsic fluorescence from the measured fluorescence [68]. This was done through describing light propagation in the medium using a relevant theory. In absorption dominant media Beer-Lambert law was used and in the scattering dominant media ($\mu'_s \gg \mu_a$) diffusion theory was used. Most of these methods were dependent on diffuse reflection spectroscopy for deriving the tissue optical properties [119].

Monte Carlo simulations have been used to derive equations describing the fluorescence attenuation without putting a restriction on the probe geometry, absorption and scattering properties of the tissue. However, the tissue's optical properties should have been previously known, or was extracted by reflection spectroscopy, in addition to the long simulation times which are not clinically applicable [68, 120].

Combination with Additional Optical Modalities

Diffuse reflection spectroscopy has been commonly used to correct for attenuation caused in the fluorescence. Different functions are calculated based on fluorescence and reflectance values at selected wavelengths [121-123]. One other suggested method of combining fluorescence with reflection is to consider the fluorescence-reflection ratio at a specific optimum distance. The method is valid over a restricted range of absorption and scattering coefficients [68, 124].

Fluorescence-Based Methods

To only take advantage of the fluorescence measurements without using additional modalities, some methods controlled the probe set up to collect the photons which have taken the least path length and are thus less distorted. Based on this concept, the use of a

single fiber for excitation and collection, was suggested [125]. A ratio of fluorescence peak and the reflection of excitation light has also been used for signal quantification [97]. Further approaches use a ratio of fluorescence signal obtained by a single excitation source or from two excitation sources for correction of the fluorescence signal [126, 127].

Two simple methods of quantifying the fluorescence signal by defining ratios are described by Sterenberg using single and double excitation [126]. The main purpose is to cancel out the effect of variations in the incident excitation fluence rate and have a better estimation for PpIX concentration in skin. The first method considers taking the ratio of fluorescence in the red region to the fluorescence in the yellow region (ex= 405nm). A normalized fluorescence ratio (NFR) is defined as Eq.11 from which PpIX's concentration may be further calculated [127]:

$$\text{NFR} = \frac{(F_{\text{PpIXpeak}} / F_{\text{autofl}})_{\text{PpIXpresent}}}{(F_{\text{autofl}} / F_{\text{autofl}})_{\text{noPpIX}}} \quad (\text{Eq. 11})$$

The double excitation method takes the ratio of PpIX/autofluorescence emission resulting from two different excitation wavelengths (Pålsson: 337 and 405 nm; Sterenberg: 405 and 435 nm). Laser at 405 nm is chosen for maximum excitation of PpIX and the second one is chosen at a wavelength where PpIX is low but tissue fluorescence is high [127]. In Pålsson's work single and double ratio evaluation do not show a significant difference in differentiating normal from malignant brain tissue; however, the samples are too few for a concrete conclusion [128]. Sterenberg claims to omit the skin color effect by the double ratio evaluation and that the two excitation ratio is only useful for low fluorophore concentrations. By defining DR (Eq. 12) as a ratio of the collected emission fluorescence signals excited by the two laser sources, the concentration of the target fluorophore can be further estimated [126, 127]:

$$\text{DR} = \frac{(F_{\text{PpIXpeak}} / F_{\text{autofl}})_{\text{ex1}}}{(F_{\text{PpIXpeak}} / F_{\text{autofl}})_{\text{ex2}}} \quad (\text{Eq. 12})$$

Chapter 5

Aim of the Thesis

The aim of the thesis was to evaluate fluorescence spectroscopy for quantitative demarcation of glioblastoma. The following points were specifically considered in the thesis:

- Development and evaluation of a system suitable for guided brain tumor resection in the operating room
- Fluorescence signal quantification, identification of and correction for error sources
- Investigation of the photobleaching behavior and adjustment of the system for introducing minimal photobleaching
- Clinical studies and comparison of the quantified fluorescence signals with diagnosis of the surgeon and the clinical gold standards

Chapter 6

The Fluorescence Spectroscopy System

A fiber-optical based fluorescence spectroscopy system was developed to excite and detect the fluorescence of PpIX in the brain tumor. The system is referred to as optical touch pointer (OTP) throughout the thesis. To meet the requirements of the operating room, the system was designed to omit the ambient light. In this chapter the system setup, its technical specifications and optical parameters that affect the fluorescence signals are described. The system settings were chosen as a compromise between considering sufficient signal intensity and the results described in Chapter 8 for inducing minimal photobleaching.

6.1 System Specifications

The system was developed with both continuous wave (CW) and pulsed (PL) operating modes. A near-UV laser module with nominal wavelengths of 405 nm with the maximal power of 50 mW (Oxxius SA, Lannion, France) was used as the light source for the excitation of PpIX. The laser pulses and power are controlled through TTL and analogue inputs. A fiber-port comprised of a lens and micro-positioner was fixed between the laser and the fiber connection to focus the laser beam into the fiber (OFR, Inc., Caldwell, NJ, USA). A spectrometer (EPP 2000, Stellarnet, Tempa, FL, USA) was used for collection of the fluorescence spectrum. The spectrometer is a 2048 elements CCD with a wavelength resolution of 3 nm collecting spectra in the wavelength range of 240-850 nm. To omit the back-reflected laser light from the tissue a long-pass filter with cutoff wavelength at 475 nm (Schott CG-GG-475-0.50-3, CVI, Melles Griot, Albuquerque, NM, USA) was mounted in a housing with focusing lenses in front of the spectrometer. Through a data acquisition card (National Instruments, Inc., Austin, TX, USA) with triggering alternative, the laser pulses and the spectrometer were synchronized. The design of the system is shown in Figure 16. All the components were placed in a portable.

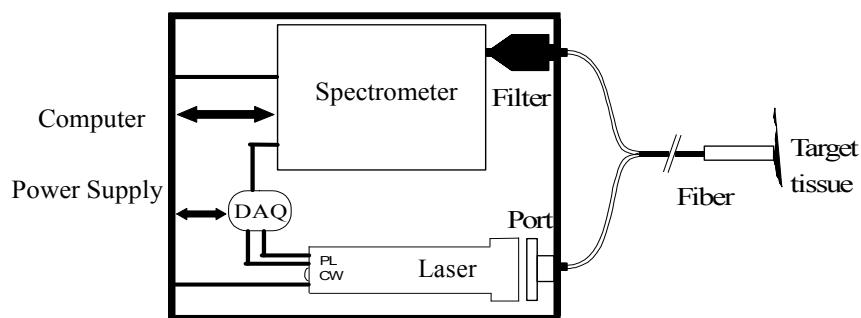


Figure 16: Fluorescence spectroscopy system. Copyright (2010) by John Wiley and Sons. Reprinted with permission from [129].

6.1.1 Suppression of Ambient Light

The three main light sources in the OR are the fluorescent tubes, surgical lamps and the surgical microscope (Figure 17). The modulation is done by triggering and synchronizing the laser pulses with the rising edge of the spectrometer scan signal; the excitation light pulse width and the spectrometer scanning intervals (integration time) are thus equal (Figure 18). The system is controlled through a LabVIEW® (Version 8, National Instruments, Inc, Austin, TX, USA) program and is able to deliver pulses with a width in the range of 6-6500 ms. At least 2 mJ excitation energy is needed to get a strong enough fluorescence signal. This amount is set by the laser power and pulse width. The pulses are delivered with a duty cycle of 50% making equal light and dark pulses. The dark spectrum is the signal from the surrounding light and the light spectrum is the sum of the surrounding light and tissue fluorescence. The subtraction of the dark spectrum from the light spectrum results in a fluorescence signal free of background light disturbance; here referred to as compensated spectrum (Figure 18).

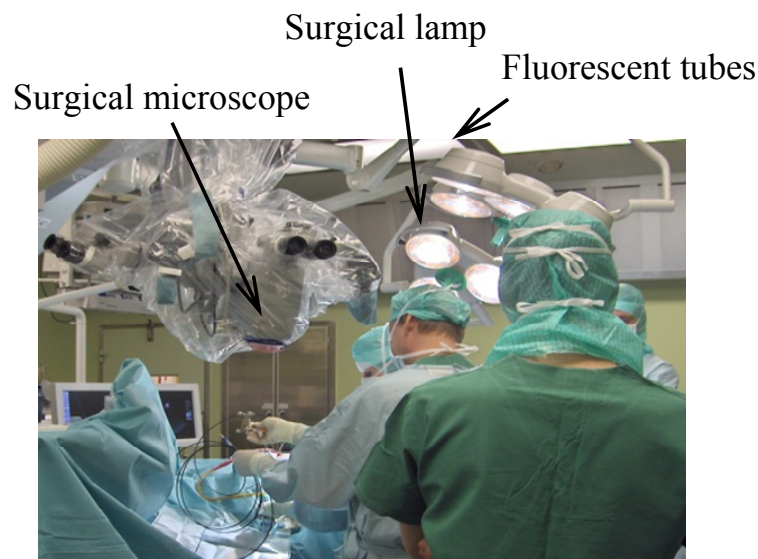


Figure 17 The three main light sources in the operating room: fluorescent tubes, surgical lamp and the surgical microscope (Neurosurgical OR, Linköping University Hospital).

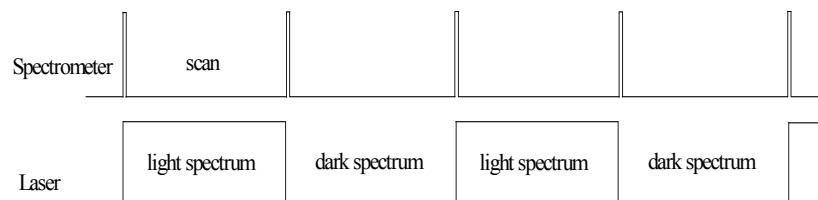


Figure 18 Modulation's concept for suppression of the surrounding light. The laser pulses start with the rising edge of the spectrometer scan signal.

Examples of light and dark spectra collected on skin under the different light sources in the operating room, and the subtraction of dark from light spectrum are shown in Figure 19. Fluorescence tubes impose a relatively weak background light which can be totally suppressed by the system. The surgical lamps and the surgical microscope, however, have higher light power which cannot be totally suppressed when the measurement is made during the direct exposure. The reason is the micro-second differences in the light and dark spectra (Figure 18) due to the spectrometer read-in routines. Therefore, during the measurements in the OR the microscope light should be either directed away, or the measurement site should be shaded by hand.

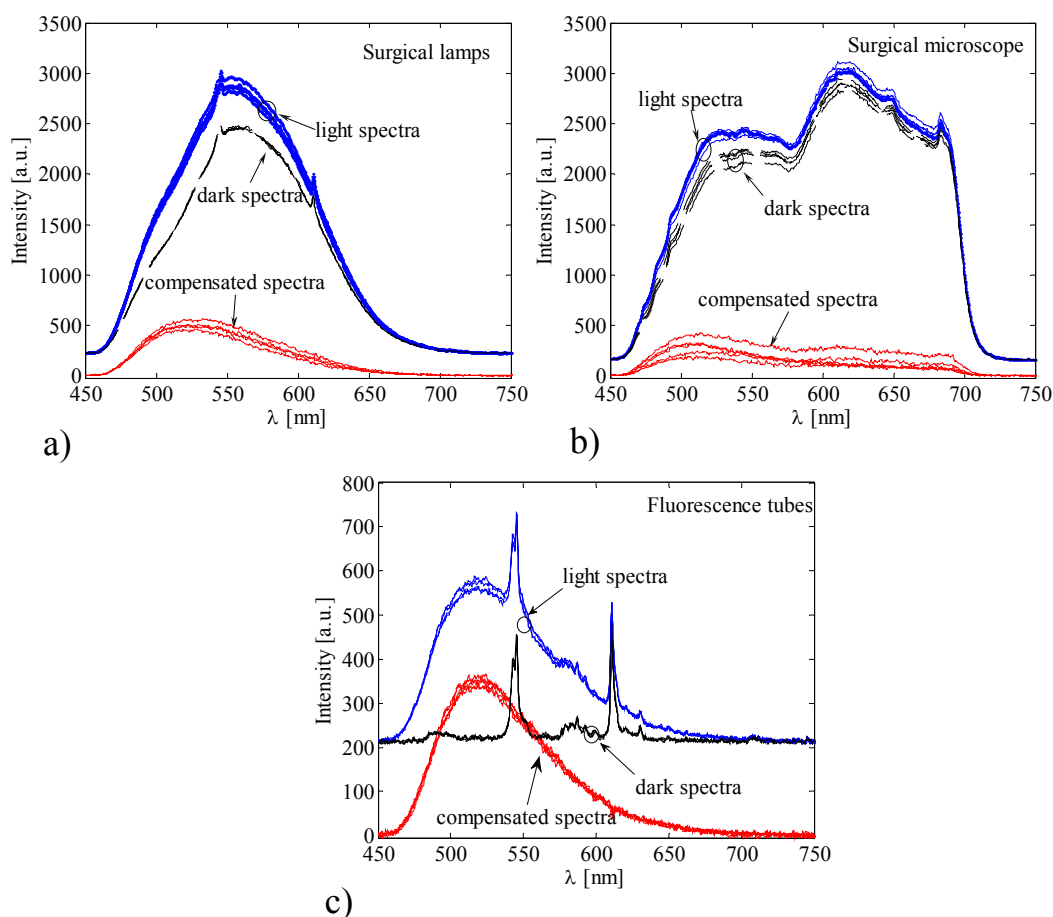


Figure 19 Suppression of the main background lights in the OR: a) fluorescent tubes, b) surgical lamps and c) surgical microscope. Copyright (2010) by John Wiley and Sons. Reprinted with permission from [129].

6.1.2 Optical Probes

A hand-held fiber optical probe transmitted the light between the tissue and the system. Several similar probes were used throughout the project time-span. In all of the probes the excitation light was brought to the measurement site by one single fiber ($\varnothing_{\text{core}} = 600 \mu\text{m}$, $\text{NA} = 0.37$). Different numbers of collection fibers ($\varnothing_{\text{core}} = 200 \mu\text{m}$, $\text{NA} = 0.22$) were

used in different probes (Figure 20). The probe shafts had a length of 12 cm and diameters of 2 or 3 mm with a more than 4 m long cable suitable for the operating room.

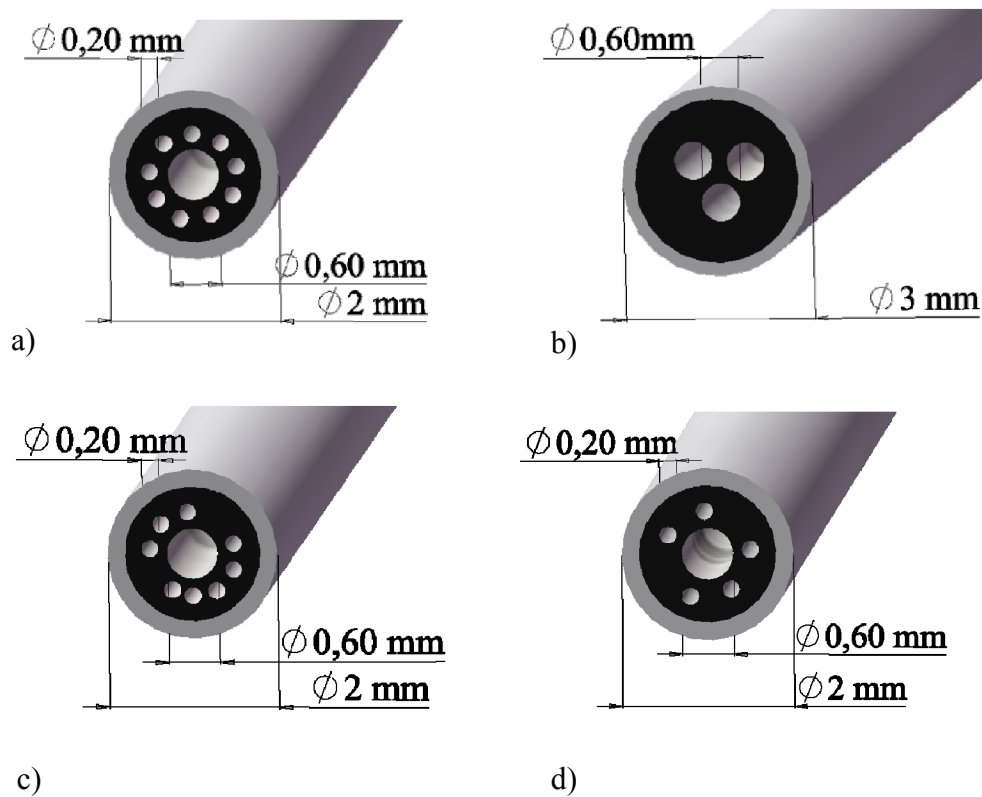


Figure 20 Probe configurations used during the study. a) probe 1, b) probe 2, c) probe 3 and d) probe 4.

6.2 Optical Specifications

Optical parameters related to excitation, probe geometry and position influence the signal collection. Optical parameters of excitation light are important regarding the laser safety and the amount of fluorophores that are excited in the tissue. The probe geometry, in addition to distance and angle of the probe relative to the tissue, affect the irradiance of the light that reaches the tissue and in the same manner the light that is collected from the tissue. Therefore, these parameters were investigated and are included in this section.

6.2.1 Laser Safety

The applied laser has class 3B which is dangerous for the eye upon direct or indirect exposure [130]. Since damage to the tissue occurs mainly through heat transfer, the temperature increase caused by the laser was investigated to consider damage to the skin and brain. Experimentally, using the IR thermometer (CIR8855, Injektor solutions, Stockholm, Sweden), the 10 mW laser light ($d = 2 \text{ mm}$ from surface) causes 1°C

temperature increase on the back of the finger after 1.5 minutes which is far longer than the actual measurement time using the optical touch pointer. Proteins in the cells go through an irreversible change first above 45°C when the temperature is increased within a few seconds [131]. Therefore, the effect of laser on the skin and the brain was considered negligible. Radiation of 10 mW blue laser did not cause any type of recognizable irritation when the skin was not treated with ALA. The same laser power caused irritation on the ALA treated skin after a few seconds.

6.2.2 Optical Parameters for Excitation

By having the numerical aperture (NA) of the optical fiber and the refractive index of tissue, n , the angle of light incidence, θ , can be calculated from Eq. 13. Irradiance, I , or power density which is the laser light power, P , per exposed surface area, SA (Eq. 14), is then calculated according to Eq. 15 for the specific optical fiber used (Figure 20, Figure 21).

$$\theta = \arcsin \frac{NA}{n} \quad (\text{Eq. 13})$$

$$SA = \pi (0.3 + h \tan \theta)^2 \quad (\text{Eq. 14})$$

$$I = \frac{P}{\pi (0.3 + h \tan \theta)^2} \quad (\text{Eq. 15})$$

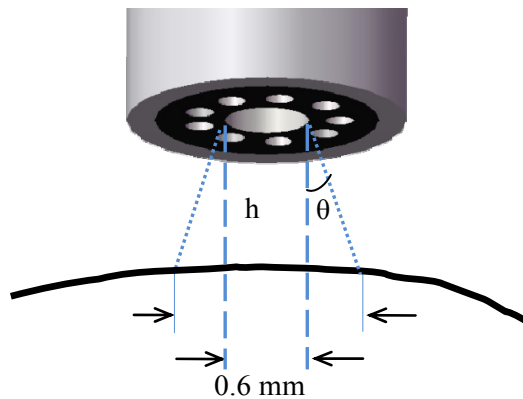


Figure 21 Corresponding geometry for calculation of the exposed surface area.

If the probe directly faces the tissue, the exposed surface area will be 0.28 mm^2 ($28 \times 10^{-4} \text{ cm}^2$) and when held at a distance from the tissue in the air ($n = 1$, $\theta = 21.7 \text{ deg}$) the exposed surface area will be a function of the distance (Eq. 14). At 1 mm distance the exposed surface area will be 1.5 mm^2 ($150 \times 10^{-4} \text{ cm}^2$). Using the estimated exposed surface area when the probe is in contact with the tissue, the standard optical parameters [132] were calculated as summarized in Table 6.

Table 6 Parameters used for the excitation of fluorescence in the brain

Parameters	Unit	OTP value
Duration of each treatment	s	0.4
Output power	mW	10
Frequency	Hz	2.5
Exposed area	cm^2	28×10^{-4}
Irradiance/Power density	W/cm^2	3.5
Dose/Energy density/Fluence	J/cm^2	1.4
Cumulative dose for each site	J/cm^2	4.2 (3×)

Effect of Angle and Distance Relative to the Tissue

Maximum transmission of light occurs when the probe is vertical and in contact with the tissue (irradiance = $3.5 \text{ W}/\text{cm}^2$). At other orientations the light transmission is presumed to drop according to Eq. 16 (Figure 22-a). Distance from the tissue reduces the excitation fluence (Figure 22-b). Probe pressure on the skin is reported to change the fluorescence intensity to 10% [133]. Experimentally, the maximum fluorescence was collected on the tissue and 0.5 mm above it. Greater distance reduced the collected fluorescence intensity. Pressing the probe on the tissue increased the fluorescence intensity up to 30% of its value when it was in a relaxed position on the skin.

Using Snell's law and by having the refractive indices of medium one and two as n_1 and n_2 , the fraction of the transmitted light, T, and the fraction of the reflected light, R, is given by:

$$R = 1 - T = \left(\frac{n_1 \cos\theta_1 - n_2 \cos\theta_2}{n_1 \cos\theta_1 + n_2 \cos\theta_2} \right)^2 \quad (\text{Eq. 16})$$

where θ_1 is the angle of incidence light with the surface normal in the first medium and $\theta_2 = \arcsin(n_2^{-1} n_1 \sin \theta_1)$ [48, 50].

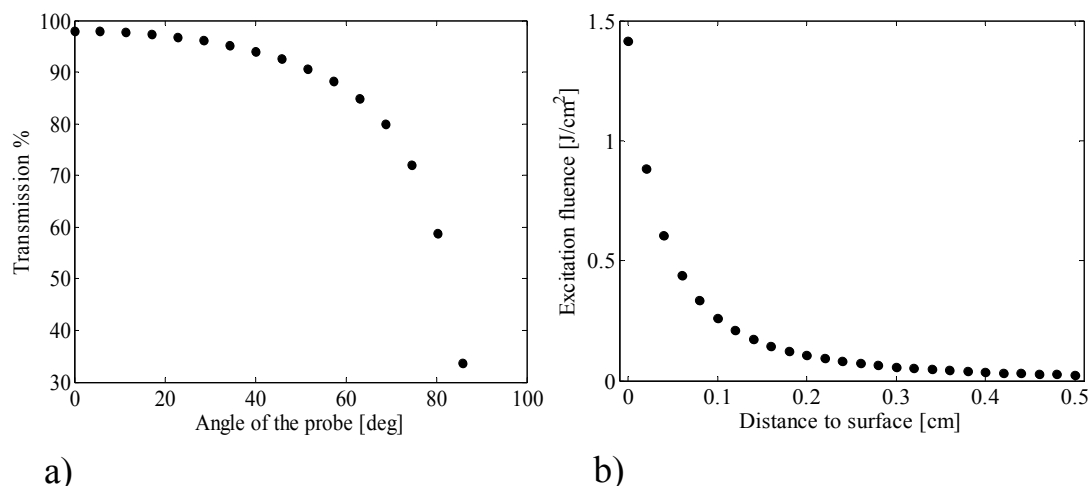


Figure 22 a) Percentage of the transmitted light from air to the tissue (skin) as a function of the probe angle with the surface normal and b) Irradiance as a function of probe distance from the tissue.

Effect of Fiber Separation

Experiments were performed on skin to investigate the effect of excitation and collection fiber separation on the collected fluorescence spectra. Using an array probe (Figure 23) with fibers ($\varnothing_{\text{core}} = 200 \mu\text{m}$, $\varnothing_{\text{cladding}} = 230 \mu\text{m}$) closely arranged in a row, the effect of fluorescence change as a result of fiber distances (230 μm , 460 μm , 690 μm) was studied on the skin. The first fiber was used as the source fiber with an output power of 10 μW . The second to the fourth fibers were one at a time used as the detection fiber. The distance from the source fiber affected the intensity of fluorescence but no line shape alteration was observed (Figure 24-a). In between the measurements; i.e., when the contacts were decoupled slight changes in the line shape of the spectra was sometimes observed. A high integration time 10 s was used to allow collection of a strong fluorescence signal. The excitation signal is however weak and results in a distorted spectral shape compared to the spectra collected at higher excitation powers.

Figure 24-b shows the spectra collected by the probes with configurations illustrated in Figure 20. The spectra in this figure are adjusted to show the same level of intensity for line shape comparison. The spectral difference is considered negligible.

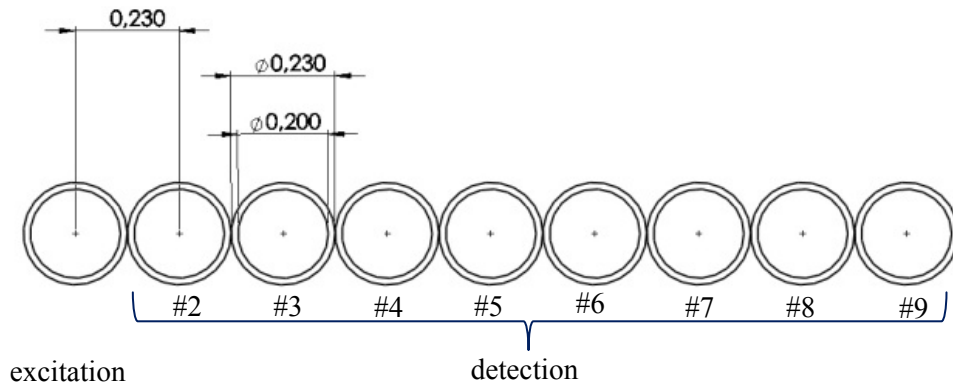


Figure 23 Array probe consisted of tightly arranged fibers. The first fiber from the left was used as source and the other fibers were one at a time used as detection fibers.

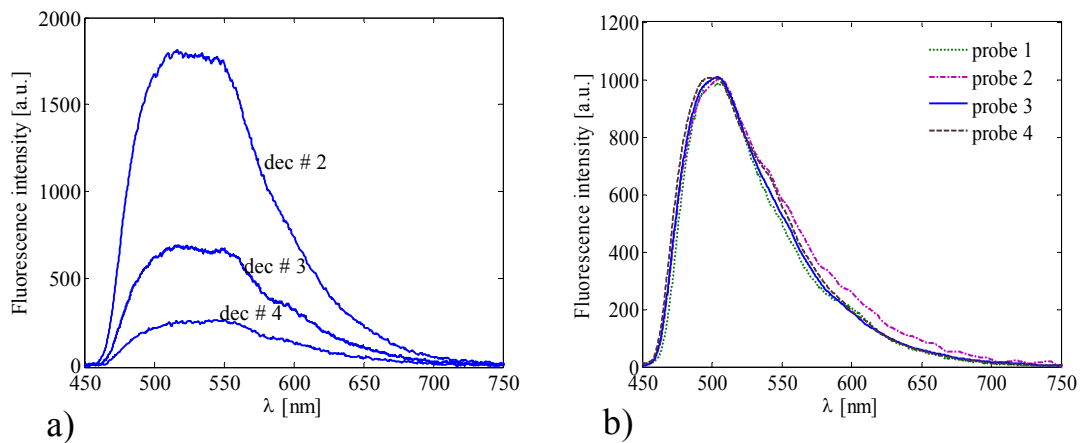


Figure 24 a) Effect of collection and source fiber separation on the fluorescence intensity and line shape collected on skin and b) Spectra collected by different probes showing negligible line shape difference. Intensity is adjusted in the latter case.

6.2.3 Excitation Depth

The tissue volume in which fluorophores were excited was approximated as the volume in which the excitation light is distributed. Axial and lateral distribution of excitation light at 405 nm was modeled in gray, white, low grade and high grade glioma based on the optical properties summarized in Table 1. Monte Carlo simulations were based on the multilayer MCML (Monte Carlo for Multi-Layered media) program [134] based on the program from the Lund University [135]. A fiber radius of 0.3 mm, excitation energy of 4 mJ and 10^6 photons were used for the simulations (Figure 25).

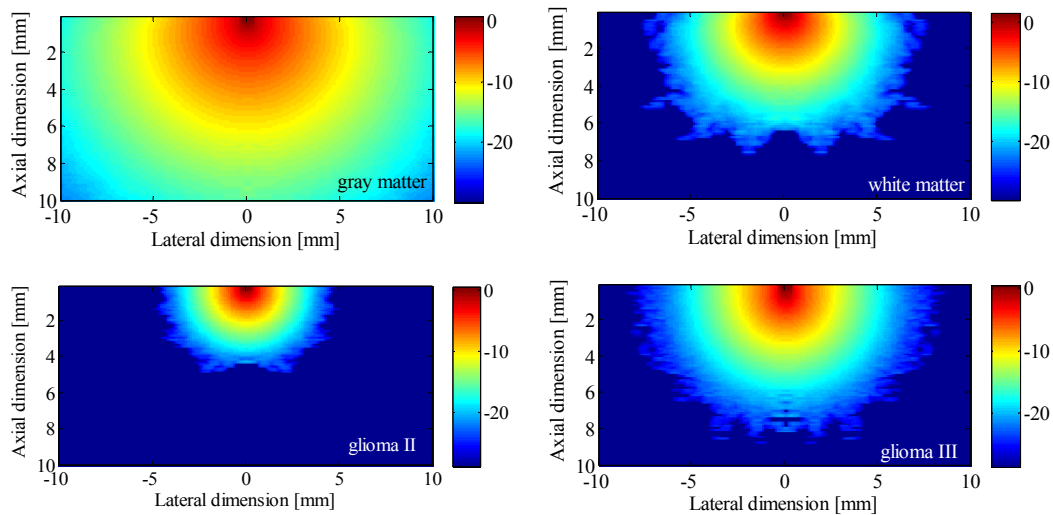


Figure 25 Distribution of the excitation light in different brain tissue types.

The Monte Carlo simulations in Figure 25 show the distribution of photons in the tissue; however, the actual excitation occurs in a smaller volume. To have an estimate for the actual volume, penetration depth of the excitation photons may be approximated according to Eq. 9 by applying the optical properties of the brain listed in Table 1. The excitation depth in brain and brain tumor tissue is listed in Table 7.

Table 7 Estimated excitation depth in various brain and tumor tissue types

	Gray matter	White matter	Glioma III	Glioma II	Meningioma
Excitation depth [mm]	0.06	0.02	0.11	0.04	0.09

6.3 Combination with Ultrasound-based Neuronavigation

As an alternative method for comparison, and to register the site of measurement, an ultrasound-based neuronavigation system (Sonowand AS, Trondheim, Norway) was used in combination with OTP [40]. After the skull was opened, images were taken from the tumor by the surgeon using an ultrasound transducer (Figure 26-a) connected to the positioning frame. The positioning frame has several reflecting spheres that allow the navigation camera to position the probe [136]. The probe was easily calibrated into the neuronavigation system by holding it at a fixed point (Figure 26-b). During the surgery, at the point of interest, one fluorescence measurement was performed with OTP followed by a navigation snapshot. Figure 26 shows the combination of OTP with the navigation system during the surgical procedure. For a 5 MHz transducer the radial, lateral and depth imaging resolutions are 0.5, 1 and 2 mm. Examples of ultrasound images and the registered fluorescence measurement site from the brain tumor are shown in Figure 27.

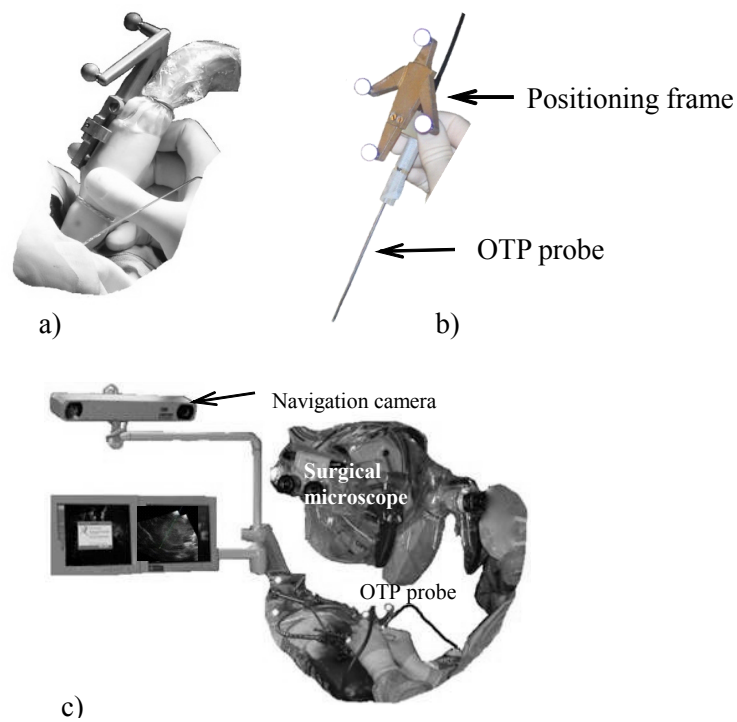


Figure 26 a) Imaging with the US transducer and calibration of the system; Copyright (2011) by John Wiley and Sons. Reprinted with permission from [137]. b) The OTP probe was calibrated into the navigation system and c) Combination of OTP with the navigation system and the surgical microscope (Neurosurgical OR, Linköping University Hospital).

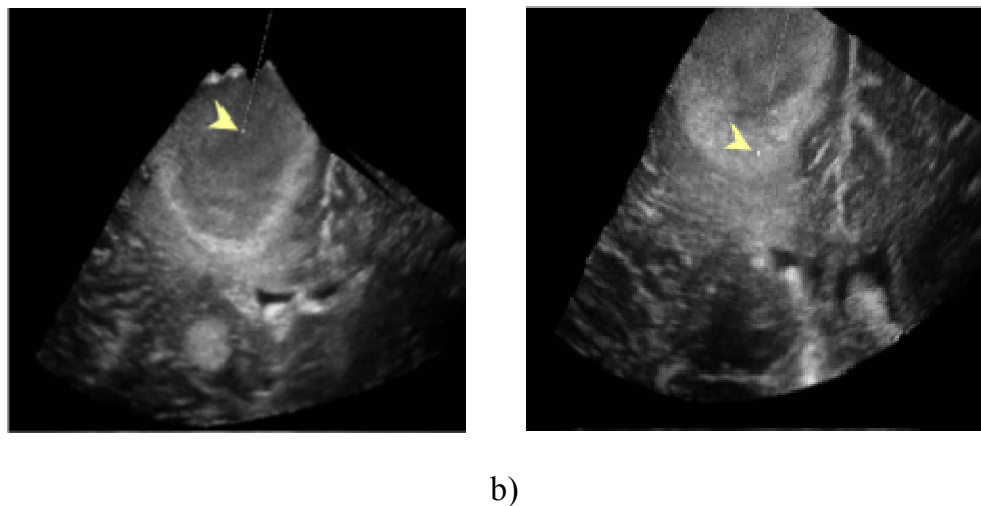


Figure 27 Examples of ultrasound images and the registered OTP measurement point on the image in a) necrosis and b) solid tumor. Copyright (2011) by John Wiley and Sons. Reprinted with permission from [137].

Chapter 7

Signal Quantification

To associate the amount of PpIX fluorescence to the malignancy degree of the tumor, the fluorescence signals were quantified by defining a fluorescence ratio. Interference of blood as one major challenge for signal quantification was investigated and a compensation method was developed. The procedure for the intra-operative brain tumor measurements is explained in Chapter 9.

7.1 Measurements on the Skin

In the laboratory, skin was used as a model for the brain measurements. The skin autofluorescence has a line shape similar to the brain autofluorescence (Figure 28). PpIX was induced in the skin by topically administrating Metylaminolevulinat (METVIX® 160 mg/g, Photocure ASA, Norway) cream. Metvix which is methyl-ALA is an esterified variant of ALA. The cream was applied in a 2-3 mm thick layer on an area of 3 cm² on the tape-stripped skin [93, 126] of the forearm 2-5 hours prior to the measurements. The skin was then covered with a transparent and non-absorbent dressing (Tegaderm™, 3M Health Care, Germany) and a non-transparent plaster to avoid photobleaching of the produced PpIX. Measurements were performed on well separated points on the treated site.

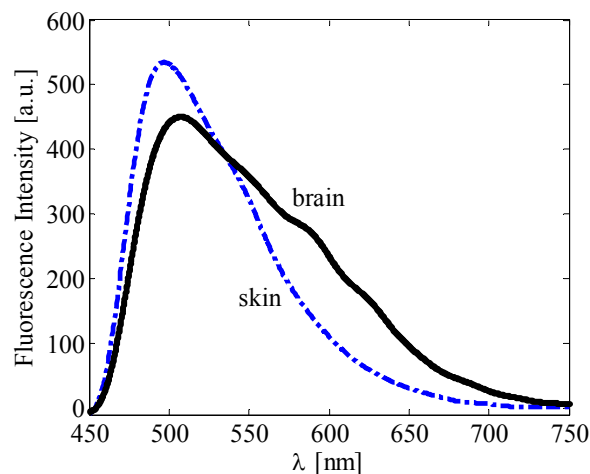


Figure 28 Autofluorescence spectra of the skin and the brain tissue.

7.2 Filtering and Calibration

The collected signals were often noisy, which induced some uncertainty when calculating values of the autofluorescence signal. The noise of the signal was removed using a low-pass filter. Fluorescence was measured at different power settings (1-10 mW) on the skin (Figure 29-a) to investigate the change of fluorescence intensity as a function of excitation energy. Fluorescence intensity ($I_{\lambda_{exc}}$) increased linearly with the increased excitation energy $I(\lambda_{exc})$; therefore, the proportionality of fluorescence intensity with laser power was calculated using a linear fit (Eq. 17).

$$I_{\lambda_{em}} = a_{\lambda} I_{\lambda_{exc}} + b_{\lambda} \quad (\text{Eq. 17})$$

where a_{λ} and b_{λ} are coefficients obtained by implementing linear fitting on fluorescence spectra corresponding to different excitation energies/irradiances. Figure 30 shows the coefficients for the whole spectral wavelengths in the skin and the brain. b_{λ} is related to the optical filter in the setup; however, its presence in the model is necessary. Figure 29-b, shows the fluorescence spectra excited by low energies. Line-shape of the fluorescence changes for the laser power of 1 mW using the applied optical fiber; however, they follow the linear fitting model.

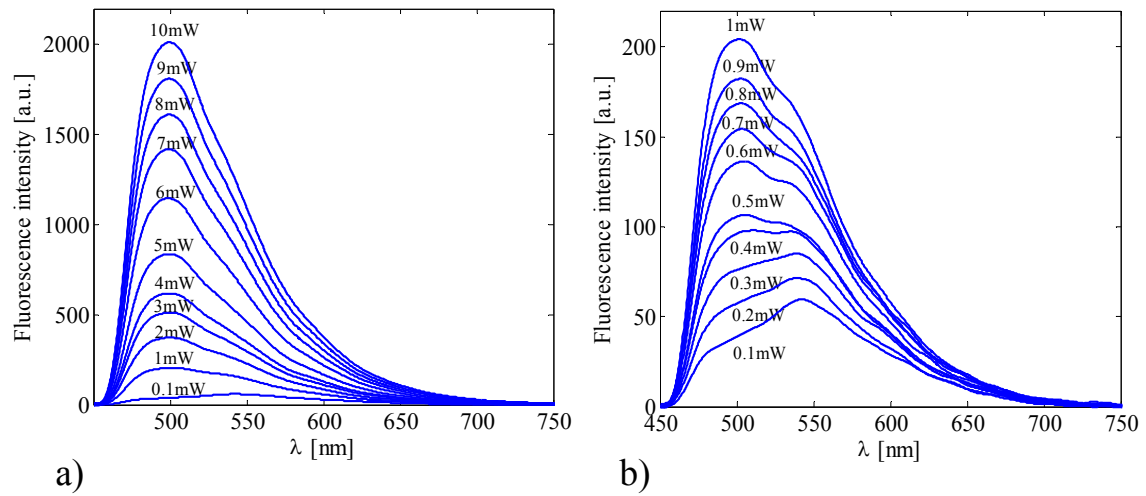


Figure 29 Fluorescence line shape as a function of excitation light (a) for laser power of 1-10 mW and b) for laser power of 0.1-1 mW.

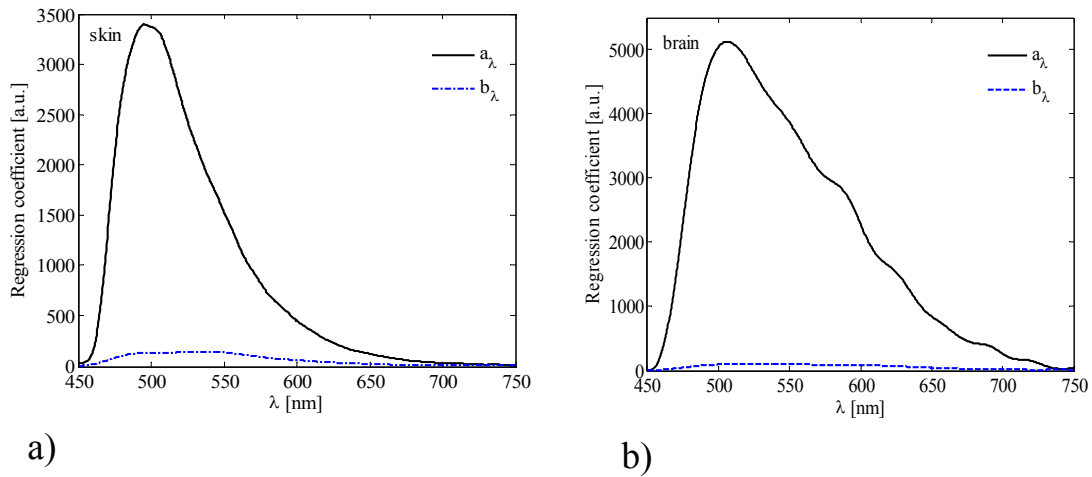


Figure 30 Coefficients obtained from linear fitting as a function of wavelength (a) in the skin and (b) in the brain.

7.3 Fluorescence Ratio

To normalize the PpIX fluorescence intensity, autofluorescence was used as a reference. Normalization was carried out since the angle and distance of the probe relative to the tissue within one set of measurements, in addition to a variation of probe geometries, laser power and pulse width settings used among sets of measurements made the excitation light delivered be different. The fluorescence ratio (FR) was defined as in Eq. 18 to quantify the PpIX fluorescence.

$$\text{FR} = \frac{I_{635} - I_{\text{autofl}(635)}}{I_{\text{autofl}(510)}} \quad (\text{Eq. 18})$$

where I_{635} is the PpIX fluorescence peak at 635 nm, $I_{\text{autofl}(510)}$ is the maximum intensity of the recorded signal, $I_{\text{autofl}(635)}$ is the autofluorescence at 635 nm (Figure 31). $I_{\text{autofl}(635)}$ can be obtained by interpolating the value at 635 using neighboring fluorescence values at 610 and 730 nm which are the two closest opposite ends where PpIX fluorescence is not influential.

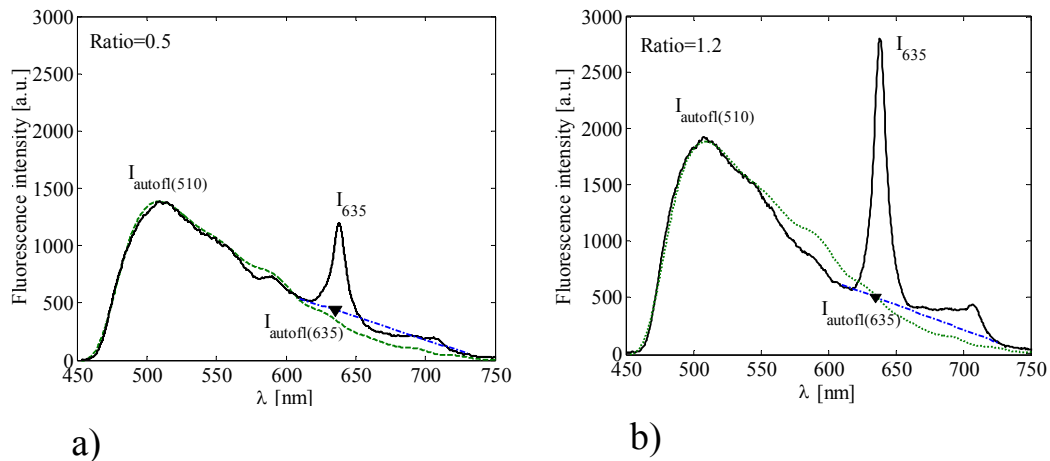


Figure 31 Examples of fluorescence ratio measured on the brain tumor and the estimated $I_{\text{autofl}}(635)$. The dotted line (green) shows the modeled autofluorescence obtained from Eq. 17 and the dash-dotted line (blue) shows the interpolated line between data points at 610 nm and 730 nm.

7.4 Blood Interference

During the operation the probe and the measurement site were constantly rinsed with sterile saline. Moreover, the probe tip was kept in a saline solution in between the measurements to avoid the adhesion and drying of blood cells on the probe. However, the problem was still present since even small remnants of the blood distort the collected signals and fluorescence ratio as a result. To avoid the repetition of measurements during surgery, the effect of blood interference was modeled and a compensation method was proposed.

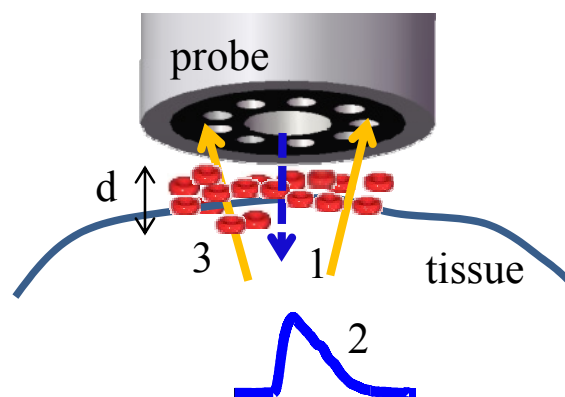


Figure 32 Sketch of model concept and steps: (1) attenuation of the excitation light, (2) fluorescence emission and (3) attenuation of the fluorescence.

The model is valid for any type of fluorescence and is based on the assumption that the blood is an absorption dominant medium ($\mu_a \gg \mu_s$). For this condition, Beer-Lambert law was used to model the light propagation in the medium. Hemoglobin is the dominant chromophore in blood and therefore its absorption properties are representative for absorption of the whole blood. The extinction coefficient of oxy and deoxy-hemoglobin (HbO_2 and Hb) measured by Prahl and Zijlstra et al., [60, 138] were used for comparison; however, as the data from Zijlstra are not available for the whole required wavelength range, the data from Prahl were further used. The absorption coefficient, μ_a , of hemoglobin was calculated by multiplying the extinction coefficient by 0.0054, as instructed [60].

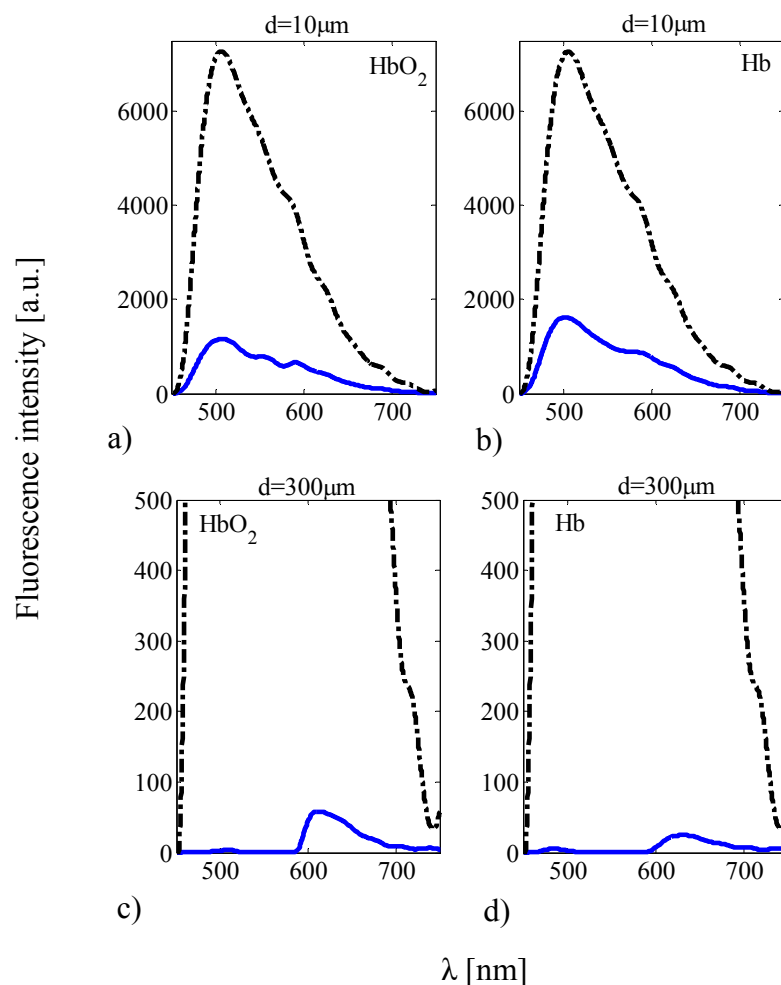


Figure 33 Pattern of blood interference in brain tissue for blood layer thicknesses of a,b) $10\ \mu\text{m}$ and c,d) $300\ \mu\text{m}$ for disturbance from pure hemoglobin and oxy-hemoglobin. The dashed signal is the undisturbed fluorescence and the signal with a solid line is the modeled blood-disturbed signal.

Blood interference model

The developed model considered the three following main steps: the attenuation of the excitation laser light when passing through blood from the probe to the tissue, the resulting fluorescence emission at the tissue and the attenuation of the tissue fluorescence when passing through the blood (Figure 32). The model for the distorted fluorescence signal, $I(\lambda, d)$, is formulated in Eq. 19. a_λ is obtained from calibration measurements on intact cortex. $I_{\lambda_{exc}}$ is the fluence of excitation light, μ_a is the absorption coefficient of hemoglobin and d is the average blood layer thickness in front of the probe.

$$I(\lambda, d) = (a_\lambda I_{\lambda_{exc}} e^{-\mu_a(\lambda_{exc})d} + b_\lambda) e^{-\mu_a(\lambda)d} \quad (\text{Eq. 19})$$

As an input, the fluence of the excitation fluence, $I(\lambda_{exc}, d)$, for each measurement was added to the model. However, $I(\lambda_{exc}, d)$ was variant and unknown during the surgery as the probe was not fixed and was therefore held at different positions relative to the tissue. An estimation of the excitation fluence was therefore used for the measurements on brain tumor (Paper V). Figure 33 illustrates the model applied to a non-disturbed fluorescence spectrum collected from an intact part of the cortex.

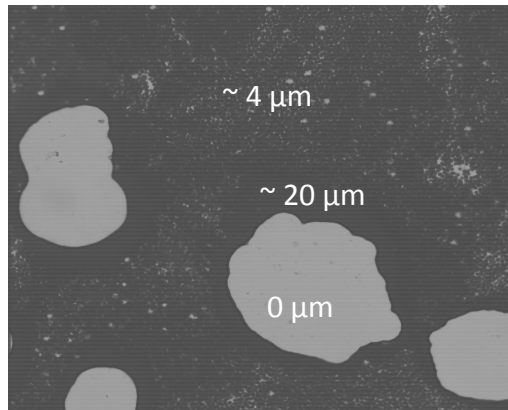


Figure 34. The blood layer thickness measured by confocal microscopy on an area of $650 \mu\text{m} \times 650 \mu\text{m}$. Using Eq. 19 a blood layer thickness of $5.5 \mu\text{m}$ was calculated.

Evaluation using confocal microscopy

Thickness of fresh blood spread on a fluorescent objective slide (Chroma, VT, USA) and covered with a transparent cover slip (Chance Propper Ltd., Warley, UK) was measured with confocal microscopy (Zeiss, LSM 700). The microscope was used without any fluorescence filtration (T-PMT). The fluorescence of the slide provided the background fluorescence for spectroscopy measurements which were performed in conjunction with microscopy measurements. An example of the image taken with confocal microscopy with a surface area of $650 \mu\text{m} \times 650 \mu\text{m}$ is shown in Figure 34. The estimated blood layer thickness was $5.5 \mu\text{m}$ as estimated by OTP using the theoretical model. The blood layer had different thicknesses on various spots on the measurement

site, thus the total thickness is presumed to be an average of the layer over the measurement area.

Correction of fluorescence ratio in the clinical measurements

Blood distortion induced an overestimation in the fluorescence ratio calculated. This was compensated by defining a *correction factor* (CF) obtained from the blood interference model. The correction factor was calculated as in Eq 20:

$$CF = \frac{I(\lambda_{635}, 0)/I(\lambda_{510}, 0)}{I(\lambda_{635}, d)/I(\lambda_{510}, d)} \quad (\text{Eq. 20})$$

where $I(\lambda_{635}, 0)$, $I(\lambda_{510}, 0)$, $I(\lambda_{635}, d)$ and $I(\lambda_{510}, d)$ are the fluorescence intensity values calculated from Eq. 19. The estimated blood layer thickness, d , was obtained by matching the model with the distorted signal. The corrected fluorescence ratio was then obtained by multiplying the correction factor by the fluorescence ratio of the measured signal.

The model was evaluated for fluorescence signals with PpIX ($n = 6$) and without PpIX contribution ($n = 14$). The correction factor may be calculated for both signal types; however, it is only meaningful for the PpIX-containing signals. The distortion models for two PpIX containing signals are shown in Figure 35. The model tended to have a higher agreement with the signal with a low contribution from PpIX. This deviation was associated with the autofluorescence decrement in the presence of relatively high amounts of PpIX relative to the considered PpIX-free autofluorescence in the model.

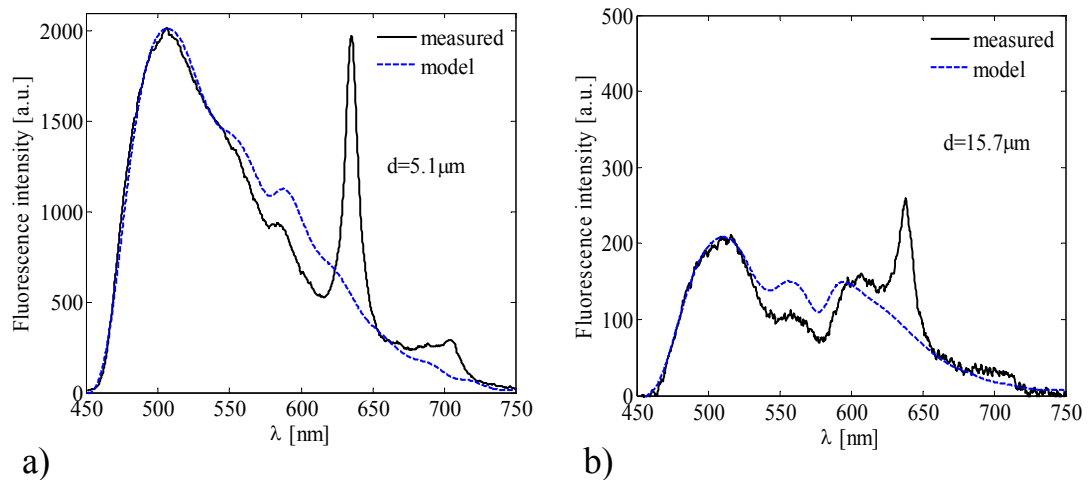


Figure 35 Examples of compensation for blood interference in the presence of PpIX a) With a correction factor of 0.92, the fluorescence ratio (0.76) can be corrected to 0.69. The blood layer thickness is 5.1 μm . b) With a correction factor of 0.60, the fluorescence ratio (0.75) is corrected to 0.45. The blood layer thickness is 15.7 μm .

Chapter 8

Photobleaching Dynamics

Dynamics of photobleaching is important regarding the decaying rate of fluorescence and the parameters that affect the photobleaching. For this thesis photobleaching behavior was studied on the skin and the brain tumor tissue in two series; once to adjust the system settings (Paper III) and once in continuation of the first study, to develop a dynamic model using principal component analysis (PCA) for additional investigation on the photobleaching behavior and to predict the induced photobleaching (Paper IV) before the start of a measurement. The procedure was approved by local ethics committee (No: M139-07 with complementary permission T83-09) and written informed consent was received from the volunteers.

Data were collected from the skin and the brain in both the CW and PL mode. The brain measurements were performed in vivo ($n = 9$) and ex vivo ($n = 22$) on fresh tumor samples. No statistical difference was observed between the in vivo and ex vivo brain measurements with the same excitation settings, thus the data are not presented separately. Figure 36 shows photobleaching over the whole fluorescence spectrum for a brain tumor sample.

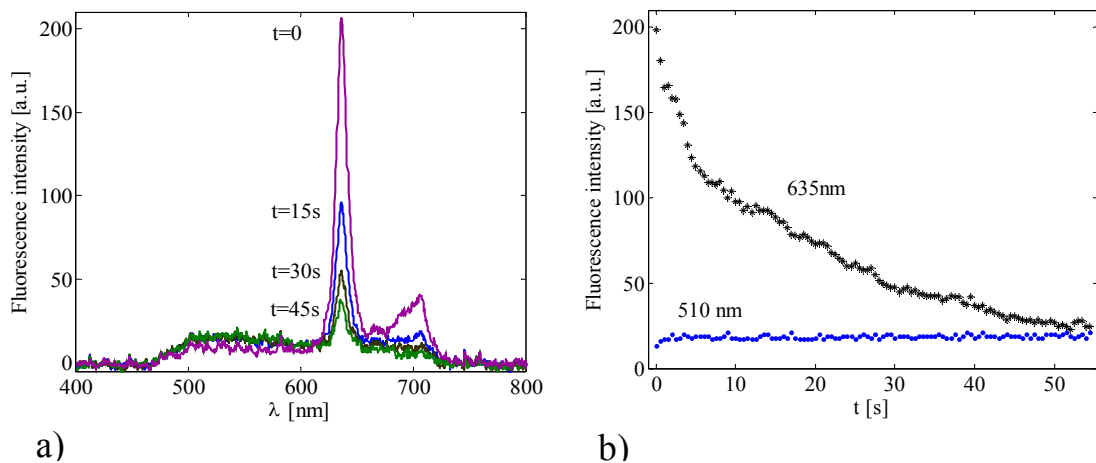


Figure 36 Photobleaching in brain tumor sample: a) Photobleaching shown in the whole fluorescence spectrum and b) Change of autofluorescence at 510 nm and PpIX peak at 635 nm versus time. Excitation was applied at 5 mW in continuous wave mode.

8.1 Dynamic Model of Photobleaching

A series of measurements was carried out on the forearm skin of four volunteers on non-treated ($n = 90$) and ALA treated ($n = 129$) skin sites. The measurements were

performed on an approximately 3 cm² area when ALA was applied, each at a new point about 3 mm² apart from the other measurement points. The measurement site was covered from light before the measurements and during the measurements. Only in between the measurements, were lights briefly turned on to shift the probe position. The probe was applied with the same amount of pressure throughout all the measurements. Measurements were performed with integration time (pulse width) of 0.2 s. A range of 50-200 spectra was collected on each measurement point.

Photobleaching series were analyzed by PCA to obtain the main contributing components to the fluorescence intensity. The number of main contributing components was obtained from eigenvalues with greatest value (Figure 37-a). The components were rotated to gain their maximum contribution (Figure 37-b). A total of three spectral components were sufficient to describe the sequences: autofluorescence, PpIX and blue shift. A dynamical model was developed based on the principal components and the fluorescence decay rates to calculate the initial amount of fluorescence. Using this model spectral composition of one instant was calculated from the previous instant. The same fluorescence ratio, but with the principal component values for PpIX and autofluorescence, was used to evaluate the amount of fluorescence.

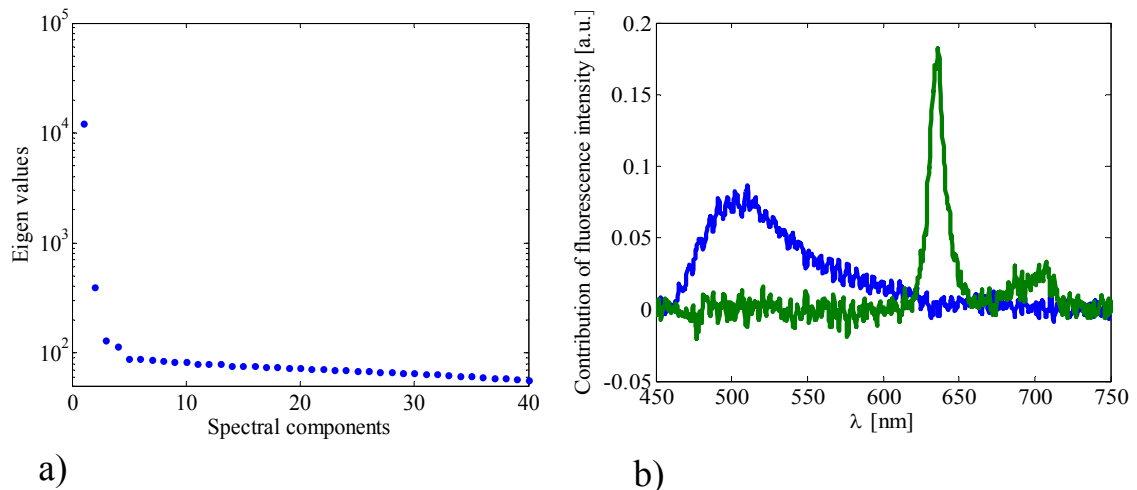


Figure 37 Principal component analysis of a skin fluorescence sequence. a) The eigenvalues of PCA, for this sequence there are two main contributors by which the signal may be described. b) The spectral shape of the first two components representing autofluorescence and PpIX fluorescence.

8.2 Parameters Influencing Photobleaching

Different time points that fluorescence reached a certain percentage (90%, 37% and 10%) of its initial value was calculated for a range of signals. The mean \pm standard deviation ($m \pm SD$) values are presented in Table 8. These values are all a measure of the photobleaching rate.

8.2.1 Effect of Photobleaching on Autofluorescence and Blue-Shift

When PpIX was present, autofluorescence increased in both the skin and brain while PpIX was photobleached (~4.2%). Autofluorescence did not increase on non-treated skin or after PpIX was photobleached. This phenomenon was mainly caused due to the change of absorption properties of the tissue in the presence and absence of PpIX. Kim et al report a < 2% increase in the absorption coefficient of their PpIX-containing phantom [116]. Blue shift was derived as one of the components of PCA analysis and was interpreted as the shift of autofluorescence peak value. Blue-shift, when present, increased as a result of photobleaching.

8.2.2 Effect of Excitation Power and Modulation on Photobleaching

The effect of excitation power was studied for powers 1-10 mW. At higher excitation powers photobleaching lifetimes were shorter (Table 8). After a certain power, photobleaching showed a saturated behavior suggesting that at high excitation powers did not significantly increase the photobleaching (Paper IV, Figure 8).

A faster photobleaching ($p < 0.05$) was observed in the brain when pulse widths of 0.5 s at 5 mW power were applied. Similarly, a faster photobleaching was seen in the skin when modulated excitation was applied (Table 8). This observation was associated with the diffusion of oxygen during the dark pulses. CW versus PL excitation did not appear to have influenced the blue shift.

Several pulse widths (0.2, 0.4, 0.5, 1 and 1.5 s) were applied to the skin with two power settings of 5 and 10 mW and duty cycles of 50% (Figure 28). At 5 mW, for pulses of 0.4 s wide a statistical difference from the CW excitation was observed ($p < 0.05$). At 10 mW, the statistical difference was only observed for 0.5 s pulse widths.

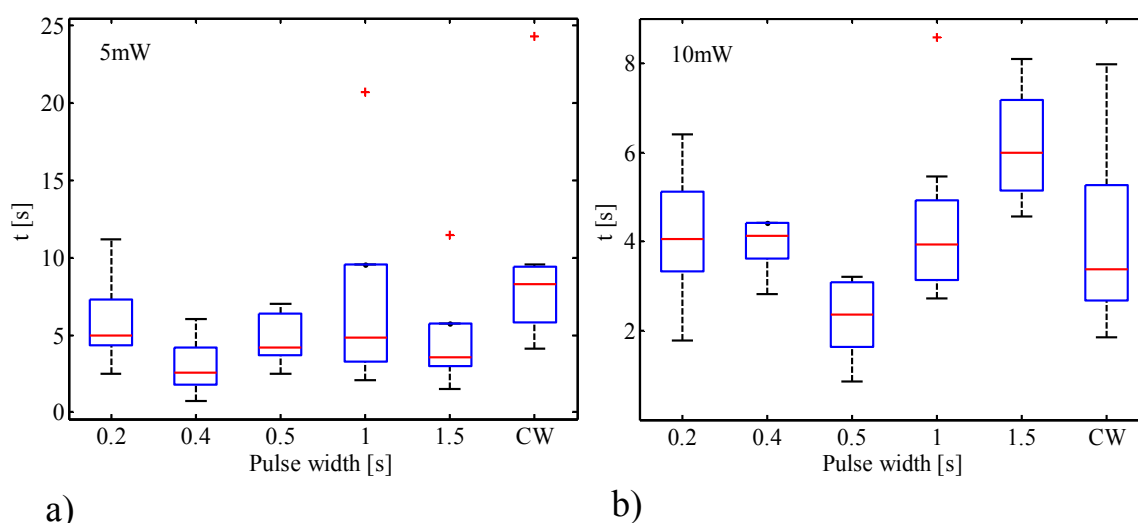


Figure 38 Median of the time that initial fluorescence reaches 37% of its initial value ($t_{37\%}$) as a function of different pulse widths for excitation powers of a) 5 mW and b) 10 mW. Copyright (2009) by SPIE. Reprinted with permission from [139].

Table 8 Photobleaching of PpIX in skin and brain in terms of the time fluorescence reaches 90%, 37% and 10% of its initial value. Copyright (2009) by SPIE. Reprinted with permission from [139].

PPIX PHOTBLEACHING IN SKIN				
Power	n	t (90%) m ± SD [s]	t (37%) m ± SD [s]	t (10%) m ± SD [s]
Continuous				
1 mW	7	0.3 ± 0.6	17.4 ± 11.7	48.5 ± 33.4
5 mW	11	0.3 ± 0.2	8.8 ± 5.4	42.6 ± 17.0
10 mW	8	0.2 ± 0.1	4.1 ± 2.0	19.8 ± 8.6
Pulsed				
1 mW	0			
5 mW	5	0.3 ± 0.3	4.8 ± 1.8	12.5 ± 3.5
10 mW	6	0.2 ± 0.1	2.3 ± 0.9	8.7 ± 2.9

PPIX PHOTBLEACHING IN BRAIN				
Power	n	t (90%) m ± SD [s]	t (37%) m ± SD [s]	t (10%) m ± SD [s]
Continuous				
1 MW	9	5.1 ± 7.6	36.5 ± 22.5	75.3 ± 31.3
5 MW	7	2.5 ± 2.2	42.2 ± 24.0	66.5 ± 16.8
10 MW	2	1.7 ± 0.0	26 ± 5.7	42.5 ± 3.5
Pulsed				
1 MW	1	1.6	7.4	50
5 MW	11	1.1 ± 1.1	20.2 ± 14.1	33.6 ± 14.7
10 MW	0			

Chapter 9

Clinical Evaluation

9.1 Clinical Procedure and Data Collection

Patients with suspected glioblastoma tumor were considered (n = 22); 12 males, 11 females, aged 47-78 years. A dose of 5 mg/kg bodyweight ALA was dissolved in orange juice and orally administered 2-3 hours prior to craniotomy. The procedure was approved by the local ethics committee (No: M139-07 with complementary permissions T110-08 and 2010/70-32) and written informed consent was received from the patients for the intra-operative measurements.

Of the twenty two patients five were excluded due to the absence of PpIX fluorescence in the tumor (Figure 39). One patient had an abscess and the remainder had tumors diagnosed to be of type recurrent GBM, recurrent glioma grade II, malignant astrocytoma and metastases. In two patients only photobleaching was studied and in one patient ALA was not administered to search for the presence of endogenous PpIX in tumor. Data from the remainder of the patients were further analyzed by comparing the fluorescence ratio to visual diagnosis, histopathology examination and ultrasound navigation.

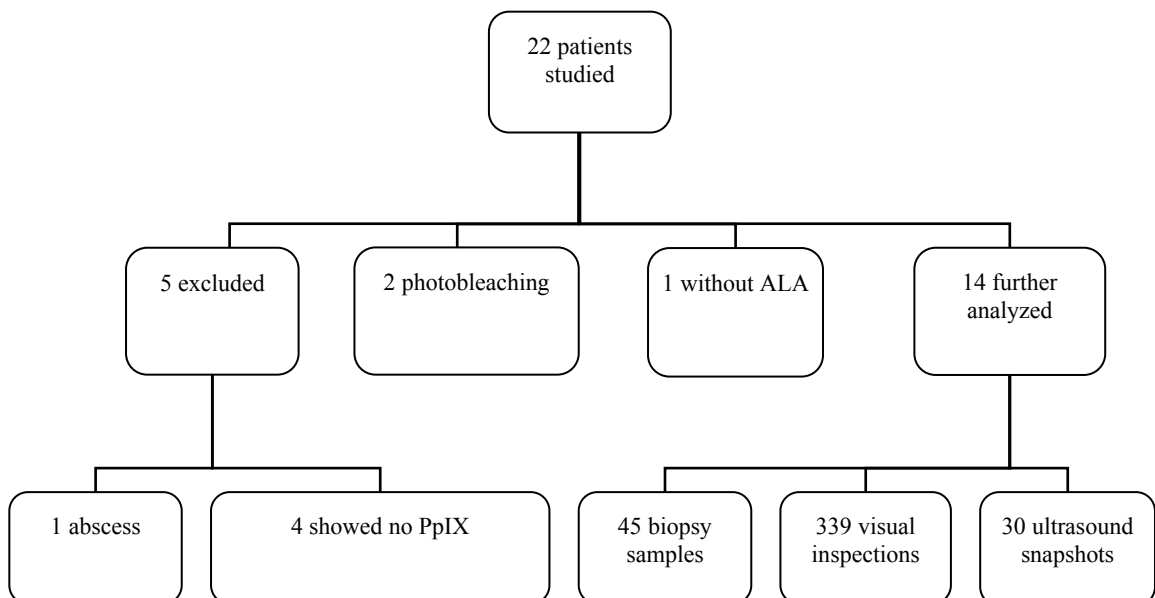


Figure 39 Patient data included in the thesis.

Measurements

All the measured points were intra-operatively categorized by the surgeon into healthy, tumor, necrosis, gliosis and tumor margin. Some points with no possible diagnosis were grouped as unclassified. The points which had no noted diagnosis and points with disturbed signals were excluded. In total 339 points were further analyzed. Forty five of these points were examined for histopathology. In total 30 snapshots were taken with the ultrasound navigation system, 19 of which had either a pathology diagnosis ($n = 8$) or a definite diagnosis by the surgeon ($n = 11$).

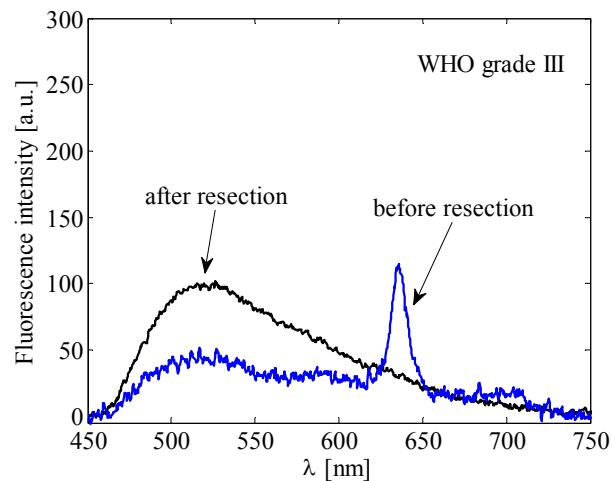


Figure 40 Fluorescence spectra on a site before and after resection. The biopsy showed a grade III malignancy. Copyright (2010) by John Wiley and Sons. Reprinted with permission from [129].

Histopathological examination

Approximately 1-2 mm large biopsies were taken in the operating room. The samples, either fresh or in formalin, were sent to the pathological department. In the pathological examination routine at the Department of Neurosurgery Linköping University Hospital, the samples were paraffin embedded and fixated. Using a microtome 4 micrometers sections were cut and put on objective slides. The samples were subsequently examined under the microscope determining the presence of necrosis, gliosis and tumor. malignancy was typed (i.e., astrocytoma, oligodendroglioma, glioblastoma) and graded according to WHO as grade II, grade III, grade IV [1]. If conclusive grading could not be made, the sample was classified as a high or low malignant tumor. Three neuropathologists were involved and each sample was analyzed by at least one of them.

9.2 Statistical Analysis and Clinical Performance Measures

The fluorescence ratio was calculated for all the collected spectra. The measurements with distortion from the operating room lamps or movement or blood were excluded from the statistical analysis. The data were statistically analyzed once based on the fluorescence ratio in Eq. 18 (quantified approach) and once based on the presence and

absence of PpIX peak (binominal approach). For the binominal data, Fisher's exact test with double-sided 95% confidence interval was used. The quantified data groups had a non-normal distribution; therefore, non-parametric statistical methods (Mann Whitney U-test) were applied.

In some surgeries, the measurement time was delayed which extended the time between ALA administration and measurements up to nine hours. No correlation between ALA administration time and maximum fluorescence intensity level was seen ($r = -0.03$, $p\text{-value} > 0.05$). The maximum fluorescence ratio is plotted vs. the time interval of ALA administration in Figure 41. PpIX could be detected between 2.5-9 hours after ALA administration. Longer and shorter intervals were not tested.

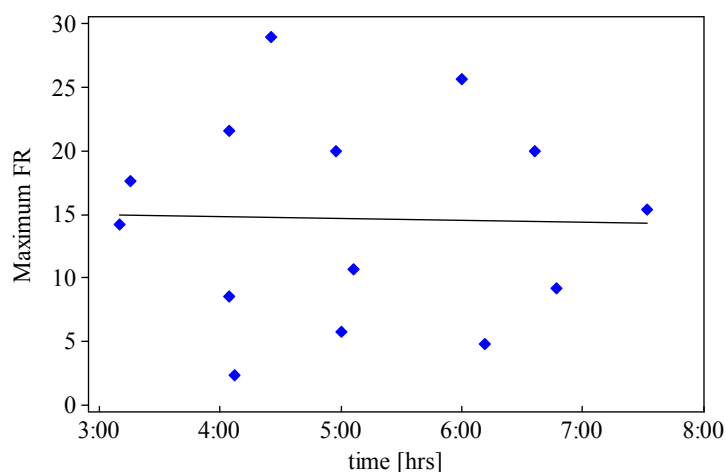


Figure 41 Fluorescence range of the collected data compared on the basis of ALA administration time. Each point corresponds to the maximum fluorescence ratio detected in one patient. The horizontal axis shows the measurement time of the maximum fluorescence ratio value.

9.2.1 Quantified Approach

The fluorescence ratio varied to a great amount among the patients which made the absolute value definition a difficult task. The intra and inter patient variation was also observed when the actual concentration of the PpIX was calculated [106]. To avoid calculating noise as PpIX, the ratios were set to zero when $(I_{635} - I_{\text{autofl}(635)}) > 20$. Figure 42 shows the box plots with 25% and 75% percentile of the fluorescence ratio categorized based on visual diagnosis. By performing the Mann-Whitney U-test, statistically significant difference was observed between non-tumor and tumor groups ($p < 0.001$). The median fluorescence ratio was lower in the margin (0.6) than the tumor (1.9). Median of fluorescence ratio was zero for gliosis and necrosis.

Figure 43 shows box plots with 25% and 75% percentile of the fluorescence ratio categorized based on the results from histopathological examination. Low grade malignancies (0.3) showed a lower fluorescence than high grade malignancies (2.4) ($p < 0.05$). Gliosis (1.6) and necrosis (1.0) showed a moderate fluorescence ratio.

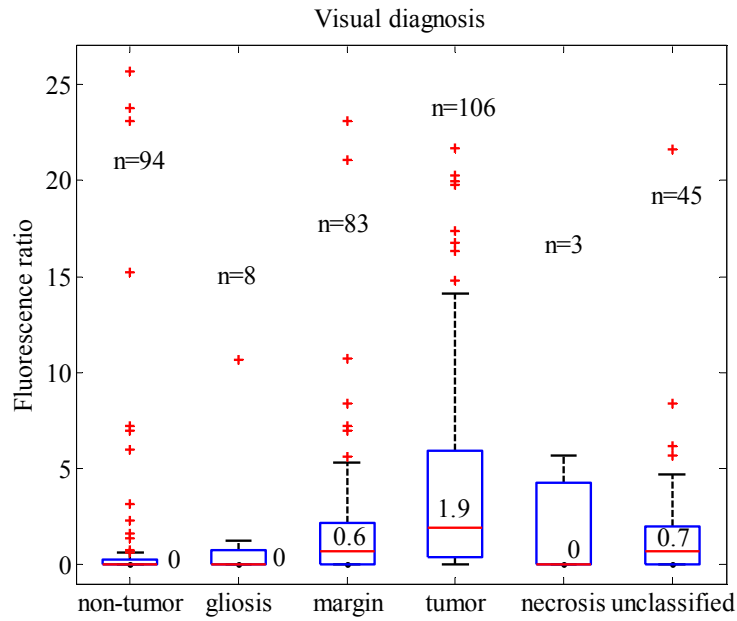


Figure 42 Comparison of fluorescence ratio with visual diagnosis of the surgeon. A total of 339 samples were included.

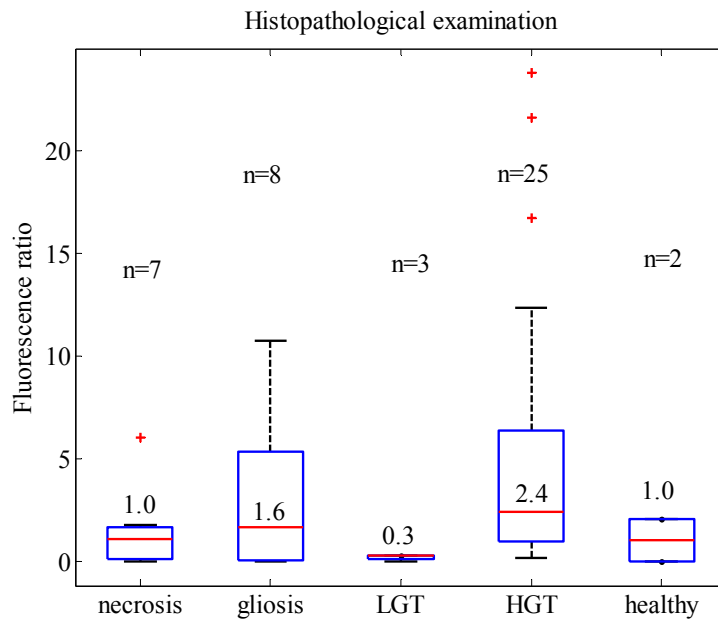


Figure 43 Comparison of fluorescence ratio with histopathological examination. The median values are stated. A total of 45 samples were included.

9.2.2 Binominal Approach

The binominal approach was based on the presence or absence of PpIX fluorescence. The limit was defined the same as the quantified approach; i.e., $(I_{635} - I_{\text{autofl}(635)}) > 20$ represented the presence of PpIX. Table 9 shows the fluorescence response of tumor tissue type based on visual diagnosis of the surgeon and Table 10 shows the fluorescence response of each histology-based tissue sample.

Table 9 Binominal coding of the fluorescence based on availability of the PpIX peak and visual diagnosis of the surgeon.

Visual diagnosis			
Tissue type	Fluorescence absent	Fluorescence present	Total
non-tumor	64	30	94
gliosis	5	3	8
margin	29	54	83
tumor	19	87	106
necrosis	2	1	3
unclassified	15	30	45

Table 10 Binominal coding of the fluorescence based on availability of the PpIX peak and histopathological examination results.

Histopathological examination			
Tissue type	Fluorescent absent	Fluorescent present	Total
necrosis	1	6	7
gliosis	2	6	8
LGT	1	2	3
HGT	0	25	25
healthy	1	1	2

To assess the diagnostic performance, parameters of sensitivity, specificity, positive predictive value (PPV), negative predictive value (NPV) and test efficiency were calculated [140]. The values corresponding to the OTP outcome are included in Table 11. Presence of PpIX in necrosis, low and high grade tumor is taken as true indication of malignancy and presence of PpIX in the gliosis and healthy tissue is taken as false indication of malignancy.

Table 11 Diagnostic performance of OTP. TP: true positives, TN: true negatives, FN: false negatives and FP: false positives.

	TP	TN	FN	FP	total
Count	33	3	2	7	45

Sensitivity	Specificity	PPV	NPV	Test efficiency
TP/(TP+FN)	TN/(TN+FP)	TP/(TP+FP)	TN/(TN+FN)	(TP+TN)/(TP+FP+TN+FN)
0.94	0.30	0.83	0.60	0.80

A total of 19 ultrasound snapshots were collected and compared to the fluorescence measurements and the histopathological results, or the definite diagnosis of the surgeon if the histopathological examination had not been performed. Values of zero and one were assigned to false and correct results obtained from US and OTP. For the combination of the methods a logical ‘or’ was used; therefore, if any of the methods showed a malignant tissue, the final result was considered as a malignant. As shown in Figure 44, when a combination of the OTP and US is used, the true positives (TP), false negatives (FN) and false positives (FP) improved in a favorable direction, but the true negatives (TN) dropped unfavorably.

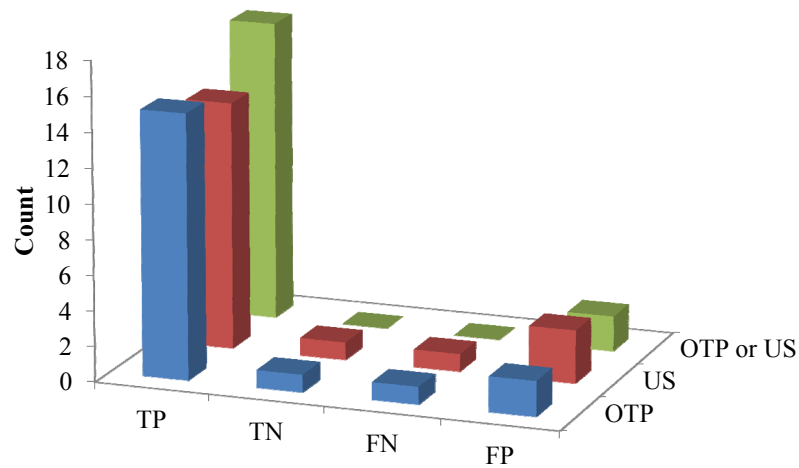


Figure 44 Diagnostic performance of OTP, ultrasound navigation (US) and their combination.

Chapter 10

Review of the Papers

Paper I- Optical touch pointer for fluorescence guided glioblastoma resection using 5-aminolevulinic acid

The paper described the system setup, concept and signal quantification used throughout the following publications and the thesis. A fiber-optical fluorescence spectroscopy system was set up for recording and quantifying the fluorescence signals. A minimum of 2 mJ (0.4 s and 5 mW) excitation energy was needed to collect an acceptable fluorescence signal from the brain; thus, the laser power and pulse width were in this study set to 5 mW and 0.4 s (Irradiance = 1.78 W/cm^2). The heat generated by these laser settings is negligible and thus no potential damage to the tissue is estimated.

The system is specifically developed for performance in the OR by reducing the surrounding light from the collected signals. To serve this purpose two spectra with the same pulse width are recorded at each measurement point, one with laser excitation (light spectrum) and one without (dark spectrum). By reducing the dark from the light spectrum, the fluorescence signal is extracted from the total fluorescence and surrounding light.

One purpose of the system is to record and quantify the fluorescence signals. The collected fluorescence is a sum of the tissue autofluorescence and the fluorescence of PpIX, in case it is present. Signal quantification is initially done by using a number referred to as the fluorescence ratio or ratio number. This number is obtained by dividing the pure effect of PpIX fluorescence by the maximum autofluorescence. Examples of fluorescence measurements in the healthy and malignant brain tissue and the corresponding fluorescence ratio are included in the paper.

Paper II- Fluorescence spectroscopy measurements in ultrasonic navigated resection of malignant brain tumors

In this paper, the performance of the fluorescence spectroscopy system and the quantification method was evaluated on nine patients undergoing tumor resection, practically and statistically. The quantified fluorescence signals (explained in Paper I) were compared based on the surgeon's visual diagnosis, histopathological examination and ultrasound-based navigation system. A total of 20 biopsy samples, 30 ultrasound images and 180 visual diagnosis points were included.

5-ALA (5 mg/kg body weight) dissolved in orange juice was orally administered 2-3 hours prior to craniotomy. The patients underwent the conventional surgical procedure. Standard white light microscopy and ultrasound navigation was used in addition to the OTP measurements. The OTP probe was set into the navigation system. The measurement points were visually diagnosed as healthy, gliosis, margin, necrosis and

tumor. At some points fluorescence measurement was performed directly after registration of the probe location on the ultrasound image and thereafter a biopsy sample was taken. Tissue type on the ultrasound image was categorized as tumor core and in/out margin and biopsy samples were classified as necrosis, gliosis and tumor.

Fluorescence data were coded in two ways of the presence and absence of PpIX (binominal approach) and actual calculated fluorescence ratios (quantified approach). The median values for the visually distinguished groups of tumor and healthy tissue showed a statistical difference using both the coding methods. Fluorescence was zero in necrosis, low in the margin and gliosis, and higher in the tumor. Using OTP, differentiation of necrosis, healthy and tumor tissue is possible; however, combined fluorescence and ultrasound-based navigation may improve the tumor diagnosis.

Paper III- Photobleaching behavior of protoporphyrin IX during 5-aminolevulinic acid marked glioblastoma detection

This paper aimed at one of the major challenges of fluorescence quantification, photobleaching. Photobleaching and its effect on autofluorescence and PpIX fluorescence peak were studied in the skin and brain tumor using the continuous and pulsed modulation of the OTP system versus several power and pulse width settings. The calculations were implemented in the system to reduce the photobleaching induced by the laser excitation light.

No photobleaching of the autofluorescence was observed in the absence of ALA in the tissue. However, when PpIX was present the autofluorescence increased approximately 5 % due to the photobleaching of PpIX. Photobleaching is proportional to the power of the excitation light. Total photobleaching of the PpIX in the skin is faster than in the brain tumor. For the excitation power of 1-10 mW, the time of photobleaching was 20-50 s in the skin and 40-80 s in the brain.

Using the pulsed modulation a range of pulse widths were applied on the skin. Some pulse widths induced a faster photobleaching than the continuous excitation. In the brain, modulated excitation induced faster photobleaching than the continuous mode. In conclusion, to keep the photobleaching induced by the system at minimum, the time of exposure was adjusted to the time when only 10% of the fluorescence was reduced (two pulses at 5 mW and 0.5 s).

Paper IV- Photobleaching-insensitive fluorescence diagnostics in skin and brain tissue

In this paper, photobleaching was studied in a continuation of Paper III using principal component analysis (PCA). Photobleaching accompanies surface fluorescence measurements specifically when the brain tissue is exposed to the strong light of the surgical lamps and microscope in the operating room. As the fluorescence signal quantification in many cases is expected to be affected by photobleaching prior to the start of the measurement, it was of interest to develop a method to predict the initial value of fluorescence. In this regard, a dynamic model was developed to predict the

photobleaching behavior based on convergence and decay rates of fluorescence from long measurement series at each point. Measurements were performed on the skin of volunteers ($n = 4$) and brain tumors ($n = 2$), respectively.

By applying PCA to the photobleaching sequences on each measurement site, a spectral component for each of the autofluorescence, PpIX fluorescence, blue shift and noise was obtained. A system matrix was then defined using the fluorescence decay rates from which spectral composition at infinity was derived. Fluorescence quantification was performed on the principal components of the initial and estimated infinity signals. The same fluorescence ratio defined in the earlier publications was used on the components. The fluorescence ratio obtained for initial moment and the infinity show a high correlation in the skin suggesting the potential of the method for correcting the photobleaching effect.

The influence of excitation power and modulation was investigated on the defined PpIX ratio, blue shift ratio and the PpIX fluorescence lifetime. Modulation did not show any influence on the blue shift but it resulted in a faster photobleaching. In agreement with Paper III, excitation power resulted in a faster photobleaching; however, at higher excitation powers photobleaching was saturated.

Paper V- Compensation for blood interference in the tissue fluorescence - application in fluorescence guided brain tumor resection

Blood often disturbed the fluorescence signals during the intraoperative measurements. In this case, blood interfered with optical signals and affected the quantification of the signals in the presence of PpIX. Blood was frequently rinsed with saline during the surgery but still many signals were distorted as a result of blood being in front of the probe. In this paper, this problem was investigated by developing a theoretical model based on Beer-Lambert Law and linear fitting of fluorescence versus excitation fluence, to model the pattern of blood interference. Intraoperative measurements were experimentally re-produced in the laboratory by placing blood drops on the skin. Both models showed a good agreement with the data collected from brain tumor resection. To evaluate the estimated amount of blood by the model, confocal microscopy was used.

According to the theoretical model, the optical signal to and from the tissue is blocked by an approximately 300 μm blood layer. The model showed an overestimation in the fluorescence ratio calculated from the distorted signal. Distortion was corrected for the blood layers thinner than 50 μm by defining a correction factor multiplied by the fluorescence ratio. The correction factor was calculated based on the developed theoretical model. Compensation performed on blood-distorted signals from one patient, showed a reduction in the median of the fluorescence ratio but there was no significant statistical difference between the distorted and corrected data sets.

Chapter 11

Discussion and Conclusions

In this thesis, fluorescence spectroscopy was evaluated as an intraoperative guiding tool for resection of the most malignant brain tumor, glioblastoma. In addition to system development, challenges of intraoperative measurements and signal quantification including photobleaching and blood interference were addressed throughout the thesis. The issues regarding the applied techniques, diagnostic performance, comparison of similar observations by other research groups and the future steps are discussed in this chapter.

Suppression of the Operating Room Lamps

Any type of optical source interferes with fluorescence signals. Ideally, the operating room should be darkened during the measurements; however, this is difficult since having a proper view of the surgical area is necessary. In an earlier generation of the system, the light has been suppressed by a plastic funnel at the tip of the probe [141]. The funnel proved to be successful in obstructing the light from the fluorescence spectrum; however, it blocked the surgeon's view from the measurement location.

Suppression of the ambient light by system modulation was adequate when applied to lamps of low optical power; i.e., fluorescent tubes in the laboratory and in the operating room. High optical power lights were to a great extent omitted; however, the total omission in the direct focus of the light was not possible as the scans generated by the spectrometer did not have perfectly equal integration times (pulse widths) and differed for several microseconds. Therefore, during the operation, the surgical microscope was shaded by the hand of the surgeon when holding the probe. A system that collects a few individual spectral bands by using photodiodes or photomultipliers instead of a spectrometer will be able to generate pulses in the kHz range. Elimination of high power light sources in the operating room may be possible with this design.

Signal Quantification and Diagnostic Performance

To obtain an absolute value for the PpIX fluorescence ratio which corresponds to a specific tumor or malignancy is a challenging task as the values vary to a great deal within one patient and among patients. One argument on the variability of ALA is the time of application. This was however not considered to affect the fluorescence intensity within 2-9 hours (Figure 41). Other arguments put forward photobleaching and individual tumor uptake of ALA.

Blood was a major challenge for fluorescence measurements that caused overestimation in the calculated fluorescence ratio. The correction of the distorted signals made the retrieval of the signals otherwise excluded from the quantification analysis possible. As the method was developed in the later phase of the thesis, the calibration measurements were only performed in one patient and the blood distorted signals were excluded from the data included in Chapter 9. In future clinical measurement routines,

calibration measurements are recommended for each surgical procedure to allow compensation for blood interference.

The implemented fluorescence ratio was considered superior to the ratio suggested in Eq. 11 [127] for quantification of fluorescence since it showed a higher test efficiency. The ability of the fluorescence ratio to classify the degree of malignancy (low or high) was evaluated by discriminant function analysis. The data collected were insufficient for reliable discriminant training; however, a test efficiency of 100% and 50% was obtained for confirmed low and high grade glioma biopsies, respectively.

The measurement on one confirmed high grade glioma did not reveal any native PpIX although reported differently in the literature [69]. Therefore the effect of endogenous PpIX was not supposed to affect the quantification. Two tumors with confirmed high malignancy grade did not show any fluorescence. The reason is unknown; however, the fact that the corresponding measurements were performed in the early stage of the study for training, might have affected the indications. The method has so far been aimed at the highly malignant GBM and recurrent GBM; however, as reviewed in Chapter 4 (Table 4), several other tumor types have responded positively to ALA. One study in the future could be to investigate the response of tumor types other than GBM to ALA.

The diagnostic performance of the system was evaluated by binominal categorization of PpIX fluorescence (Table 11). A larger dataset is required to confirm the values; however, the evaluation was included to give an overall view of the performance of the method. A high sensitivity and test efficiency is obtained by OTP but the specificity was low due to the fact that biopsies were taken from the suspected malignant tumors rather than suspected healthy tissue. Other groups who investigated the fluorescence response of the tumor report on high performance values (Table 5). At the next step for diagnostic performance evaluation, the entire resection could be guided based on the OTP. The outcome could then be compared to the extent of resection calculated from the pre-operative and post-operative MR images.

Distribution pattern of PpIX fluorescence at cellular level may explain the reason for fluorescence variation among samples. The fluorescence at the cellular level can be monitored using two main methods of confocal fluorescence microscopy or flow cytometry. Flow cytometers are suitable for measuring the fluorescence intensity of each cell and in advanced equipment may be combined with cell imaging options where fluorescence inside the cell structures may be imaged [142, 143]. Confocal fluorescence microscopy however offers the simultaneous pathological examination of the cells; i.e., each cell can at the same time be diagnosed for its pathology and fluorescence intensity. It has been reported [144] and seen in test measurements at Linköping University Hospital (unpublished data) that not all of the high malignant GBM cells fluoresce. It is of interest to investigate the causes behind this observation.

Photobleaching

As described in Chapter 8 and Paper III photobleaching due to the excitation light of the OTP was calculated and set to be minimal; thus the photobleaching induced by the OTP system was insignificant. However, PpIX is photobleached as a result of being exposed to the surgical lamp and the surgical microscope when the measurements are performed on tissue surface. The commercial surgical microscopes adapted to detect fluorescence, filter the blue part of the light (below 440 nm) when the microscope

operates in the white light mode. This is done to prevent rapid photobleaching of the PpIX as it has high absorption in the blue region; nevertheless, the PpIX is still photobleached by longer wavelengths. The time that fluorescence photobleaches to 36% of its intensity is reported to be 25 minutes and 87 minutes respectively for the blue and white light microscopy at 20 mg/kg [42]. Photobleaching lifetime was much shorter (less than one minute) for OTP using 5 mg/kg ALA. Since photobleaching is dependent on the concentration of oxygen and photosensitizer [66], the different excitation power of the microscope, the higher ALA dose or the starting point of measurements are the possible causes for this difference in fluorescence lifetime.

The PCA-based dynamic model (Paper IV) suggested a method to predict the initial amount of fluorescence from the photobleached fluorescence spectra. This method was however not applicable to the current generation of the system in the operating room as a large number of spectra at each point was needed. Excitation power and pulsation settings influence the photobleaching lifetime. To precisely associate the pulse settings with photobleaching and taking into consideration the oxygen diffusion time in the tissue, more investigation on the duty cycle and the pulse width is needed.

Comparison of Fluorescence Spectroscopy with Fluorescence Microscopy

The first clinical trials for ALA-guided brain tumor surgery were performed by fluorescence microscopy. The fluorescence microscopes are rapidly replacing the conventional neurosurgical microscopes for clinical use in many countries. In Europe it is used in clinic routines since 2007 while in some other countries including the USA, Australia and some Asian countries it is at the stage of clinical trials prior to approval.

Fluorescence microscopy provides an overview of the tumor; however, it is restricted in several other aspects. One main limitation of microscopy is the high detection threshold which results in missing the weak fluorescence signals. Combined fluorescence spectroscopy and microscopy measurements showed that some points which appeared to be blue (normal) in the microscope, were detected as fluorescent using OTP (unpublished data). Consistently, Valdes et al., obtained higher test efficiency (87% versus 66%) with the spectroscopy method than with microscopy method [114]. Moreover, fluorescence detection using microscopy is subjective and based on the surgeon's categorization of the fluorescence intensity as vague or solid.

Using a probe for fluorescence spectroscopy gives the advantage of examining the tumor extent in depth by inserting the probe in the tumor while microscopy is limited to the surface view only. Also to consider is the post-op patient care and ALA costs imposed on clinics when a 20 mg/kg dose is used. The 24-48 hours incubation in a dark room [42] may not be a burden as the patients stay at post-op care routinely. However, no skin sensitization is induced when a 5 mg/kg ALA dose is administered (unpublished data).

Complimentary Technologies

Fluorescence spectroscopy was compared to ultrasound-based navigation as a reference method and for registering the location of the measurement site on ultrasound images at the same instant it was measured. Complementary performance of fluorescence spectroscopy and ultrasound-based navigation was evaluated as positive. However, the

OTP and US are both unable to detect the tumor cell infiltrations and might both indicate gliosis as a tumor [40].

Various optical modalities have been developed for non-invasive in vivo screening of surface malignancies (e.g. skin tumors) based on tissue functionality, metabolism or structure. However, few of these modalities have been used during actual surgical procedures mainly due to limitations of device-tissue interface, bulky instrumentation, long measurement time and off-line data processing requirements [145]. Optical methods that have so far been implemented for in vivo human brain studies are fluorescence microscopy [43, 146] and a feasibility study with a hand-held confocal microscope [147].

Integration of other optical methods with the fluorescence spectroscopy is possible through the addition of extra optical fibers in the probe. Optical coherence tomography (OCT) and DRS are the only optical methods available in the fiber-optical form as of today. Results from DRS although indicative, are not reliable for clinical diagnosis [76]. OCT is a potential complementary method to fluorescence spectroscopy as it provides high resolution ($\sim 1 \mu\text{m}$) images of the tissue microstructures 2-3 mm deep. Feasibility of OCT for human brain tumor detection has been investigated in one study so far [148]. The multiphoton fluorescence imaging method is compatible with ALA properties [149] and is useful in terms of inducing less photobleaching and deeper penetration in blood and tissue due to the longer excitation wavelengths used. However, it is not yet available in the fiber-optic mode [150].

Conclusion

Fluorescence spectroscopy was evaluated as being a feasible technique for quantitative demarcation of glioblastoma. Fluorescence signals were quantified and the technical challenges including photobleaching and blood interference were studied. Photobleaching sequences were explained by three major components using principal component analysis. Different system settings were found to influence the fluorescence lifetime. Blood absorption caused an overestimation in the fluorescence ratio and the error was corrected based on a theoretical model. Ultrasound-based neuronavigation was considered a complementary technology for fluorescence point measurements. Clinical evaluation of the method showed that the presence of fluorescence was associated with the tissue pathologically diagnosed as malignant. Fluorescence ratios were indicative of tumor tissue malignancy degree.

Acknowledgements

I would like to acknowledge the financial support from the Swedish Foundation for Strategic Research (SSF), Swedish Research Council (VR, grant number 621-2008-3013), Swedish Governmental Agency for Innovation Systems (VINNOVA, group grant number 311-2006-7661) and NovaMedTech (Swedish Agency for Economic and Regional Growth, grant number 160382).

This thesis would have not been possible without the support of individuals and organizations at many levels, directly and indirectly, from past to the present. I owe this moment to those who gave me opportunities, guided me, encouraged me and above all gave me constructive criticism.

First and foremost, I am heartily grateful to my supervisor *Professor Karin Wårdell* for believing in me and giving me the opportunity to work on this very interesting project. Your encouragement, involvement and enthusiasm made the work joyful. The work was demanding but never boring or tiring! The OTP team, *Stefan Andersson-Engels* (and the group at Lund Medical Laser Center), *Johan Richter*, *Martin Hallbeck*, *Ola Svärm*, *Malin Svensson*, *Mikkel Brydegaard* and *Haiyan Xie* it has been a pleasure to work with you! The surgeons and staff at the Department of Neurosurgery, Linköping University Hospital who were involved in one way or another, my thanks for all the arrangements and measurements!

Colleagues at IMT, you have been so kind. *Göran Salerud*, I am glad to have had a caring co-supervisor. *Prof. Åke Öberg*, thanks for being my half-time opponent. *Tomas Stromberg*, *Marcus Larsson*, *Ingmar Fredriksson* and *Hanna Karlsson*, thanks for commenting on my thesis and the every now and then optical discussions. *Mats Andersson*, *Olivier Cros*, *Rodrigo Moreno* and *Anders Eklund*, thanks for discussions on image processing. Undergraduate students who did your thesis with me, *Ali Aghajani*, *Shannely Lowndes* and *Fabian Balsiger*, it was great to work with you. The MINT group, *Peter Rejmstad*, *Malcolm Lattorre*, *Mattias Åström* and *Elin Diczfalusy*, my thanks for your company. *Bengt Ragnemalm*, *Per Sveider*, *Mats Andersson* and *Malcolm Lattorre* your technical support was much appreciated. *Martin Eneling*, was fun with all the diverse discussions! The IMT administration team, you do a great job and are wonderful!

I would also like to thank *Professor Bruce Tromberg*, *Dr. Darren Roblyer*, *Dr. Albert Cerussi* and all the people I met at the Beckman Laser Institute, UC Irvine, for hosting me and giving me a great time during my stay. Visiting your group was scientifically inspirational and guiding. *Dr. Leigh Johnston* at the Neuroengineering Department, Melbourne University, it was a great pleasure to know you and spend time at the University of Melbourne. *Dr. Andrei Zvygin*, thanks for hosting me at the Optical Biomedical Imaging and Sensing group at the Macquarie University; *Dr. Stephen Williams*, *Geoff Osborne* and *Dr. Yonghui Li*, my thanks for the interesting discussions at the Queensland Brain Institute. *Jonas Gårdin* and *Malin Svensson*, thank you for hosting me at Elekta AB in Stockholm. Most of all, I am grateful to the *AgoraLink committee* who provided me with the unique opportunity to make these visits during my PhD studies.

Last but not least, I am indebted to my parents, my family and friends for supporting me on this road. *Sholeh* and *Shirin Fazel*, *Ursula* and *Heinz Nikola* thanks for your love, encouragement and for being my secondary family during this time!

References

- [1] D. N. Louis, H. Ohgaki, and O. Wiestler, *WHO classification of tumours of the central nervous system*, 4 ed.: International Agency for Research on Cancer, 2007.
- [2] M. Lacroix, D. Abi-Said, D. R. Fournay, Z. L. Gokaslan, W. Shi, F. Demonte, F. F. Lang, I. E. Mccutcheon, S. J. Hassenbusch, E. Holland, K. Hess, C. Michael, and D. a. S. Miller, Raymond, "A multivariate analysis of 416 patients with glioblastoma multiforme: prognosis, extent of resection, and survival," *Journal of neurosurgery*, vol. 95, pp. 190–198, 2001.
- [3] W. Stummer, H.-J. Reulen, T. Meinel, U. Pichlmeier, W. Schumacher, J.-C. Tonn, V. Rohde, F. Oettel, B. Turowski, C. Woiciechowsky, K. Franz, and T. Pietsch, "Extent of resection and survival in glioblastoma multiforme: Identification of and adjustment for bias.," *Neurosurgery-online*, vol. 62, pp. 564-576, 2008.
- [4] W. A. Hall, C. Nimsky, and C. L. Truwit, Eds., *Intraoperative MRI-Guided Neurosurgery*. New York: Thieme Medical Publishers Inc, 2010.
- [5] W. Stummer, U. Pichlmeier, T. Meinel, O. D. Wiestler, F. Zanella, and H. J. Reulen, "Fluorescence-guided surgery with 5-aminolevulinic acid for resection of malignant glioma: a randomised controlled multicentre phase III trial," *The Lancet Oncology*, vol. 7, p. 392, 2006.
- [6] B. Krammer and K. Plaetzer, "ALA and its clinical impact, from bench to bedside," *Photochemical & Photobiological Sciences*, vol. 7, pp. 283-289, 2008.
- [7] F. H. Martini, *Fundamentals of Anatomy and Physiology*, Sixth ed.: Pearson Education, 2004.
- [8] G. Tortora and S. R. Grabowski, *Principles of Anatomy and Physiology*, Ninth ed.: John Wiley & Sons, 2000.
- [9] R. F. Tuma, "Chapter 11 - The Cerebral Microcirculation," in *Microcirculation (Second Edition)*, F. T. Ronald, N. D. Walter, W. N. D. Klaus LeyA2 - Ronald F. Tuma, and L. Klaus, Eds., ed San Diego: Academic Press, pp. 485-520, 2008.
- [10] F. A. Azevedo, L. R. Carvalho, L. T. Grinberg, J. M. Farfel, R. E. Ferretti, R. E. Leite, W. Jacob Filho, R. Lent, and S. Herculano-Houzel, "Equal numbers of neuronal and nonneuronal cells make the human brain an isometrically scaled-up primate brain," *The Journal of Comparative Neurology*, vol. 513, pp. 532-541, 2009.
- [11] L. Lundy-Ekman, *Neuroscience: Fundamentals for Rehabilitation*, second ed. Philadelphia: Elsevier Science, 2002.
- [12] S. Nag, *The Blood-Brain Barrier, Biology and Research Protocols*. New Jersey: Humana Press Inc. , 2003.
- [13] National Cancer Institute. (2012, 04/06/2012). *Defining Cancer*. Available: <http://cancer.gov/cancertopics/cancerlibrary/what-is-cancer>
- [14] World Health Organization. (2011, 07/28/2011). *Health topics-Cancer*. Available: <http://www.who.int/topics/cancer/en/>
- [15] L. M. Franks and N. M. Teich, *Introduction to Cellular and Biology of Cancer*. London: Bath Press Ltd., 1997.
- [16] Central Brain Tumor Registry of the United States. (2012, 07/07/2012). *Primary Brain and Central Nervous System Tumors Diagnosed in the United States in 2004-2008*. Available: <http://www.cbtrus.org/reports/reports.html>
- [17] A. Jemal, R. Siegel, J. Xu, and E. Ward, "Cancer Statistics, 2010," *CA Cancer J Clin*, p. caac.20073, July 7, 2010.

- [18] J. Ferlay, D. M. Parkin, and E. Steliarova-Foucher, "Estimates of cancer incidence and mortality in Europe in 2008," *European Journal of Cancer*, vol. 46, pp. 765-781, 2010.
- [19] J. Wiemels, M. Wrensch, and E. Claus, "Epidemiology and etiology of meningioma," *Journal of Neuro-Oncology*, vol. 99, pp. 307-314, 2010.
- [20] J. Raizer, "Meningiomas," *Current Treatment Options in Neurology*, vol. 12, pp. 360-368, 2010.
- [21] A. D. Norden and E. B. Claus, "Benign and Malignant Tumors of the Brain" in "Principles and Practice of Geriatric Surgery," R. A. Rosenthal, M. E. Zenilman, and M. R. Katlic, Eds., ed: Springer New York, pp. 1151-1164, 2011.
- [22] J. B. Aragon-Ching and J. A. Zujewski, "CNS Metastasis: An Old Problem in a New Guise," *Clinical Cancer Research*, vol. 13, pp. 1644-1647, March 15, 2007.
- [23] W. Mason, "Oligodendroglioma," *Current Treatment Options in Neurology*, vol. 7, pp. 305-314, 2005.
- [24] CERN Foundation. (2010, 07/07/2012). *Distribution of All Primary Brain and CNS Tumors by Histology*. Available: <http://www.cern-foundation.org/Content.aspx?id=830>
- [25] N. Sanai, S. Chang, and M. S. Berger, "Low-grade gliomas in adults," *Journal of neurosurgery*, vol. 115, pp. 948-965, 2011.
- [26] J. D. Weingart, M. J. McGirt, and H. Brem, "High-Grade Astrocytoma/Glioblastoma," in *Neuro-Oncology of CNS Tumors*, J.-C. Tonn, S. A. Grossman, J. T. Rutka, and M. Westphal, Eds., ed: Springer Berlin Heidelberg, pp. 127-138, 2006.
- [27] L. Oliver, C. Olivier, F. B. Marhuenda, M. Campone, and F. M. Vallette, "Hypoxia and the Malignant Glioma Microenvironment: Regulation and Implications for Therapy " *Current Molecular Pharmacology*, vol. 2, pp. 263-284, 2009.
- [28] S. Vishal, G.-G. Ignacio, and E. L. Walter, "A noninvasive multimodal technique to monitor brain tumor vascularization," *Physics in Medicine and Biology*, p. 5295, 2007.
- [29] S. Schneider, T. Ludwig, L. Tatenhorst, S. Braune, H. Oberleithner, V. Senner, and W. Paulus, "Glioblastoma cells release factors that disrupt blood-brain barrier features," *Acta Neuropathologica*, vol. 107, pp. 272-276, 2004.
- [30] S. M. Russell, R. Elliott, D. Forshaw, J. G. Golfinos, P. K. Nelson, and P. J. Kelly, "Glioma vascularity correlates with reduced patient survival and increased malignancy," *Surgical Neurology*, vol. 72, p. 242, 2009.
- [31] A. H. Kaye and E. Laws, *Brain Tumors, An encyclopedic approach*, 2 ed.: Churchill Livingstone, 2001.
- [32] L. C. Hou, A. Veeravagu, A. R. Hsu, and V. C. K. Tse, "Recurrent glioblastoma multiforme: a review of natural history and management options," *Neurosurgical FOCUS*, vol. 20, p. E3, 2006.
- [33] E. C. Holland, "Glioblastoma multiforme: The terminator," *Proceedings of the National Academy of Sciences*, vol. 97, pp. 6242-6244, June 6, 2000.
- [34] S. Tatter, "Recurrent malignant glioma in adults," *Current Treatment Options in Oncology*, vol. 3, pp. 509-524, 2002.
- [35] J. Wood, S. Green, and W. Shapiro, "The prognostic importance of tumor size in malignant gliomas: a computed tomographic scan study by the Brain Tumor Cooperative Group," *Journal of Clinical Oncology*, vol. 6, pp. 338-343, February 1, 1988.
- [36] T. Hartkens, D. L. G. Hill, A. D. Castellano-Smith, D. J. Hawkes, C. R. Maurer, Jr., A. J. Martin, W. A. Hall, H. Liu, and C. L. Truwit, "Measurement and analysis of brain deformation during neurosurgery," *Medical Imaging, IEEE Transactions on*, vol. 22, pp. 82-92, 2003.

- [37] A. Nabavi, U. Blömer, and H. Maximilian Mehdorn, "Clinical Aspects of Gliomas," *Medical Laser Application*, vol. 17, pp. 91-104, 2002.
- [38] G. Bertani, E. Fava, G. Casaceli, G. Carrabba, A. Casarotti, C. Papagno, A. Castellano, A. Falini, S. M. Gaini, and L. Bello, "Intraoperative mapping and monitoring of brain functions for the resection of low-grade gliomas: technical considerations," *Neurosurgical FOCUS*, vol. 27, p. E4, 2009.
- [39] N. Sanai and M. S. Berger, "Intraoperative stimulation techniques for functional pathway preservation and glioma resection," *Neurosurgical FOCUS*, vol. 28, p. E1, 2010.
- [40] G. Unsgaard, T. Selbekk, T. Brostrup Müller, S. Ommedal, S. H. Torp, G. Myhr, J. Bang, and T. A. Nagelhus Hernes, "Ability of navigated 3D ultrasound to delineate gliomas and metastases – comparison of image interpretations with histopathology," *Acta Neurochirurgica*, vol. 147, p. 1259, 2005.
- [41] G. Unsgaard, O. M. Rygh, T. Selbekk, T. B. Müller, F. Kolstad, F. Lindseth, and T. A. N. Hernes, "Intra-operative 3D ultrasound in neurosurgery," *Acta Neurochirurgica*, vol. 148, p. 235, 2006.
- [42] J.-C. Tonn and W. Stummer, "Fluorescence-guided resection of malignant gliomas using 5-aminolevulinic acid: practical use, risks, and pitfalls," *Clin Neurosurg*, vol. 55, pp. 20-6, 2008.
- [43] M. S. Eljamel, "Brain photodiagnosis (PD), fluorescence guided resection (FGR) and photodynamic therapy (PDT): Past, present and future," *Photodiagnosis and Photodynamic Therapy*, vol. 5, p. 29, 2008.
- [44] A. Pesce, M. Bolognesi, A. Bocedi, P. Ascenzi, S. Dewilde, L. Moens, T. Hankeln, and T. Burmester, "Neuroglobin and cytoglobin," *EMBO reports*, vol. 3, pp. 1146-1151, 2002.
- [45] Biomedical Optics Research Laboratory. (2005, 06/20/2012). *Specific Extinction Spectra of Tissue Chromophores*. Available: http://www.medphys.ucl.ac.uk/research/borl/research/NIR_topics/spectra/spectra.htm
- [46] Oregan Medical Laser Center. (2001, 04/03/2010). *Optical properties spectra*. Available: <http://omlc.ogi.edu/spectra/index.html>
- [47] D. A. Boas, C. Pitris, and N. Ramanujam, Eds., *Handbook of Biomedical Optics*. Boca Raton: CRC Press, 2011.
- [48] T. Vo-Dinh, Ed., *Biomedical Photonics Handbook*. CRC Press, 2003.
- [49] E. B. Hanlon, R. Manoharan, T. W. Koo, K. E. Shafer, J. T. Motz, M. Fitzmaurice, J. R. Kramer, I. Itzkan, R. R. Dasari, and M. S. Feld, "Prospects for in vivo Raman spectroscopy," *Physics in Medicine and Biology*, vol. 45, p. R1, 2000.
- [50] R. Splinter and B. A. Hooper, *An Introduction to Biomedical Optics*: Taylor and Francis, 2007.
- [51] H. Buiteveld, J. M. Hakvoort, and M. Donze, "The optical properties of pure water," in *SPIE Proceedings on Ocean Optics XII*, 1994, pp. 174-183.
- [52] R. L. P. van Veen, H. J. C. M. Sterenborg, A. Pifferi, A. Torricelli, and R. Cubeddu, "Determination of VIS- NIR absorption coefficients of mammalian fat, with time and spatially resolved diffuse reflectance and transmission spectroscopy," in *OSA Annual BIOMED Topical Meeting*, 2004.
- [53] S. Prahl. (1998). *Melanosome absorption coefficient*. Available: <http://omlc.ogi.edu/spectra/melanin/mua.html>
- [54] S. A. Prahl, "Light Transport in Tissue," PhD, University of Texas in Austin, Austin, 1988.
- [55] G. Müller and A. Roggan, Eds., *Laser-Induced Interstitial Thermo-therapy*. Washington: SPIE-The International Society for Optical Engineering, 1995.

- [56] S. L. Jacques and S. A. Prahl. (1998). *ECE532 Biomedical Optics*. Available: <http://omlc.ogi.edu/education/ece532/class3/musp.html>
- [57] S. L. Jacques and B. W. Pogue, "Tutorial on diffuse light transport," *Journal of Biomedical Optics*, vol. 13, p. 041302, 2008.
- [58] A. N. Yaroslavsky, P. C. Schulze, I. V. Yaroslavsky, R. Schober, F. Ulrich, and H. J. Schwarzmaier, "Optical properties of selected native and coagulated human brain tissues in vitro in the visible and near infrared spectral range," *Physics in medicine and biology*, vol. 47, pp. 2059-2073, 2002.
- [59] D. J. Faber, M. C. G. Aalders, E. G. Mik, B. A. Hooper, M. J. C. van Gemert, and T. G. van Leeuwen, "Oxygen Saturation-Dependent Absorption and Scattering of Blood," *Physical Review Letters*, vol. 93, p. 028102, 2004.
- [60] S. Prahl. (2001, 2011). *Optical Absorption of Hemoglobin*. Available: <http://omlc.ogi.edu/spectra/hemoglobin/index.html>
- [61] H. J. Schwarzmaier, F. Eickmeyer, V. U. Fiedler, and F. Ulrich, "Basic Principles of Laser Induced Interstitial Thermotherapy in Brain Tumors," *Medical Laser Application*, vol. 17, pp. 147-158, 2002.
- [62] A. Roggan, "Dosimetrie thermischer Laseranwendungen in der Medizin," Dissertation, Laser und Medizin Technologie, Technische Universität Berlin, 1997.
- [63] J. R. Lakowicz, *Principles of Fluorescence Spectroscopy*, Second ed. New York: Kluwer Academic/ Plenum Publishers, 1999.
- [64] J. F. Lovell, T. W. B. Liu, J. Chen, and G. Zheng, "Activatable Photosensitizers for Imaging and Therapy," *Chemical Reviews*, vol. 110, pp. 2839-2857, 2010/05/12.
- [65] G. Hennig, H. Stepp, and A. Johansson, "Photobleaching-based method to individualize irradiation time during interstitial 5-aminolevulinic acid photodynamic therapy," *Photodiagnosis and Photodynamic Therapy*, vol. 8, pp. 275-281, 2011.
- [66] I. J. Macdonald and T. J. Dougherty, "Basic principles of photodynamic therapy," *Journal of Porphyrins and Phthalocyanines*, vol. 5, pp. 105-129, 2001.
- [67] E. Udd and W. B. Spillman, *Fiber Optic Sensors: An Introduction for Engineers and Scientists.*, Second ed.: John Wiley & Sons 2011.
- [68] R. S. Bradley and M. S. Thorniley, "A review of attenuation correction techniques for tissue fluorescence," *Journal of The Royal Society Interface*, vol. 3, pp. 1-13, February 22, 2006.
- [69] S. Andersson-Engels, Å. Elner, J. Johansson, S. E. Karlsson, L. G. Salford, L. G. Strömblad, K. Svanberg, and S. Svanberg, "Clinical recording of laser-induced fluorescence spectra for evaluation of tumour demarcation feasibility in selected clinical specialities," *Lasers in Medical Science*, vol. 6, pp. 415-424, 1991.
- [70] Z. Huang, W. Zheng, S. Xie, R. Chen, H. Zeng, D. I. McLean, and H. Lui, "Laser-induced autofluorescence microscopy of normal and tumor human colonic tissue," *Int J Oncol*, vol. 24, pp. 59-63, 2004.
- [71] A. C. Croce, F. Sabrina, D. Locatelli, R. Nano, M. Ceroni, F. Tancioni, E. Giombelli, E. Benericetti, and G. Bottiroli, "Diagnostic Potential of Autofluorescence for an Assisted Intraoperative Delineation of Glioblastoma Resection Margins," *Photochemistry and Photobiology*, vol. 77, pp. 309-318, 2003.
- [72] A. C. Croce, U. D. Simone, I. Freitas, E. Boncompagni, D. Neri, U. Cillo, and G. Bottiroli, "Human liver autofluorescence: An intrinsic tissue parameter discriminating normal and diseased conditions," *Lasers in Surgery and Medicine*, vol. 42, pp. 371-378, 2010.

- [73] J. R. Albani, *Principles and applications of fluorescence spectroscopy*: Blackwell Science, 2007.
- [74] G. A. Wagnieres, W. M. Star, and B. C. Wilson, "In Vivo Fluorescence Spectroscopy and Imaging for Oncological Applications," *Photochemistry and Photobiology*, vol. 68, pp. 603-632, 1998.
- [75] Y. G. Chung, J. A. Schwartz, C. M. Gardner, R. E. Sawaya, and S. L. Jacques, "Diagnostic potential of laser-induced autofluorescence emission in brain tissue," *J Korean Med Sci*, vol. 12, p. 135, 1997.
- [76] S. A. Toms, W.-C. Lin, R. J. Weil, M. D. Johnson, D. E. Jansen, and A. Mahadevan-Jansen, "Intraoperative Optical Spectroscopy Identifies Infiltrating Glioma Margins with High Sensitivity," *Neurosurgery*, vol. 57, pp. 382-391, 2005.
- [77] B. W. Pogue, S. L. Gibbs-Strauss, Valde, x, P. A. s, K. S. Samkoe, D. W. Roberts, and K. D. Paulsen, "Review of Neurosurgical Fluorescence Imaging Methodologies," *Selected Topics in Quantum Electronics, IEEE Journal of*, vol. 16, p. 493, 2010.
- [78] W. C. Lin, S. A. Toms, M. Johnson, E. D. Jansen, and A. Mahadevan-Jansen, "In Vivo Brain Tumor Demarcation Using Optical Spectroscopy," *Photochemistry and Photobiology*, vol. 73, pp. 396-402, 2001.
- [79] J. C. Finlay, "Reflectance and Fluorescence Spectroscopies in Photodynamic Therapy," PhD, Physics and Astronomy, University of Rochester, Rochester, 2003.
- [80] M. S. Eljamel, "Fluorescence image-guided surgery of brain tumors: Explained step-by-step," *Photodiagnosis and Photodynamic Therapy*, vol. 5, p. 260, 2008.
- [81] H. Hirschberg, C.-H. Sun, B. J. Tromberg, and S. J. Madsen, "ALA- and ALA-ester-mediated Photodynamic Therapy of Human Glioma Spheroids," *Journal of Neuro-Oncology*, vol. 57, pp. 1-7, 2002.
- [82] S. Stylli, M. Howes, L. MacGregor, P. Rajendra, and A. H. Kaye, "Photodynamic therapy of brain tumours: evaluation of porphyrin uptake versus clinical outcome," *Journal of Clinical Neuroscience*, vol. 11, pp. 584-596, 2004.
- [83] L. Ma, J. Moan, and K. Berg, "Comparison of the photobleaching effect of three photosensitizing agents: Meso-tetra(m-hydroxyphenyl) chlorin, meso-tetra (m-hydroxyphenyl) porphyrin and photofrin during photodynamic therapy," *Lasers in Medical Science*, vol. 9, pp. 127-132, 1994.
- [84] M. Eljamel, C. Goodman, and H. Moseley, "ALA and Photofrin® Fluorescence-guided resection and repetitive PDT in glioblastoma multiforme: a single centre Phase III randomised controlled trial," *Lasers in Medical Science*, vol. 23, pp. 361-367, 2008.
- [85] A. Zimmermann, M. Ritsch-Marte, and H. Kostron, "mTHPC-mediated Photodynamic Diagnosis of Malignant Brain Tumors," *Photochemistry and Photobiology*, vol. 74, pp. 611-616, 2001.
- [86] M. B. Ericson, S. Grapengiesser, F. Gudmundson, A. M. Wennberg, O. Larkö, J. Moan, and A. Rosén, "A spectroscopic study of the photobleaching of protoporphyrin IX in solution," *Lasers in Medical Science*, vol. 18, p. 56, 2003.
- [87] R. Pottier, B. Krammer, R. Baumgartner, and H. Stepp, Eds., *Photodynamic therapy with ALA: a clinical handbook*. Dorchester: The Royal Society of Chemistry, 2006.
- [88] Q. Peng, K. Berg, J. Moan, M. Kongshaug, and J. M. Nesland, "5-Aminolevulinic Acid-Based Photodynamic Therapy: Principles and Experimental Research," *Photochemistry and Photobiology*, vol. 65, pp. 235-251, 1997.
- [89] A. Novotny and W. Stummer, "5-Aminolevulinic Acid and the Blood-Brain Barrier - A Review," *Medical Laser Application*, vol. 18, p. 36, 2003.

- [90] S. Collaud, A. Juzeniene, J. Moan, and N. Lange, "On the Selectivity of 5-Aminolevulinic Acid-Induced Protoporphyrin IX Formation," *Current Medicinal Chemistry - Anti-Cancer Agents*, vol. 4, pp. 301-316, 2004.
- [91] S. R. Ennis, A. Novotny, J. Xiang, P. Shakui, T. Masada, W. Stummer, D. E. Smith, and R. F. Keep, "Transport of 5-aminolevulinic acid between blood and brain," *Brain Research*, vol. 959, pp. 226-234, 2003.
- [92] S. L. Gibson, M. L. Nguyen, J. J. Havens, A. Barbarin, and R. Hilf, "Relationship of [delta]-Aminolevulinic Acid-Induced Protoporphyrin IX Levels to Mitochondrial Content in Neoplastic Cells in Vitro," *Biochemical and Biophysical Research Communications*, vol. 265, p. 315, 1999.
- [93] J. Moan, J. T. Van Den Akker, P. Juzenas, L. W. Ma, E. Angell-Petersen, Ø. B. Gadmar, and V. Iani, "On the basis for tumor selectivity in the 5-aminolevulinic acid-induced synthesis of protoporphyrin IX," *Journal of Porphyrins and Phthalocyanines*, vol. 5, pp. 170-176, 2001.
- [94] P. A. Valdés, K. Samkoe, J. A. O'Hara, D. W. Roberts, K. D. Paulsen, and B. Pogue, W., "Deferoxamine Iron Chelation Increases delta-Aminolevulinic Acid Induced Protoporphyrin IX in Xenograft Glioma Model," *Photochemistry and Photobiology*, vol. 86, pp. 471-475, 2010.
- [95] Y. Tamura, T. Kuroiwa, Y. Kajimoto, Y. Miki, S.-I. Miyatake, and M. Tsuji, "Endoscopic identification and biopsy sampling of an intraventricular malignant glioma using a 5-aminolevulinic acid-induced protoporphyrin IX fluorescence imaging system," *Journal of neurosurgery*, vol. 106, pp. 507-510, 2007.
- [96] R. Ritz, G. C. Feigl, M. U. Schuhmann, A. Ehrhardt, S. Danz, S. Noell, A. Bornemann, and M. S. Tatagiba, "Use of 5-ALA fluorescence guided endoscopic biopsy of a deep-seated primary malignant brain tumor," *Journal of neurosurgery*, vol. 114, pp. 1410-1413, 2011.
- [97] R. Ishihara, Y. Katayama, T. Watanabe, A. Yoshino, T. Fukushima, and K. Sakatani, "Quantitative Spectroscopic Analysis of 5-Aminolevulinic Acid-Induced Protoporphyrin IX Fluorescence Intensity in Diffusely Infiltrating Astrocytomas," *Neurologia medico-chirurgica*, vol. 47, pp. 53-57, 2007.
- [98] M. Hefti, G. v. Campe, M. Moshopulos, A. Siegner, H. Looser, and H. Landolt, "5-aminolaevulinic acid-induced protoporphyrin IX fluorescence in high-grade glioma surgery," *SWISS MED WKLY*, vol. 138, pp. 180-185, 2008.
- [99] M. Kamp, P. Grosser, J. Felsberg, P. Slotty, H.-J. Steiger, G. Reifenberger, and M. Sabel, "5-Aminolevulinic acid (5-ALA)-induced fluorescence in intracerebral metastases: a retrospective study," *Acta Neurochirurgica*, vol. 154, pp. 223-228, 2012.
- [100] S. Utsuki, H. Oka, S. Sato, S. Shimizu, S. Suzuki, Y. Tanizaki, K. Kondo, Y. Miyajima, and K. Fujii, "Histological Examination of False Positive Tissue Resection Using 5-Aminolevulinic Acid-Induced Fluorescence Guidance," *Neurologia medico-chirurgica*, vol. 47, p. 210, 2007.
- [101] M. S. Eljamel, "Which Intracranial Lesions Would Be Suitable for 5-Aminolevulinic Acid-Induced Fluorescence-Guided Identification, Localization, or Resection: A Prospective Study of 114 Consecutive Intracranial Lesions," *Clinical Neurosurgery*, vol. 56, pp. 93-97, 2009.
- [102] G. Widhalm, S. Wolfsberger, B. Kiesel, A. Mert, G. Minchev, E. Springer, A. Woehrer, D. Prayer, and E. Knosp, "5-Aminolevulinic Acid Induced Fluorescence is a Promising Marker for Rapid Progression in Low-Grade Gliomas," presented at the EANS, Rome, 2011.
- [103] G. Widhalm, S. Wolfsberger, G. Minchev, A. Woehrer, M. Krssak, T. Czech, D. Prayer, S. Asenbaum, J. A. Hainfellner, and E. Knosp, "5-Aminolevulinic acid is a promising

- marker for detection of anaplastic foci in diffusely infiltrating gliomas with nonsignificant contrast enhancement," *Cancer*, vol. 116, pp. 1545-1552, 2010.
- [104] G. C. Feigl, R. Ritz, M. Moraes, J. Klein, K. Ramina, A. Gharabaghi, B. Krischek, S. Danz, A. Bornemann, M. Liebsch, and M. S. Tatagiba, "Resection of malignant brain tumors in eloquent cortical areas: a new multimodal approach combining 5-aminolevulinic acid and intraoperative monitoring," *Journal of neurosurgery*, vol. 113, pp. 352-357, 2010.
- [105] A. Nabavi, H. Thurm, B. Zountsas, T. Pietsch, H. Lanfermann, U. Pichlmeier, and M. Mehdorn, "Five-aminolevulinic acid for fluorescence-guided resection of recurrent malignant gliomas: a phase II study," *Neurosurgery*, vol. 65, pp. 1070-1077, 2009.
- [106] A. Johansson, G. Palte, O. Schnell, J.-C. Tonn, J. Herms, and H. Stepp, "5-Aminolevulinic Acid-induced Protoporphyrin IX Levels in Tissue of Human Malignant Brain Tumors," *Photochemistry and Photobiology*, vol. 86, pp. 1373-1378, 2010.
- [107] K. Bekelis, P. A. Valdés, K. Erkmén, F. Leblond, A. Kim, B. C. Wilson, B. T. Harris, K. D. Paulsen, and D. W. Roberts, "Quantitative and qualitative 5-aminolevulinic acid-induced protoporphyrin IX fluorescence in skull base meningiomas," *Neurosurgical FOCUS*, vol. 30, p. E8, 2011.
- [108] Y. Kajimoto, T. Kuroiwa, S.-I. Miyatake, T. Ichioka, M. Miyashita, H. Tanaka, and M. Tsuji, "Use of 5-aminolevulinic acid in fluorescence-guided resection of meningioma with high risk of recurrence," *Journal of neurosurgery*, vol. 106, pp. 1070-1074, 2007.
- [109] D. Coluccia, J. Fandino, M. Fujioka, S. Cordovi, C. Muroi, and H. Landolt, "Intraoperative 5-aminolevulinic-acid-induced fluorescence in meningiomas," *Acta Neurochirurgica*, vol. 152, pp. 1711-1719, 2010.
- [110] W. Stummer, H. Stepp, G. Möller, A. Ehrhardt, M. Leonhard, and H. J. Reulen, "Technical Principles for Protoporphyrin-IX-Fluorescence Guided Microsurgical Resection of Malignant Glioma Tissue," *Acta Neurochirurgica*, vol. 140, p. 995, 1998.
- [111] Leica Microsystems AG. (2010). *Leica FL400*. Available: www.leica-microsystems.com
- [112] W. Stummer, A. Novotny, H. Stepp, C. Goetz, K. Bise, and H. J. Reulen, "Fluorescence-guided resection of glioblastoma multiforme by using 5-aminolevulinic acid-induced porphyrins : a prospective study in 52 consecutive patients," *Journal of Neurosurgery*, p. 1003:1013, 2000.
- [113] P. P. Panciani, M. Fontanella, B. Schatlo, D. Garbossa, A. Agnoletti, A. Ducati, and M. Lanotte, "Fluorescence and image guided resection in high grade glioma," *Clinical Neurology and Neurosurgery*, 2011.
- [114] P. A. Valdés, F. Leblond, A. Kim, B. T. Harris, B. C. Wilson, X. Fan, T. D. Tosteson, A. Hartov, S. Ji, K. Erkmén, N. E. Simmons, K. D. Paulsen, and D. W. Roberts, "Quantitative fluorescence in intracranial tumor: implications for ALA-induced PpIX as an intraoperative biomarker," *Journal of neurosurgery*, pp. 1-7, 2011.
- [115] S. Utsuki, H. Oka, Y. Miyajima, S. Shimizu, S. Suzuki, and K. Fujii, "Auditory Alert System for Fluorescence-Guided Resection of Gliomas; Technical Note," *Neurologia medico-chirurgica*, vol. 48, p. 95, 2008.
- [116] A. Kim, M. Khurana, Y. Moriyama, and B. C. Wilson, "Quantification of in vivo fluorescence decoupled from the effects of tissue optical properties using fiber-optic spectroscopy measurements," *Journal of Biomedical Optics*, vol. 15, p. 067006, 2010.
- [117] D. S. Kepshire, S. L. Gibbs-Strauss, J. A. O'Hara, M. Hutchins, N. Mincu, F. Leblond, M. Khayat, H. Dehghani, S. Srinivasan, and B. W. Pogue, "Imaging of glioma tumor with endogenous fluorescence tomography," *Journal of Biomedical Optics*, vol. 14, p. 030501, 2009.

- [118] G. I. Lozovaya, Z. Masinovsky, and A. A. Sivash, "Protoporphyrin ix as a possible ancient photosensitizer: Spectral and photochemical studies," *Origins of Life and Evolution of Biospheres*, vol. 20, pp. 321-330, 1990.
- [119] A. J. Durkin, S. Jaikumar, N. Ramanujam, and R. Richards-Kortum, "Relation between fluorescence spectra of dilute and turbid samples," *Appl. Opt.*, vol. 33, p. 414, 1994.
- [120] G. M. Palmer and N. Ramanujam, "Monte-Carlo-based model for the extraction of intrinsic fluorescence from turbid media," *Journal of Biomedical Optics*, vol. 13, p. 024017, 2008.
- [121] J. Wu, M. S. Feld, and R. P. Rava, "Analytical model for extracting intrinsic fluorescence in turbid media," *Appl. Opt.*, vol. 32, p. 3585, 1993.
- [122] M. G. Müller, I. Georgakoudi, Q. Zhang, J. Wu, and M. S. Feld, "Intrinsic fluorescence spectroscopy in turbid media: disentangling effects of scattering and absorption," *Appl. Opt.*, vol. 40, p. 4633, 2001.
- [123] W. C. Lin, S. A. Toms, E. D. Jansen, and A. Mahadevan-Jansen, "Intraoperative application of optical spectroscopy in the presence of blood," *Selected Topics in Quantum Electronics, IEEE Journal of*, vol. 7, p. 996, 2001.
- [124] J. C. Finlay and T. H. Foster, "Recovery of hemoglobin oxygen saturation and intrinsic fluorescence with a forward-adjoint model," *Appl. Opt.*, vol. 44, p. 1917, 2005.
- [125] B. W. Pogue and G. Burke, "Fiber-optic bundle design for quantitative fluorescence measurement from tissue," *Applied Optics* vol. 37, pp. 7429-7436, 1998.
- [126] H. J. Sterenborg, A. E. Saarnak, R. Frank, and M. Motamedi, "Evaluation of spectral correction techniques for fluorescence measurements on pigmented lesions in vivo," *Journal of Photochemistry and Photobiology B: Biology*, vol. 35, pp. 159-165, 1996.
- [127] M. C. Aalders, H. J. Sterenborg, F. A. Stewart, and N. van der Vange, "Photodetection with 5-Aminolevulinic Acid-induced Protoporphyrin IX in the Rat Abdominal Cavity: Drug-dose-dependent Fluorescence Kinetics," *Photochemistry and Photobiology*, vol. 72, pp. 521-525, 2000.
- [128] S. Pålsson, "Methods, Instrumentation and Mechanisms for Optical Characterization of Tissue and Treatment of Malignant Tumors," Doctoral, Department of Physics, Lund University of technology, Lund, 2003.
- [129] N. Haj-Hosseini, J. Richter, S. Andersson-Engels, and K. Wårdell, "Optical touch pointer for fluorescence guided glioblastoma resection using 5-aminolevulinic acid," *Lasers in Surgery and Medicine*, vol. 42, pp. 9-14, 2010.
- [130] ANSI. *American National Standard for Safe Use of Lasers* (2007). Available: http://www.lia.org/PDF/Z136_1_s.pdf
- [131] E. Jeffrey and W. v. M. Wolf, "Electrosurgical Devices," in *The Biomedical Engineering Handbook, Second Edition. 2 Volume Set*, ed: CRC Press, 1999.
- [132] C. S. Enwemeka, "Editorial: Standard Parameters in Laser Phototherapy," *Photomedicine and Laser Surgery*, vol. 26, pp. 411-411, 2008.
- [133] L. Lim, B. Nichols, N. Rajaram, and J. W. Tunnell, "Probe pressure effects on human skin diffuse reflectance and fluorescence spectroscopy measurements," *Journal of Biomedical Optics*, vol. 16, p. 011012, 2011.
- [134] L. Wang, S. L. Jacques, and L. Zheng, "MCML--Monte Carlo modeling of light transport in multi-layered tissues," *Computer Methods and Programs in Biomedicine*, vol. 47, p. 131, 1995.
- [135] E. Alerstam and S. Andersson-Engels. (2009). *Monte Carlo Simulations of Light Transport in Tissue*. Available:

- http://www.atomic.physics.lu.se/education/elective_courses/faf150_medical_optics/laboratory_and_computer_exercises/
- [136] A. Gronningsaeter, A. Kleven, S. B. S. Ommedal, T. E. Aarseth, T. Lie, F. Lindseth, T. Lango, and G. Unsgard, "SonoWand, an Ultrasound-based Neuronavigation System. [Miscellaneous Article]," *Neurosurgery*, vol. 47, pp. 1373-1380, 2000.
- [137] J. Richter, N. Haj-Hosseini, S. Andersson-Engels, and K. Wårdell, "Fluorescence spectroscopy measurement in ultrasonic navigated resection of malignant brain tumors," *Lasers in Surgery and Medicine*, vol. 43, pp. 8-14, 2011.
- [138] W. G. Zijlstra, A. Buursma, and O. W. van Assendelft, *Visible and Near Infrared Absorption Spectra of Human and Animal Haemoglobin determination and application*, 1 ed.: BRILL, 2000.
- [139] N. Haj-Hosseini, J. Richter, S. Andersson-Engels, and K. Wardell, "Photobleaching behavior of protoporphyrin IX during 5-aminolevulinic acid marked glioblastoma detection," in *Photonics West*, San Jose, CA, USA, pp. 716131-8, 2009.
- [140] M. Fitzmaurice, "Principles and pitfalls of diagnostic test development: implications for spectroscopic tissue diagnosis," *Journal of Biomedical Optics*, vol. 5, p. 119, 2000.
- [141] M. A. Ilias, J. Richter, F. Westermarck, M. Brantmark, S. Andersson-Engels, and K. Wardell, "Evaluation of a fiber-optic fluorescence spectroscopy system to assist neurosurgical tumor resections," in *Novel Optical Instrumentation for Biomedical Applications III*, Munich, Germany, p. 66310W, 2007.
- [142] Amnis. (2012, June). *ImageStream*. Available: <https://www.amnis.com/imagestream.html>
- [143] G. Osborne, "Flow cytometry at Queensland Brain Institute," ed. Brisbane, 2012.
- [144] W. J. Whitson, P. A. Valdes, B. T. Harris, K. D. Paulsen, and D. W. Roberts, "Confocal Microscopy for the Histological Fluorescence Pattern of a Recurrent Atypical Meningioma: Case Report," *Neurosurgery*, vol. 68, pp. E1768-E1773, 2011.
- [145] V. Ntziachristos, J. S. Yoo, and G. M. van Dam, "Current concepts and future perspectives on surgical optical imaging in cancer," *Journal of Biomedical Optics*, vol. 15, pp. 066024-12, 2010.
- [146] W. M. Stummer, S. P. Stocker, S. P. Wagner, H. P. Stepp, C. M. Fritsch, C. M. Goetz, A. E. M. Goetz, R. M. Kiefmann, and H. J. M. Reulen, "Intraoperative Detection of Malignant Gliomas by 5-Aminolevulinic Acid-induced Porphyrin Fluorescence," *SO - Neurosurgery March 1998;42(3):518-526*, 1998.
- [147] N. Sanai, J. Eschbacher, G. Hattendorf, S. W. Coons, M. C. Preul, K. A. Smith, P. Nakaji, and R. F. Spetzler, "Intraoperative Confocal Microscopy for Brain Tumors: A Feasibility Analysis in Humans," *Neurosurgery*, vol. 68 Operative Neurosurgery, pp. ons282-ons290, 2011.
- [148] H. Böhringer, E. Lankenau, F. Stellmacher, E. Reusche, G. Hüttmann, and A. Giese, "Imaging of human brain tumor tissue by near-infrared laser coherence tomography," *Acta Neurochirurgica*, vol. 151, pp. 507-517, 2009.
- [149] S. Kantelhardt, J. Leppert, J. Kantelhardt, E. Reusche, G. Hüttmann, and A. Giese, "Multi-photon excitation fluorescence microscopy of brain-tumour tissue and analysis of cell density," *Acta Neurochirurgica*, vol. 151, p. 253, 2009.
- [150] K. Konig, "New developments in multimodal clinical multiphoton tomography," 2011, p. 790305.